

A novel role for the E3 ubiquitin ligase FBXO7 in axon-myelin interaction

Ph.D. Thesis

In partial fulfillment of the requirements for the degree

“Doctor rerum naturalium (Dr.rer.nat)”

in the Neuroscience Program

at the Georg August University Göttingen,

Faculty of Biology

submitted by

Sabitha Lis Joseph

born in

Düsseldorf, Germany

Göttingen 2017



A novel role for the E3 ubiquitin ligase FBXO7 in axon-myelin interaction

Ph.D. Thesis

In partial fulfillment of the requirements for the degree

“Doctor rerum naturalium (Dr.rer.nat)”

in the Neuroscience Program

at the Georg August University Göttingen,

Faculty of Biology

submitted by

Sabitha Lis Joseph

born in

Düsseldorf, Germany

Göttingen 2017



Thesis Committee Members:

PD Dr. Judith Stegmüller (Reviewer)

Department of Neurology

RWTH University Aachen

Prof. Dr. Wolfgang Brück (Reviewer)

Department of Neuropathology

University Medical Center Göttingen

Prof. Dr. Klaus-Armin Nave

Department of Neurogenetics

Max Planck Institute for Experimental Medicine

Date of oral examination: 29th September 2017

Affidavit

I hereby declare that this PhD thesis entitled “**A novel role for the E3 ubiquitin ligase FBXO7 in axon-myelin interaction**” has been written independently with no other aid or sources than quoted.

A handwritten signature in black ink, appearing to read 'Sabitha Lis Joseph', with a stylized, cursive script.

Sabitha Lis Joseph

July 2017

Aachen, Germany

Für meine Mama.

Acknowledgments

Along my way to a PhD, I experienced the kind support of many people, to whom I would like to express my gratitude.

First and foremost, I would like to thank my supervisor PD Dr. Judith Stegmüller for her wonderful supervision. Your support and guidance throughout the years were remarkable and I highly appreciate our scientific discussions and your inspiring expertise that helped me along the way. Thank you for providing the encouraging atmosphere and opportunity for me to develop as a scientist.

Further on, I thank my thesis committee members Prof. Dr. Wolfgang Brück and Prof. Dr. Klaus-Armin Nave for their valuable suggestions and fruitful discussions during my thesis committee meetings.

Moreover, I want to thank my collaborators, Prof. Dr. Klaus-Armin Nave, Dr. Olaf Jahn, Dr. Wiebke Möbius, Dr. Miso Mitkovski, Dr. Hauke Werner, Prof. Dr. Michael Sereda and Prof. Dr. Joachim Weis for their supportive contribution to my PhD project.

I further would like to highlight, how much I appreciate the incredible effort and immense support that the coordinators (Prof. Dr. Michael Hörner and Sandra Drube) of the IMPRS Neuroscience program provided. Thank you Michael and Sandra for making this PhD journey so pleasant and smooth sailing. I am very grateful to have had the opportunity to be part of this program.

I also want to thank Prof. Dr. Jörg Schulz, who welcomed us in the department of Neurology at the University Hospital Aachen, for his interest in my PhD project and his helpful input.

A special, heartfelt thank you goes to my amazing colleges, who made the past years of my PhD so enjoyable. I had the great fortune to have you, Ghergana as my companion and friend since the first day of my journey. Thank you for your mental support, your great sense of humor, your inspiring knowledge and the wonderful time we had. I also like to thank Siv for being an amazing project partner and a great support. Your drive and ambition for science is truly inspiring and it was a delight to work with such a witty person like you. Nicola and David, you were wonderful bay-mates and I thank you for all the great help and advice I received from you whenever I was in doubt. I further want to thank Shih-Ju, Chaitali, Anna, Anika and Alina for being amazing lab-mates and providing a wonderful atmosphere in lab. Thank you, to all members of AG Awesome for the great

times we had in and outside of lab. Having said that, I also want to thank Yuhao, Quan and all my other colleagues in Aachen, who welcomed me in the new lab and contributed to the great time I had in the last period of my PhD. Thank you Vibha, for your cheerful attitude and all the amusing conversation we had that made especially tedious incubation times pass so quickly.

Pratibha, Ghergana, Siv and Kathy I would like to thank for prove-reading my dissertation and all the helpful suggestions you provided.

My deepest gratitude however goes to my family. You are the foundation on which I stay and without you I would have not come so far. No words can describe how deeply blessed I feel to have such a loving and supporting family. Your constant encouragement and your tremendous love guide my ways and lift me up in difficult times. Mama and Papa, your hard work, devotion and inspiring achievements in life paved the way, on which Smitha and I are walking on. You strengthen us with your unconditional support and love to reach for the stars and taught us to never loose hope, no matter what challenges life might bring. Smitha you are an amazingly supportive, encouraging and caring sister and the best role model a younger sister can hope to look up to. In all my ups and downs, you have been my greatest advisor and with your courage, fortitude and love you are a true inspiration for me.

Table of Content

Table of Content	I
List of figures	V
List of tables	VII
Abstract	1
1. Introduction	2
1.1 The nervous system	2
1.2 Glial cells	2
1.2.1 Myelinating cells.....	3
1.2.2 Myelin.....	4
1.2.3 Axon-glia interaction.....	5
1.2.4 Dysfunctions in myelinating cells induce axonal pathology	6
1.3 The ubiquitin-proteasome system (UPS)	7
1.3.1 E3 ubiquitin ligases	10
1.3.2 UPS dysfunctions are associated with neurodegenerative diseases.....	11
1.4 <i>PARK</i> genes	13
1.5 <i>FBXO7</i>	15
1.5.1 SCF-E3 ubiquitin ligase.....	17
1.5.2 Interaction partners of <i>FBXO7</i>	18
1.5.3 Mutation in <i>PARK15</i>	20
Aim of the study	22
2. Materials and methods	23
2.1 Materials	23
2.1.1 Lab equipment and consumables	23
2.1.2 Chemicals and reagents	24
2.1.3 Enzymes	24
2.1.4 Kits	25
2.1.5 Software	25
2.1.6 Antibodies	25
2.1.7 Buffers and stock solutions	27

2.1.8 Mammalian cell lines.....	29
2.1.9 Plasmid constructs and primers.....	30
2.2 Methods.....	31
2.2.1 Cell culture.....	31
2.2.1.1 Passage of immortalized cell lines.....	31
2.2.2 Transfection of cultured cells.....	32
2.2.2.1 Calcium phosphate transfection.....	32
2.2.2.2 Lipofectamine® 2000 transfection.....	32
2.2.3 Biochemical techniques.....	33
2.2.3.1 Lysis of tissue.....	33
2.2.3.2 Lysis of cultured cells.....	33
2.2.3.3 Measurement of protein concentration.....	33
2.2.3.4 Co-Immunoprecipitation (Co-IP).....	34
2.2.3.5 SDS-PAGE and western-blot.....	35
2.2.4 FACS and proteasome activity assay.....	36
2.2.5 Myelin purification.....	36
2.2.5.1 Silver staining of SDS-PAGE.....	37
2.2.5.2 Quantitative Mass spectrometry.....	37
2.2.6 Transgenic mouse line.....	38
2.2.6.1 Generation of conditional FBXO7 mouse line.....	38
2.2.6.2 Tamoxifen induced knock down.....	39
2.2.6.3 Isolation of genomic DNA.....	39
2.2.6.4 Genotyping.....	39
2.2.6.5 RNA isolation.....	40
2.2.6.6 cDNA synthesis.....	41
2.2.6.7 Quantitative real-time (RT) PCR.....	41
2.2.6.8 Electrophysiological measurement.....	42
2.2.7 Histological analysis.....	43
2.2.7.1 Transcardial perfusion and fixation.....	43
2.2.7.2 Immunohistochemistry on cryo-sections.....	43
2.2.7.3 Immunohistochemistry on paraffin-sections.....	44
2.2.7.4 Tunnel assays.....	45
2.2.7.5 Gallyas silver impregnation.....	45
2.2.8 Electron microscopic analysis.....	46
2.2.8.1 Tissue preparation and epon embedding.....	46
2.2.8.2 Staining of semi-thin sections.....	47
2.2.8.3 Contrasting of ultra-thin sections.....	47
2.2.9 Mouse behavioral analyses.....	48
2.2.9.1 Elevated plus maze.....	48

2.2.9.2	Open field	48
2.2.9.3	Tail suspension test	49
2.2.9.4	Kyphosis	49
2.2.9.5	Inverted grid	49
2.2.9.6	Pole test	49
2.2.9.7	Wire hang	50
2.2.9.8	Balance beam	50
2.2.9.9	Rota-Rod	50
2.2.9.10	Hot plate	51
2.2.10	Statistical analysis	51
3.	Results	52
3.1	Systemic characterization of <i>Cnp1</i>^{Cre/+};<i>Fbxo7</i>^{fl/fl} mice	52
3.1.1	Deletion of <i>Fbxo7</i> in myelinating cells by generating a conventional <i>Cnp1</i> ^{Cre/+} ; <i>Fbxo7</i> ^{fl/fl} mouse line	52
3.1.2	<i>Cnp1</i> ^{Cre/+} ; <i>Fbxo7</i> ^{fl/fl} mice display a distinct phenotype	53
3.1.3	<i>Cnp1</i> ^{Cre/+} ; <i>Fbxo7</i> ^{fl/fl} mice show paresis of the hind limbs caused by muscle weakness	54
3.2	Cellular characterization of <i>Cnp1</i>^{Cre/+};<i>Fbxo7</i>^{fl/fl} mice	56
3.2.1	Loss of <i>Fbxo7</i> does not affect myelination but leads to a shift in axon caliber .	56
3.2.2	<i>Cnp1</i> ^{Cre/+} ; <i>Fbxo7</i> ^{fl/fl} mice display prominent axonal degeneration in the periphery	65
3.2.3	Knockdown of <i>Fbxo7</i> from myelinating cells leads to increased inflammation .	72
3.3	Molecular characterization of <i>Cnp1</i>^{Cre/+};<i>Fbxo7</i>^{fl/fl} mice	78
3.3.1	<i>Fbxo7</i> deletion leads to an up-regulation of stress sensors and down-regulation of cytoskeletal proteins in CNS myelin	78
3.3.2	Loss of <i>Fbxo7</i> causes an immune response and down-regulation of cytoskeleton proteins in PNS myelin	81
3.3.3	Increased myelin maintenance in the CNS and signs of peripheral neuropathy in <i>Cnp1</i> ^{Cre/+} ; <i>Fbxo7</i> ^{fl/fl} mice	84
3.3.4	<i>Cnp1</i> ^{Cre/+} ; <i>Fbxo7</i> ^{fl/fl} mice show unaltered development of oligodendrocytes regarding NG2 and CNP levels	86
3.3.5	Knockdown of the E3-ubiquitin ligase FBXO7 decreases proteasome activity.	87
3.4	The post-developmental contribution of FBXO7 to the maintenance of the axon-glia interaction	90
3.4.1	Generation of the <i>Plp1</i> ^{CreERT2/+} ; <i>Fbxo7</i> ^{fl/fl} mouse line	90
3.4.2	<i>Plp1</i> ^{CreERT2/+} ; <i>Fbxo7</i> ^{fl/fl} mice show a moderate reduction of motor endurance and progressive muscle weakness	92
3.4.3	Post-developmental loss of <i>Fbxo7</i> does not affect myelination, but induces a moderate axonal degeneration and immune response	94

4. Discussion	97
4.1 Deletion of <i>Fbxo7</i> in myelinating cells results in a strong motor phenotype in <i>Cnp^{Cre/+};Fbxo7^{fl/fl}</i> mice	97
4.2 Loss of <i>Fbxo7</i> does not affect myelin integrity, but leads to degeneration of large-caliber axons in the PNS.....	98
4.3 Deletion of <i>Fbxo7</i> causes a shift in axon diameter without affecting myelination in the CNS	100
4.4 FBXO7 remains relevant for the post-developmental maintenance of the axon-myelin interaction	101
4.5 Lack of <i>Fbxo7</i> elicits a strong inflammatory response and an increase in detoxification processes	102
4.6 Mutation in the <i>FBXO7</i> gene cause Parkinsonian-Pyramidal syndrome	105
4.7 Molecular changes induced by loss of <i>Fbxo7</i>.....	106
5. Conclusion and perspectives	109
List of abbreviations	110
Nomenclature.....	119
References	120

List of figures

1. Introduction	2
Figure 1.2.1 Different types of myelinating cells in the CNS and PNS.	3
Figure 1.2.2 Distribution of compact and non-compact myelin proteins at the axon-glia junction in the CNS.	5
Figure 1.3.3 The cycle of protein ubiquitination.	9
Figure 1.3.4 The 26S/30S proteasome.	10
Figure 1.5.5 The <i>Fbxo7</i> gene and protein structure.	17
Figure 1.5.6 The FBXO7 SCF-E3 ubiquitin ligase.	17
3. Results	52
Figure 3.1.1 Validation of <i>Cnp1</i> ^{Cre/+} ; <i>Fbxo7</i> ^{fl/fl} knockout mouse line.	53
Figure 3.1.2 <i>Cnp1</i> ^{Cre/+} ; <i>Fbxo7</i> ^{fl/fl} mice display kyphosis, muscle and lung atrophy.	54
Figure 3.1.3 <i>Cnp1</i> ^{Cre/+} ; <i>Fbxo7</i> ^{fl/fl} mice show reduced motor performance, due to paresis of hind limbs and muscle weakness.	55
Figure 3.2.1 <i>Cnp1</i> ^{Cre/+} ; <i>Fbxo7</i> ^{fl/fl} mice present no histological changes in myelination.	58
Figure 3.2.2 <i>Cnp1</i> ^{Cre/+} ; <i>Fbxo7</i> ^{fl/fl} mice do not display any major alterations in CNS myelination, but a shift in axon caliber.	60
Figure 3.2.3 <i>Cnp1</i> ^{Cre/+} ; <i>Fbxo7</i> ^{fl/fl} mice show no severe changes in PNS myelination, but a shift in axon caliber.	62
Figure 3.2.4 <i>Cnp1</i> ^{Cre/+} ; <i>Fbxo7</i> ^{fl/fl} mice display a normal abundance of oligodendrocyte, Schwann cell and Remak cell nuclei.	64
Figure 3.2.5 <i>Cnp1</i> ^{Cre/+} ; <i>Fbxo7</i> ^{fl/fl} mice show axonal damage in the PNS.	66
Figure 3.2.6 Loss of FBXO7 induces an increase in axon caliber in the CNS and a shift towards small caliber axons in the PNS of <i>Cnp1</i> ^{Cre/+} ; <i>Fbxo7</i> ^{fl/fl} mice.	67
Figure 3.2.7 <i>Cnp1</i> ^{Cre/+} ; <i>Fbxo7</i> ^{fl/fl} mice show no significant increase in the number of axons as well as degenerated axons in the optic nerve.	68
Figure 3.2.8 Loss of <i>Fbxo7</i> leads to increased axonal degeneration within the sciatic nerve of <i>Cnp1</i> ^{Cre/+} ; <i>Fbxo7</i> ^{fl/fl} mice.	70
Figure 3.2.9 Severe axonal degeneration in the sciatic nerve of <i>Cnp1</i> ^{Cre/+} ; <i>Fbxo7</i> ^{fl/fl} mice.	71
Figure 3.2.10 Increased inflammation in the white matter of cerebellum and spinal cord of <i>Cnp1</i> ^{Cre/+} ; <i>Fbxo7</i> ^{fl/fl} mice.	74
Figure 3.2.11 Levels of inflammatory markers show a trend of elevation in the cerebellum of <i>Cnp1</i> ^{Cre/+} ; <i>Fbxo7</i> ^{fl/fl} mice.	75

Figure 3.2.12 Increased inflammatory response in sciatic nerve of <i>Cnp1^{Cre/+};Fbxo7^{fl/fl}</i> mice.	77
Figure 3.3.1 Up- and down-regulated proteins in CNS myelin upon deletion of <i>Fbxo7</i>	79
Figure 3.3.2 Increased GST π 1 levels in the CNS due to <i>Fbxo7</i> deletion.	81
Figure 3.3.3 Up- and down-regulated proteins in PNS myelin upon <i>Fbxo7</i> deletion. .	83
Figure 3.3.4 Increased GST π 1 signal in sciatic nerve isolated from <i>Cnp1^{Cre/+};Fbxo7^{fl/fl}</i> mice.	84
Figure 3.3.5 Loss of <i>Fbxo7</i> induces an increase in CNS myelin maintenance and affects proteins, which are associated with peripheral neuropathy in the PNS.	85
Figure 3.3.6 <i>Fbxo7</i> deletion does not influence the development of oligodendrocytes.	87
Figure 3.3.7 The FBXO7 F-box domain is crucial for the SCF-complex formation.	88
Figure 3.3.8 Knockdown of FBXO7 in Schwann cells leads to decreased proteasome activity.	89
Figure 3.4.1 Validation of Tamoxifen-inducible <i>Pip1^{CreERT2/+}; Fbxo7^{fl/fl}</i> mouse line.	91
Figure 3.4.2 <i>Pip1^{CreERT2/+}; Fbxo7^{fl/fl}</i> mice show mild but progressive muscle weakness and reduced motor endurance.	93
Figure 3.4.3 <i>Pip1^{CreERT2/+}; Fbxo7^{fl/fl}</i> mice display no alteration in PNS myelination and no significant but slight increase in axonal degeneration and inflammation.	95

List of tables

2. Materials and methods	Error! Bookmark not defined.
Table 2.1.1 List of enzymes used in the study.	24
Table 2.1.2 List of commercially available kits used in this study.....	25
Table 2.1.3 List of commercially available primary antibodies used in this study.....	26
Table 2.1.4 List of commercially available secondary antibodies used in this study..	26
Table 2.1.5 Immortalized cell lines used for experiments.....	29
Table 2.1.6 Plasmid constructs and primers used in this study.....	30
Table 2.2.1 Recipe for SDS-PAGE gels of different acrylamide percentage.....	35
Table 2.2.2 Recipe for PCR reaction.....	40
Table 2.2.3 Set up of PCR program for genotyping.	40
Table 2.2.4 Protocol for cDNA synthesis I.....	41
Table 2.2.5 Procedure for cDNA synthesis II.	41
Table 2.2.6 Protocol for RT-PCR.....	42

Abstract

The regulated turnover of proteins is an essential aspect of every cell. Cells must be able to respond to environmental changes or undergo different developmental stages, while still maintaining a balanced protein homeostasis. The ubiquitin-proteasome system (UPS) is a major intracellular regulator of the protein homeostasis and is responsible for protein degradation and quality control. Dysfunctions of the UPS have been linked to various neurodegenerative diseases and opened up a new perspective on the disease-causing mechanism in these disorders.

The E3-ubiquitin ligase FBXO7 is part of the UPS and is expressed throughout the brain, predominantly in the cortex, hippocampus and substantia nigra, as well as in the white matter of the cerebellum and corpus callosum. Mutations of the *Fbxo7* gene (*PARK15*) are known to cause an early-onset form of Parkinsonism with a broad spectrum of symptoms, which are collectively referred to as Parkinsonian-Pyramidal syndrome. So far, the role of FBXO7 in the nervous system is not fully understood and while recent studies focused on the function of FBXO7 in neurons, its importance in myelinating cells has not been investigated. Although myelinating cells are as equally important to the function of the nervous system as neurons, little is known about the relevance of the UPS in myelinating cells.

In my project, I investigated the importance of FBXO7 for myelinating cells and its impact on the axon-myelin interaction. Therefore, we generated the *Cnp1^{Cre/+};Fbxo7^{fl/fl}* mouse line, in which FBXO7 was deleted from myelinating cells. The phenotype of *Cnp1^{Cre/+};Fbxo7^{fl/fl}* mice displayed severe motor deficit and premature death. Interestingly, I showed that deletion of *Fbxo7* did not induce significant changes in myelination, however severely affected the integrity of axons. Moreover, deletion of *Fbxo7* from Schwann cells affected the survival of axons in the PNS to a greater extent, than the integrity of CNS axons, when deleted from oligodendrocytes. In order to elucidate the post-developmental contribution of FBXO7 to the maintenance of the axon-glia interaction, I further generated the Tamoxifen-inducible *Pip1^{CreERT2/+};Fbxo7^{fl/fl}* mouse line, in which FBXO7 was deleted from myelinating cells once myelination was completed. I found FBXO7 to be less crucial, however still relevant for the function of myelinating cells regarding axonal support, once myelination was completed. Concluding from my results, I demonstrate the vital importance of FBXO7 for myelinating cells, particularly during development. Furthermore, I showed that FBXO7 is essential for the maintenance of the axon-myelin interaction, especially in the PNS.

1. Introduction

1.1 The nervous system

The human nervous system is a remarkable structure, which has developed in the course of evolution to perform exceptional tasks. It computes information from inside and outside the body and generates an appropriate response, which enables us to interact with our environment, conduct higher cognitive activities and regulate almost all our body functions. In vertebrates, the two main parts of the nervous system are the central nervous system (CNS) and the peripheral nervous system (PNS). While the CNS consists of the brain and spinal cord, the PNS mainly comprises nerves, which connect the CNS to every part of the body. At a cellular level, the main constituents of the nervous system are neurons and glial cells. Neurons receive and process signals and relay this information to connected neurons of the network via electrical and chemical signals, known as action potentials (AP). Neurons that connect to each other form neuronal circuitries (Eric R. Kandel, 2000). Glial cells provide a functional scaffold for neurons and together these cells engage in a bi-directional dialogue that is essential for the functioning of neuronal networks. The detailed function of glial cells, however, has only just started to be unraveled.

1.2 Glial cells

Glial cells are typically subdivided into astrocytes, microglia and myelinating cells and are as abundant as neurons in the nervous system (Azevedo et al., 2009; Eric R. Kandel, 2000). The main function of astrocytes is to support the neuronal network by transferring nutrients, recycling neurotransmitter from the synaptic cleft and participating in the inflammatory response - to name a few functions (Carson et al., 2006; Eric R. Kandel, 2000; Helmut Kettenmann, 2013).

Microglia are brain-specific inflammatory cells, which are activated during an inflammatory event. Further on, they support the clearance of debris from apoptotic cells and synapses (Allen and Barres, 2009).

Myelinating cells insulate axons with a multilayered myelin sheath, by extending their cell membrane and wrapping it around long segments of axons (Nave, 2010a). Myelination increases the electrical resistance and lowers the capacitance of axons, which enables a fast and saltatory propagation of the action potential that is 50 to 100 fold faster compared to non-myelinated axons. In addition, myelinated axons consume less energy compared

to non-myelinated axons, since they not require as much energy to maintain ion gradients along insulated axons (Nave, 2010b). Evolutionarily, these characteristics of myelinated axons were beneficial for developing fast and complex brain function.

1.2.1 Myelinating cells

There are two types of myelin-producing cells specific for each part of the nervous system: oligodendrocytes in the CNS and Schwann cells in the PNS. While oligodendrocytes are capable of myelinating multiple segments of different axons at the same time, Schwann cells only myelinate one axonal segment (Helmut Kettenmann, 2013; Jessen and Mirsky, 2005) (**Figure 1.2.1**). Another subclass of Schwann cells are the non-myelinating Remak cells that engulf small caliber C-fibers axons and form the so-called Remak bundles (Feltri et al., 2016). In both CNS and PNS the axon-myelin interaction is comparable and accomplishes similar tasks, which are performed by overlapping, but not identical set of proteins (Nave, 2010a).

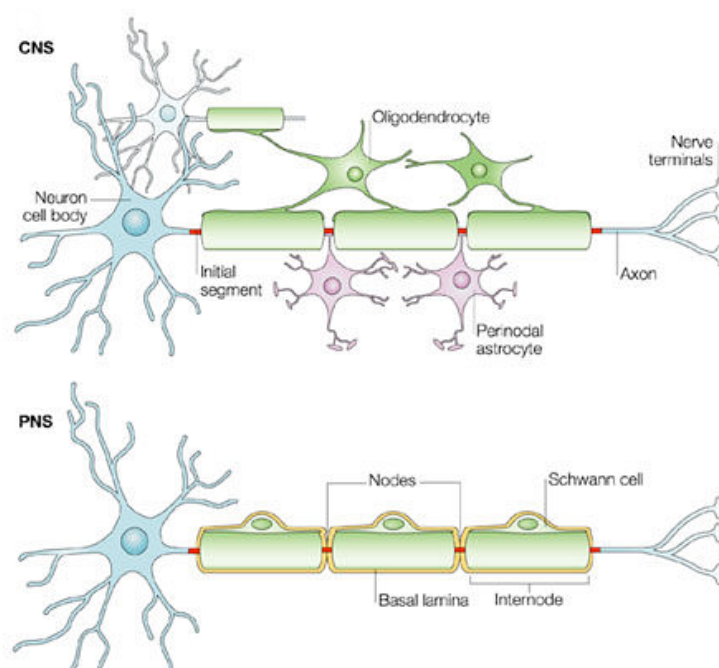


Figure 1.2.1 Different types of myelinating cells in the CNS and PNS.

Oligodendrocytes exclusively myelinate axons of the CNS, whereas axons of the PNS are myelinated by Schwann cells. While oligodendrocytes are able to myelinate multiple axonal segments, Schwann cells only wrap around one axonal segment. Both types of myelinating cells enable the saltatory propagation of action potentials. The figure was modified from: Poliak S, Peles E (2003) The local differentiation of myelinated axons at nodes of Ranvier. *Nat Rev Neurosci* 4:968-980, doi:10.1038/nrn1253. Reprinted by permission from Macmillan Publishers Ltd: *Nat Rev Neurosci*, copyright (2003). Nature publishing group license number 4151391176819.

1.2.2 Myelin

Myelin is a specialized plasma membrane that consists of 80% lipids and approximately 20% of proteins (as per dry weight) (Norton and Autilio, 1965; Pfeiffer et al., 1993). This enrichment in lipids is the underlying reason for the insulating properties of myelin. Owing to the low density, the purifications of myelin via density gradient centrifugation is feasible (Norton and Poduslo, 1973a). The most abundant proteins within CNS myelin are proteolipid protein (PLP) and myelin basic protein (MBP), representing 17% and 8% of total myelin, respectively. In the PNS, myelin protein zero (MPZ or P0), periaxin and MBP constitute 21, 16 and 8% of total myelin, respectively. Further, myelin proteins that are expressed in both systems include 2',3'-cyclic nucleotide 3'-phosphodiesterase (CNP), myelin-associated glycoprotein (MAG) and tetraspanin-29 (known as CD9) (Jahn et al., 2009; Patzig et al., 2011). Myelin can be divided in two distinct domains: compact and non-compact myelin (Poliak and Peles, 2003). Compact myelin defines the tightly packed layers of myelin, which are devoid of cytoplasm and contain proteins including MBP, PLP and MPZ (Dupouey et al., 1979; Martini et al., 1995). The cytoplasmic rich non-compact region represents a specific axon-glia contact zone, in which the myelinating cell interacts with the axonal side and the nodes of Ranvier. This region contains proteins like CNP and MAG and further harbors organelles, secretory vesicles and a cytoskeleton (Nave, 2010b; Zuchero and Barres, 2011).

The node of Ranvier describes the region between two segments of myelin. Here, the axon is not insulated by myelin and contains a high density of voltage-gated sodium channels as well as other channels, which enable the saltatory propagation of an AP from one node to the neighboring one (Bennett and Lambert, 1999; Eric R. Kandel, 2000). Next to the nodes of Ranvier is the non-compact paranodal region, which is adjacent to the juxtaparanodal region. Within these domains, myelin interacts with the axon, by means of adhesion proteins to maintain the axon-glia interface. The juxtaparanodal region further harbors potassium channels, which repolarize the axonal membrane during an AP (Eric R. Kandel, 2000; Poliak and Peles, 2003; Tait et al., 2000) (**Figure 1.2.2**). Myelin thickness is tightly regulated by axonal signals such as neuregulin 1 type III in the PNS (Michailov et al., 2004; Taveggia et al., 2005). A method to evaluate the thickness of myelin is to measure the g-ratio, which determines the ratio of inner axonal diameter divided by outer diameter of the myelinated axon (Rushton, 1951). The average g-ratio in the CNS is around 0.77 and in the PNS has an approximate value of 0.6 (Chomiak and Hu, 2009; Rushton, 1951). Variations in g-ratio indicate potential pathological changes in myelination.

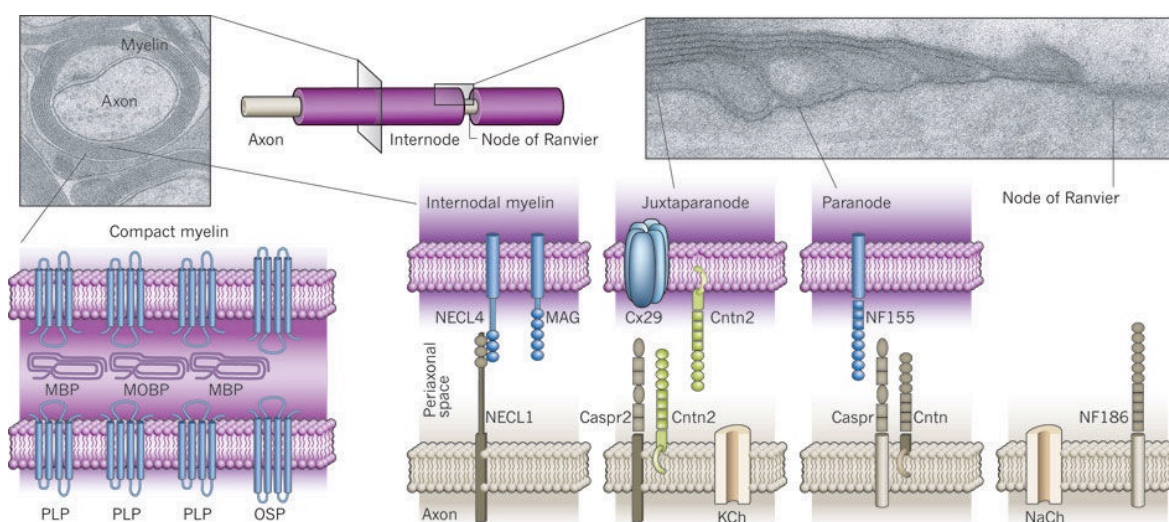


Figure 1.2.2 Distribution of compact and non-compact myelin proteins at the axon-glia junction in the CNS.

The illustration shows the distribution of myelin proteins at the axon-glia interface along different regions of myelin. The regions depicted include compact myelin, juxtaparanode, paranode and the node of Ranvier. The electron microscopic images show the ultrastructure of cross- and longitudinal-section of a myelinated axon from the CNS. Abbreviations: Caspr: contactin-associated protein; Cntn: contactin; Cx29: connexin 29 kDa; KCh: fast potassium channels; MAG: myelin-associated glycoprotein; MBP: myelin basic protein; MOBP: myelin oligodendrocyte basic protein; NaCh: voltage-gated sodium channels; NECL: nectin-like protein/synCAM; NF155/186: neurofascin 155 kDa/186 kDa; OSP: oligodendrocyte-specific protein; PLP: proteolipid protein. The figure was adapted from: Nave, K.A. (2010). Myelination and support of axonal integrity by glia. *Nature* 468, 244-252 10.1038/nature09614. Reprinted by permission from Macmillan Publishers Ltd: Nature, copyright (2010). Nature publishing group license number 4151350094282.

1.2.3 Axon-glia interaction

In addition to ensuring a fast and saltatory propagation of the AP, myelinating cells are crucial for the long-term integrity and survival of axons (Griffiths et al., 1998; Lappe-Siefke et al., 2003; Nave, 2010a; Yin et al., 1998). Previous studies showed that myelinating cells support the integrity of axons by providing neurotrophic factors, such as growth factors and cytokines (Nave, 2010a, b). Schwann cells secrete molecules like ciliary neurotrophic factor (CNTF) and erythropoietin to enhance axonal survival. Moreover, it has been shown that deletion of the gene encoding neuregulin1 receptor ErbB3 in Schwann cell induces severe neuropathy (Keswani et al., 2004; Riethmacher et al., 1997; Simon et al., 2010). Oligodendrocytes release factors including brain-derived neurotrophic factor (BDNF), neurotrophin3 (NT3), insulin-like growth factor 1 (IGF1) and glial cell-derived neurotrophic factor (GDNF) to support axonal function (Dai et al., 2003; Du and Dreyfus, 2002; Wilkins et al., 2003). Additionally, myelinating cells supply axons with

metabolic factors, as myelinated and thus insulated axons are deprived of metabolic access from the extracellular space (Nave, 2010b). Especially axons that have larger calibers have a higher energy demand and are highly dependent on the metabolic support of glial cells. Myelinating cells express the glial glucose transporter GLUT1 and are able to take up glucose from the blood vessels. They have also been reported to perform more glycolytic metabolism than oxidative metabolism, resulting in pyruvate and lactate as products (Lee et al., 2012b; Morland et al., 2007). Further studies show that oligodendrocyte-derived lactate is shuttled through the monocarboxylate transporter MCT1 via the axonal-specific MCT2 transporter into axons, where lactate is metabolized (Funfschilling et al., 2012; Lee et al., 2012b; Saab et al., 2013; Simons and Nave, 2015). These additional contributions of myelinating cells to the maintenance of axons are independent from their myelinating function and persist throughout the lifetime of an axon-glia symbiosis (Nave, 2010a). The axon-glia axis is not a one-way street, but is rather based on a bi-directional communication and mutual support (Taveggia et al., 2005). Hence, axonal signals also control the survival, proliferation, differentiation and myelination of myelinating cell. Neuregulin1 type III (NRG1), which is expressed by axons, has been shown to control myelination by Schwann cells, as well as the cells' proliferation and survival (Michailov et al., 2004; Nave and Salzer, 2006). In the CNS, growth factors and cytokines like BDNF, CNTF, platelet derived growth factor (PDGF) and leukemia inhibitory factor (LIF) control proliferation and differentiation of oligodendrocytes (Nave, 2010a).

1.2.4 Dysfunctions in myelinating cells induce axonal pathology

Myelinating cells support and maintain axonal integrity, but when alterations occur within myelinating cells, this supportive function is disturbed. Abnormalities in myelinating cells can induce axonal degeneration and eventually cause different neurodegenerative diseases (Nave, 2010a). Studies, in which mouse models lack particular myelin proteins, demonstrated the relevance of a functional axon-glia interaction. Mutations of *Mpz* in Schwann cells or mutations of the *Pip1* gene leading to a medium number of gene-copies in oligodendrocytes induce dysmyelination and eventually causes axonal loss (Clark et al., 2013; Griffiths et al., 1998; Klugmann et al., 1997; Suter and Scherer, 2003). These pathological changes are seen in neurological disorders such as Charcot-Marie-Tooth (CMT), an inherited peripheral neuropathy, in which *MPZ* is mutated (De Jonghe et al., 1999). Moreover, mutations in *PLP1* are linked to Pelizaeus-Merzbacher disease, which is an inherited form of leukodystrophy (Garbern, 2007). Interestingly, myelinating cells can

also cause axonal degeneration, without major impairments in myelin synthesis. Mouse models, in which *Cnp1* is deleted, develop without motor symptoms until four months of age and display a normal compaction of the myelin sheaths. However at around six months of age, these mice exhibit altered paranodes, axonal swellings, defective axonal transport and axonal death, which reflects in a prominent motor phenotype in young adult mice (Edgar et al., 2009; Lappe-Siefke et al., 2003). Furthermore, in *Plp1*^{-/-} mice, which undergo normal motor development in the first year, the overall myelination appears to be intact, but long spinal tracts show progressive degeneration (Garbern et al., 2002; Griffiths et al., 1998; Klugmann et al., 1997). Myelin of *Plp1*^{-/-} mice only show abnormalities at an ultrastructural level (Rosenbluth et al., 2006). Mutations of the *Plp1* gene have a dose-dependent effect depending on the number of copies of the transgene (Griffiths et al., 1998). While high gene copies induce more severe symptoms, a prominent dysmyelination and early death, low gene copies or *Plp1*^{-/-} mice only develop late onset neurodegenerations including axonal degeneration (Griffiths et al., 1998). Long-traveling axons appear to be most vulnerable to this lack of support by dysfunctional myelin cells, as it is seen in *Plp1*^{-/-} and *Mpz* mouse models (Garbern, 2007; Griffiths et al., 1998). Investigations on myelin function always pose an interdisciplinary challenge, due to its close axonal interaction. In the recent decades interesting and essential new functions of myelinating cells have been identified, however further studies are required to better understand the axon-glia axis and thereby elucidate the pathological changes occurring in neurological disorders.

1.3 The ubiquitin-proteasome system (UPS)

The proper function of a cell is based on a well-orchestrated interplay of fundamental cellular mechanisms. Such mechanisms including metabolism, energy production, molecular transport, cell division, cell growth and structural arrangement are constantly regulated. The ubiquitin-proteasome system (UPS) is a major intracellular regulator that is responsible for protein degradation and quality control (Hershko and Ciechanover, 1998). It therefore participates in essentially all processes involved in the precise spatial and temporal regulation of protein homeostasis. Target proteins of the UPS are modified with ubiquitin (Ub), a small 8.5 kDa molecule that is covalently attached to lysine residues of the substrate (Hershko and Ciechanover, 1998; Schlesinger and Goldstein, 1975). Conjugation of ubiquitin to a substrate is accomplished via a three-step enzymatic cascade. Initially, Ub is activated in an ATP-dependent manner by the ubiquitin-activating enzyme E1. It is then transferred to the ubiquitin-conjugating enzyme E2. From there,

ubiquitin can either be directly coupled to a substrate that is specifically bound to an E3 ubiquitin ligase, or Ub is transferred onto an E3 ubiquitin ligase and then conjugated to a substrate recruited by this particular E3 ligase (Ciechanover and Schwartz, 2002; Pickart and Eddins, 2004). The modification of proteins by ubiquitin determines their fate, which is why ubiquitination can be viewed as a code. A substrate can either be mono-ubiquitinated, multimon-ubiquitinated or poly-ubiquitinated. Poly-ubiquitination occurs when additional Ub molecules are attached to one of the seven lysine (K) residues of the preceding ubiquitin. Linkages of K48 Ub-chains are commonly associated with proteasomal degradation; whereas K63 linked chains are mainly considered to induce a non-proteolytic, functional modification of the target protein (Komander and Rape, 2012; Pickart and Fushman, 2004). Furthermore, protein degradation is also regulated by deubiquitinating enzymes (DUBs), which can reverse ubiquitination of mono- or poly-ubiquitinated proteins by removing Ub molecules. DUBs thereby are able to reverse the fate of modified proteins and additionally are able to recycle Ub molecules during protein degradation for further ubiquitination processes (Glickman and Ciechanover, 2002; Lilienbaum, 2013) (**Figure 1.3.3**). Proteins designated for degradation, are generally send to the 26S multi-catalytic proteasome. This complex consists of two compartments: the 20S barrel-shaped core particle (CP) and the 19S regulatory particle (RP), which is attached to one or both ends of the CP. The core particle consists of two β -rings located at the center and two outer α -rings (Bochtler et al., 1999). One α -ring and one β -ring comprise seven α -subunits and seven β -subunits, respectively. The α -rings, provide structural stability to the proteasome holoenzyme, while the β -rings harbor catalytic activity. Prior to proteolysis, the RP recruits ubiquitinated proteins to the proteasome. The RP is bound to the α -rings and harbors an ubiquitin-recognition motif for binding ubiquitinated proteins. Moreover, the RP unfolds and prepares the ubiquitinated substrate for degradation in the core (Dikic, 2017) (**Figure 1.3.4**).

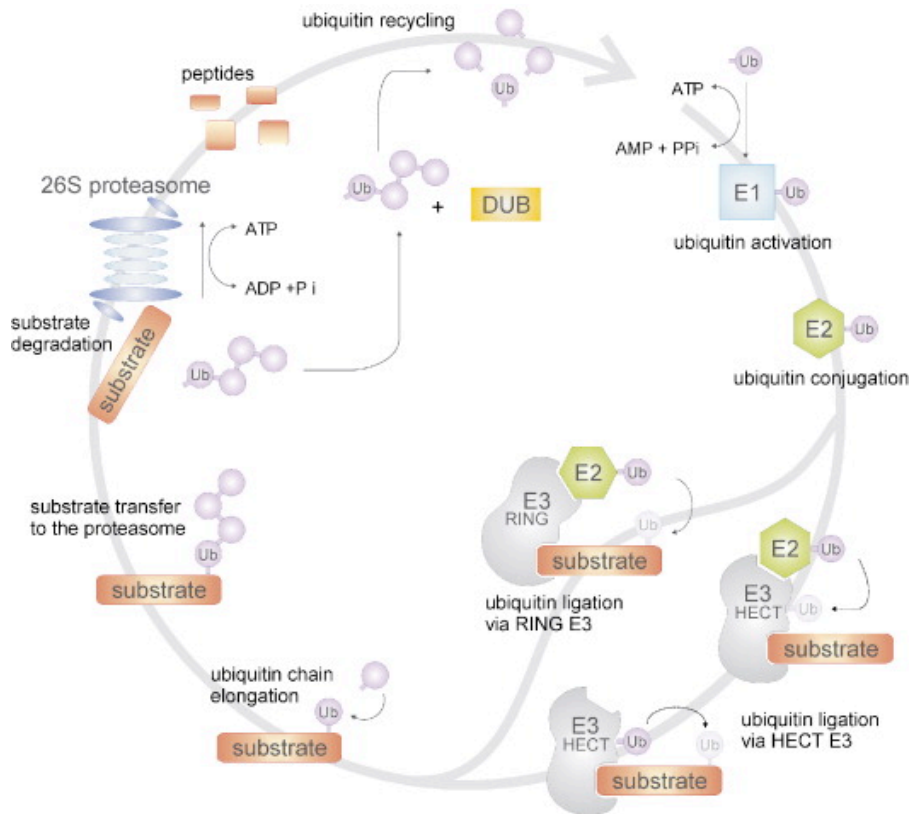


Figure 1.3.3 The cycle of protein ubiquitination.

The Ubiquitin-proteasome system starts with the activation of ubiquitin (Ub) by the E1-activating enzyme. Ub is then transferred on to the E2-conjugating enzyme. Proteins designated for ubiquitin-modification or degradation, interact with the E3-ubiquitin ligase, which mediated the ubiquitination of the target substrate. E3-ubiquitin ligases are classified in RING or HECT-E3 enzymes. Substrates that are poly-ubiquitinated by K48 linkage of Ub generally bind to the 26S proteasome and are degraded. Finally, Ub molecules are recycled by deubiquitinating enzymes (DUBs). The figure was adapted from: van Tijn, P., Hol, E.M., van Leeuwen, F.W., and Fischer, D.F. (2008). The neuronal ubiquitin-proteasome system: murine models and their neurological phenotype. *Prog Neurobiol* 85, 176-193. Reprinted by permission from Elsevier Ltd: Progress in Neurobiology, copyright (2008). Elsevier license number 4151791383353.

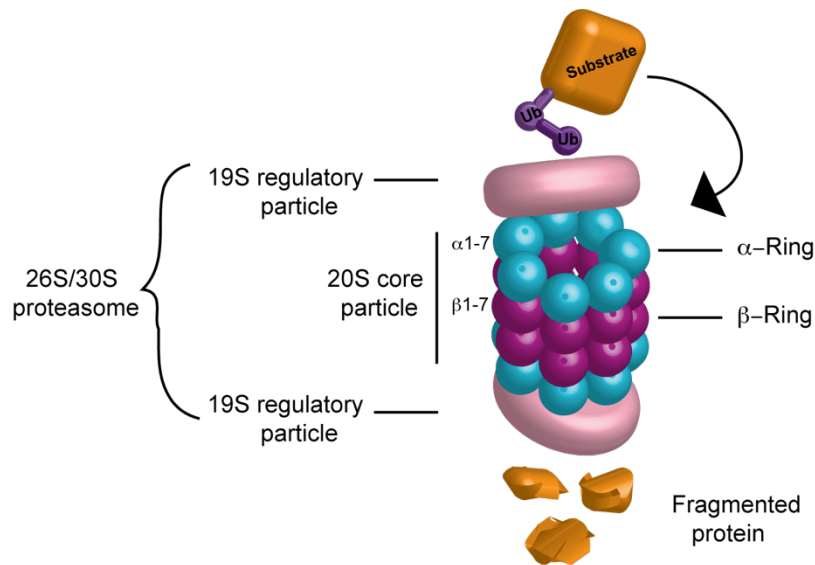


Figure 1.3.4 The 26S/30S proteasome.

Schematic of the 26S/ 30S proteasome, consisting of a 20S core particle (CP) and one or two 19S regulatory particles (RP). The CP is constituted of two α - and two β -rings, each made up of seven respective subunits. Proteins designated for degradation bind to the RP and are degraded by the CP.

1.3.1 E3 ubiquitin ligases

The degradation and post-translational modification of proteins by ubiquitination is a fine-tuned process that relies highly on its specificity for substrate recognition. It is therefore not surprising that the human genome encodes for over 600 different E3 ligases, which recognize substrates via unique protein-protein interactions (Deshaies and Joazeiro, 2009). In contrast, the human genome only encodes for two E1 enzymes and approximately 35 E2 enzymes, pinpointing E3 ligases as the main determinants in the specific process of ubiquitination (Kawabe and Brose, 2011; Scheffner et al., 1995). An E3 ligase can have more than one interaction partner and in return substrates can be ubiquitinated by various E3 ligases. This adds another layer of complexity to the regulation of protein homeostasis and cellular function. Depending on the mode of ubiquitin transfer, E3 ligases can be classified as RING-type or HECT-type ligases. In 'really interesting new gene' (RING) ligases, the E3 enzyme functions as a scaffold binding the E2 conjugating enzyme as well as the target protein and bringing both in close proximity for a direct ubiquitination. RING-ligases can exist as monomeric or multimeric complexes and are more abundant than HECT-ligases (Pickart and Eddins, 2004; Pickart and Fushman, 2004). 'Homologous to E6AP C-terminus' (HECT) ligases have intrinsic enzymatic activity: the E2 ligase is recruited to the E3 ligase and transfers the ubiquitin

molecule first onto the E3 enzyme before it is transferred onto the target substrate, which simultaneously binds to the E3 ligase (Komander and Rape, 2012) (**Figure 1.3.3**).

1.3.2 UPS dysfunctions are associated with neurodegenerative diseases

Like in any other cell type, the UPS plays a crucial role in neurons and glial cells. Dynamic changes or plasticity of the brain depend on the balance between synthesis and degeneration of proteins. Previous studies have shown that the UPS is essential for the functional and molecular reorganization of the postsynaptic density in rat hippocampal neurons in response to synaptic activity (Ehlers, 2003). Besides synaptic remodeling, axonal regeneration also relies on an efficient UPS. Interestingly, efficient UPS has been highlighted as part of the mechanism involved in new growth-cone formation after axonal injury (Verma et al., 2005). Glial cells are as essential to brain function as neurons and further contribute to its plasticity. When myelination hits its peak, myelinating cells produce myelin membrane at a daily rate that is equal to three times the weight of their soma (Jansen et al., 2014). Ensuring a stable homeostasis is therefore decisive for myelin integrity and involves the UPS. Studies from Goldbaum *et al.* show that inhibition of the proteasome by the inhibitor MG-132 induces apoptosis and mitochondrial dysfunction in cultured oligodendrocytes from rats (Goldbaum et al., 2006). In the PNS, the UPS was shown to participate in the response of Schwann cells to peripheral injuries. Inhibition of the UPS by MG-132 during the early phase of Wallerian degeneration of injured peripheral nerves induced a cell cycle arrest of Schwann cells and suppressed their dedifferentiation *in vivo* and *in vitro* (Lee et al., 2009). Further on, it has been reported for both rats and multiple myeloma patients, that treatment with the proteasome inhibitor Bortezomib caused a degeneration of Schwann cell myelin and peripheral neuropathy (Cavaletti et al., 2007; Filosto et al., 2007).

Proper protein turnover is not only vital during neurogenesis and gliogenesis, but the UPS provides also protection against age-associated changes in the adult brain. Disturbances in the UPS involving ubiquitination, deubiquitination or the proteasomal function are therefore associated with many different neurodegenerative diseases and forms of cancer. Hallmarks of major neurodegenerative diseases often include aggregates of protein within neurons and glial cells. Interestingly, these accumulations seen in tauopathies, synucleinopathies and polyglutamine diseases are thought to compromise the function of the overloaded UPS and contribute to the process of degradation (Bence

et al., 2001; Dantuma and Bott, 2014; Lindsten et al., 2002). At the same time, inclusion bodies often consist of ubiquitinated proteins, UPS components and proteasome subunits (Dantuma and Salomons, 2016). Further studies in affected neurons suggest that ubiquitin in inclusions may reflect an attempt by the cell to clear these aggregates via proteolytic systems (Yamamoto et al., 2000). However, it is currently unclear whether ubiquitinated proteins within inclusion bodies are the result of a dysfunctional UPS or whether it indicates a protective mechanism of the cell to manage the toxic aggregates. Neurofibrillary tangles, consisting of hyper-phosphorylated tau molecules are a hallmark of Alzheimer's disease (AD) and are intensively ubiquitinated (Perry et al., 1987). In addition, amyloid β peptide, the major constituent of amyloid plaques, another hallmark of AD, can interact with the proteasome and inhibit degradation of proteins (Gregori et al., 1995). Lewy bodies are a hallmark of Parkinson's disease (PD), which predominantly comprise α -synuclein. It has been shown that α -synuclein also binds to the proteasome and inhibits the UPS *in vitro* and *in vivo* (Chen et al., 2006; Snyder et al., 2003; Stefanis et al., 2001). In Huntington disease, ubiquitinated filamentous mutant huntingtin aggregates were found to selectively inhibit the peptidase activity of the 26S proteasome *in vitro* (Diaz-Hernandez et al., 2006).

In diseases affecting the PNS, it was observed that proteasome impairment in Schwann cells induces misfolding and aggregations of proteins like SIMPLE (small integral membrane protein of lysosome/late endosome) and the myelin proteins PMP22 (peripheral myelin protein 22) and MPZ (Lee et al., 2012a). These pathologies are associated with the peripheral neuropathy of demyelinating Charcot-Marie-Tooth disease, which is characterized by motor and sensory weakness as well as muscle wasting (Lee et al., 2012a). Glial cells are similarly affected as neurons, however the disparity in inclusions occurring in neurons as compared to glial cells implies that the UPS is more efficient in clearing out toxic aggregates within glial cells. While glial cells may cope better with these protein aggregates, they still are affected and contribute to the general outcome. In multiple system atrophy, α -synuclein aggregates have been shown to be present in oligodendrocytes (Asi et al., 2014; Dickson, 2012; Stefanova et al., 2009). Inhibition of the UPS in oligodendrocytes expressing α -synuclein aggregates, leads to a severe motor phenotype and effects neuronal function and integrity (Stefanova et al., 2012).

Astrocytes are able to take up aggregates of α -synuclein or amyloid β and secrete pro-inflammatory markers, which activate microglia and subsequently help to clear out aggregates (Mandrekar et al., 2009; Mulder et al., 2014; Wyss-Coray et al., 2003). Pro-inflammatory markers such as interferon γ induce the formation of immunoproteasomes in

glial cells that exhibit an exchange of β -subunits by immuno-subunits in the core particle of the proteasome. With this exchange, the catalytic activity in immunoproteasomes is increased and the cleavage pattern is altered, resulting in peptides that are subsequently presented to the MHC class-I molecule of the immune system (Basler et al., 2013; Sijts and Kloetzel, 2011). The inflammatory response of glial cells further leads to an up-regulation of the NF- κ B or JKN pathway, which are controlled by UPS components (Dalal et al., 2012; Stefanova et al., 2009). While it seems to be beneficial to up-regulate the inflammatory response and clear out toxic aggregates, it is unknown whether the induction of immunoproteasomes are beneficial or detrimental in neurodegenerative diseases in the long run, as chronic inflammation is known to contribute to the degeneration of neurons (Tansey et al., 2012).

1.4 *PARK* genes

Neurodegenerative diseases often have an unknown origin, also referred to as idiopathic origin. Parkinson's disease (PD) for example, which is one of the most prevalent neurodegenerative conditions, is caused in 85-90% of the cases by a sporadic event, while approximately 10% are due to an environmental cause and 5-10% occur as a result of an inherited genetic mutation (de Lau and Breteler, 2006). Even though genetic mutations linked to PD only occur quite rarely, studying their cause will help to elucidate the mechanisms involved in sporadic PD cases. Cellular dysfunctions that had been identified in genetic forms of PD have also been found in idiopathic PD. For instance, the first gene that was associated with familial PD was *SNCA*, which encodes for α -synuclein (Polymeropoulos et al., 1997). Only later α -synuclein was identified as major constituent of Lewy bodies in sporadic PD patients (Spillantini et al., 1997). *SNCA* is also known as *PARK1* or *4* and belongs to the 20 identified *PARK* genes, which are linked to familial PD. Among these *PARK* genes with their various functions, 3 loci are related to the UPS: *parkin*, *UCH-L1* and *FBXO7*.

Parkin (*PARK2*) encodes for an E3-ubiquitin ligase with multiple interaction partners. It is most prominently known to regulate mitochondrial function together with another *PARK* gene, *PINK1* (*PARK6*). Upon mitochondrial damage, *PINK1* accumulates at the outer membrane of the mitochondria and recruits *parkin*. *Parkin* then ubiquitinates outer membrane proteins and induces selective degradation of mitochondria (Pickrell and Youle, 2015). Mitochondrial impairment is shown in brains of sporadic PD patients in several studies before, however the critical pathway was previously unknown (Keeney et

al., 2006; Parker et al., 1989; Schapira et al., 1989). This newly identified pathway, shed light on mitochondrial contribution in PD and identified an underlying mechanism, which is also relevant in sporadic forms of PD (Wang, 2017).

UCH-L1 (PARK5) or ubiquitin carboxy-terminal hydrolase 1 is a deubiquitinating enzyme and part of the UPS. Its function lies in the recycling of monomeric ubiquitin molecules for new protein degradation and modification (Pickart, 2000). UCH-L1 is highly expressed in neurons and is required for axonal maintenance and integrity. Mutations in UCH-L1 lead to reduced intracellular ubiquitin levels, which restrain proper protein clearance and lead to an imbalanced protein turnover (McNaught et al., 2002; Osaka et al., 2003). Further on, UCH-deficient mouse models have shown that lack of UCH-L1 will lead to inclusion bodies in axonal terminals as well as motor and sensory ataxia, hind limb paralysis and premature death (Bishop et al., 2016).

Another *PARK* gene that encodes for a component of the UPS is *FBXO7 (PARK15)*. Since *FBXO7* is the subject of my study, I will explain the function of *FBXO7* in more detail in the following section.

Although the UPS provides a vital function in all different cell types, its role in myelinating cells is barely investigated. In oligodendrocytes it was reported that the SCF-E3 ubiquitin ligase *FBXW7* limits the myelin-promoting activity of mTOR (Kearns et al., 2015). The mechanistic target of rapamycin (mTOR) serine/threonine kinase was previously shown to be a powerful driver of myelination, however factors that would regulate mTOR activity were only poorly elucidated (Guardiola-Diaz et al., 2012; Tyler et al., 2009; Wahl et al., 2014). The study by Kearns *et al.* identified mTOR as direct target of *FBXW7* and showed in a mutant zebrafish model, in which *Fbxw7* was deleted from oligodendrocytes, that mTOR signaling activity was elevated, resulting in hypermyelination. Hence, under physiological conditions *FBXW7* limits myelination, while inhibiting mTOR activity and therefore acting as regulator of myelination during development (Kearns et al., 2015). Moreover *FBXW7* was reported to decrease Notch signaling, which blocks neurogenesis and promotes gliogenesis. This identified *FBXW7* as limiting factor of OPC-formation (Snyder et al., 2012). Another E3 ubiquitin ligase that regulates Notch signaling is called mind bomb-1 (MIB1). MIB1 promotes the endocytosis of Notch ligands and therefore the formation of progenitors designates for gliogenesis and was shown to suppress glial differentiation, when MIB1 was depleted (Kang et al., 2013).

In Schwann cells, mutations in the small integral membrane protein of lysosome/late endosome (SIMPLE) has been linked to CMT1C disease (Lee et al., 2012a). SIMPLE is involved in the UPS while interacting with the E3 ubiquitin ligase NEDD4 (Shirk et al.,

2005). Although its function is not fully understood, it is speculated that dysfunction of SIMPLE may lead to incorrect turnover of myelin proteins like PMP22, which have been found to be misfolded and aggregated in similar forms of CMT diseases (Kazunori Sango, 2014). Mutations in SIMPLE itself leads to aggregations and hence places a burden on the proteasome pathway (Kazunori Sango, 2014). Many mutations in PMP22 have been identified in mouse and human affected by CMT and have been shown to induce accumulations in the endoplasmic reticulum (ER) (D'Urso et al., 1990; Naef et al., 1997). A recent study showed that misfolded PMP22 at the site of ER is degraded by the E3-ubiquitin ligase HRD1/SYVN1, which mediates ER-associated degradation (ERAD) (Hara et al., 2014).

Peripheral nerve injury results in axonal degeneration and phenotypic changes in Schwann cells, which are critical for potential nerve regeneration or degeneration. These changes in Schwann cells require an efficient turnover and modification of proteins within Schwann cells. The E3 ubiquitin ligase ZNRF1 has been reported to be deregulated in Schwann cells following a nerve injury, but its function remains to be further investigated (Araki et al., 2001).

Taken together, these examples illustrate the importance of the UPS for the cellular function and show that dysfunction of the UPS induces neurodegenerative diseases. Its crucial role in myelinating cells however is only poorly understood and requires further investigation.

1.5 FBXO7

The *FBXO7* gene is located on chromosome 22q12-q13 and consists of nine exons (**Figure 1.5.5a**). There are three coding isoforms of the *FBXO7* mRNA transcript known, with isoform 1 being most abundantly expressed in all different types of tissue. Isoform 2 and 3 are shorter and harbor alterations in the first couple of exons at the 5 prime-end (Nelson et al., 2013) (**Figure 1.5.5b**). When translated, FBXO7 comprises distinct functional domains, which enable FBXO7 to be involved in various cellular mechanisms. At its N-terminus, FBXO7 contains an ubiquitin-related (UbR) domain, which is known to mediate its interaction with proteasome-linked proteins such as PSMA2 (Burchell et al., 2013; Cenciarelli et al., 1999; Kirk et al., 2008; Laman et al., 2005; Vingill et al., 2016). With its N-terminus, FBXO7 also interacts with parkin and together they regulate mitochondrial quality control (Burchell et al., 2013; Cenciarelli et al., 1999; Kirk et al., 2008; Laman et al., 2005; Vingill et al., 2016). The interaction of FBXO7 with the

cyclinD/CDK6 complex via the cyclin-dependent kinase 6 (CDK6) binding domain, mediates cell cycle regulation (Burchell et al., 2013; Cenciarelli et al., 1999; Kirk et al., 2008; Laman et al., 2005; Vingill et al., 2016). The FBXO7/PI31 (FP) domain is another prominent domain of FBXO7 that facilitates the interaction with the proteasomal inhibitor 31 (Burchell et al., 2013; Cenciarelli et al., 1999; Kirk et al., 2008; Laman et al., 2005; Vingill et al., 2016). The eponymous F-box domain, mediates the interaction to SKP1 and together with cullin1 and RBX1 forms the SCF-E3 ubiquitin ligase (Burchell et al., 2013; Cenciarelli et al., 1999; Kirk et al., 2008; Laman et al., 2005; Vingill et al., 2016). At its C-terminus, FBXO7 harbors a proline-rich repeat (PRR), which has been shown to be another site of interaction with cell cycle regulating molecules (Huang et al., 2003) (**Figure 1.5.5c**). All these specific domains facilitate the specific interaction of FBXO7 with its target substrates, as FBXO7 mainly acts as subunit of the cullin1-based SCF-E3 ubiquitin ligase (Cenciarelli et al., 1999; Winston et al., 1999; Zheng et al., 2002).

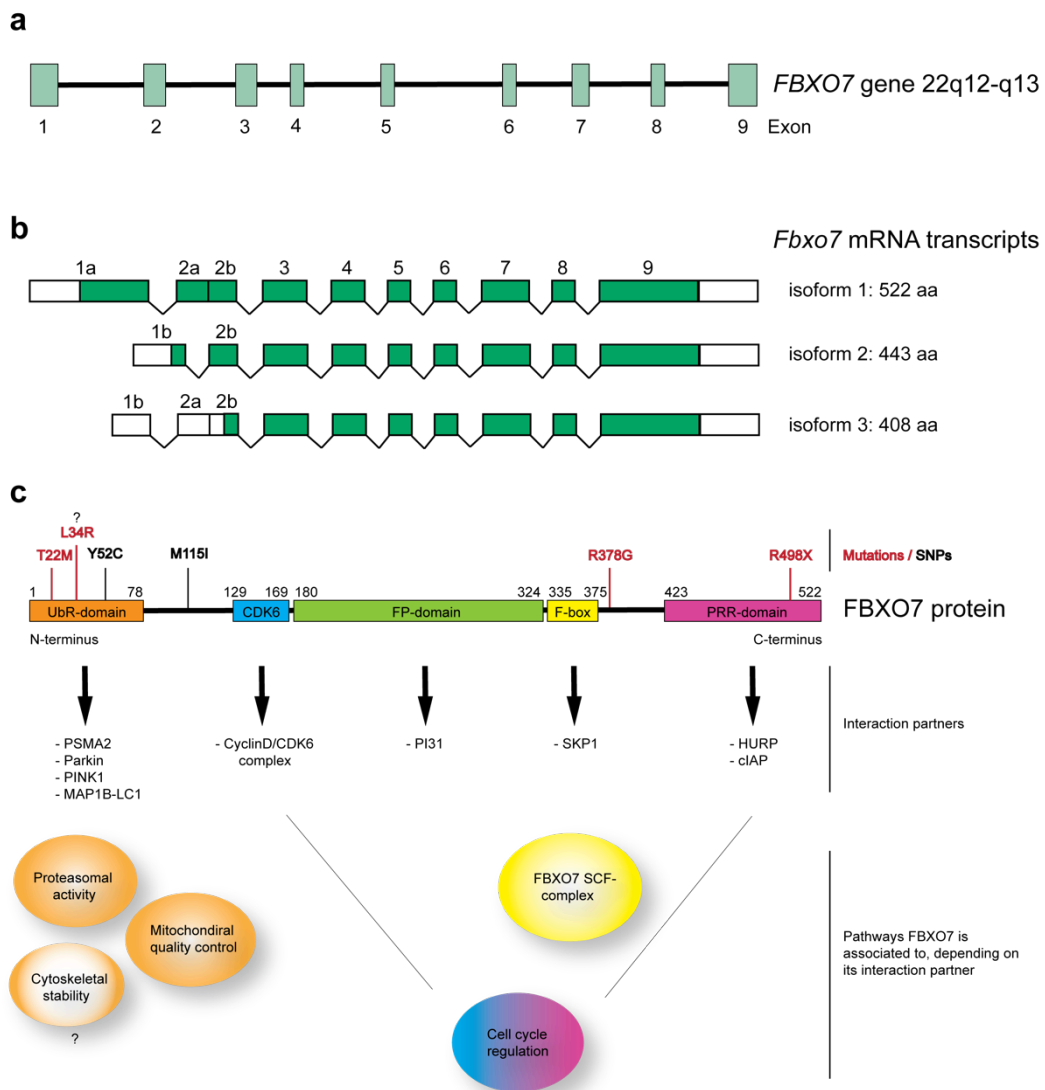


Figure 1.5.5 The *Fbxo7* gene and protein structure.

(a) Schematic of the human *FBXO7* gene, which is located at chromosome 22q12-q13 and harbors 9 exons. (b) Illustration of the 3 protein coding mRNA transcripts of *FBXO7* and the protein size of each isoform. (c) The protein construct of *FBXO7* isoform 1 and its distinctive domains. Pathogenic mutations of *FBXO7*, which are linked to PPS are labeled in red, while SNPs are indicated in black. The pathways, in which *FBXO7* is associated to, are sorted according to the domain, by which *FBXO7* interacts with its substrates. UbR: ubiquitin-related domain; CDK6: cyclin-dependent kinase 6 binding domain; FP: *FBXO7*/PI31 domain; PRR: prolin-rich-region. Modified from Nelson *et al.* (Nelson *et al.*, 2013).

1.5.1 SCF-E3 ubiquitin ligase

Together with SKP1, cullin1 and RBX1, the adaptor molecule *FBXO7* forms the multimeric SCF-complex. While *CUL1*, *RBX1* and *SKP1* constitute the core of the complex, *FBXO7* is the substrate-recruiting subunit. As a result, *FBXO7*-SCF brings the E2 enzyme and substrate in close proximity for ubiquitin transfer. The SCF-E3 ubiquitin ligase is categorized as RING-type ligase. At a closer look, the subunit of the SCF-complex, cullin1 (*CUL1*) acts as scaffold protein. It binds the RING-box protein 1 (*RBX1*), which recruits the E2 conjugating enzyme and also binds the small adaptor protein S-phase kinase-associated protein 1 (*SKP1*). *SKP1* in turn binds the respective F-box protein (FBP), like F-box only protein 7 (*FBXO7*) (Cardozo and Pagano, 2004) (**Figure 1.5.6**). Based on the structural motifs, FBPs are categorized as: FBXLs, which contain leucine rich repeats, FBXWs that harbor a specific WD40 domain and FBXOs with no or other structural motifs (Jin *et al.*, 2004). FBPs are the subunits responsible for the decisive step of interaction and recruitment of target substrates, which are designated for ubiquitination.

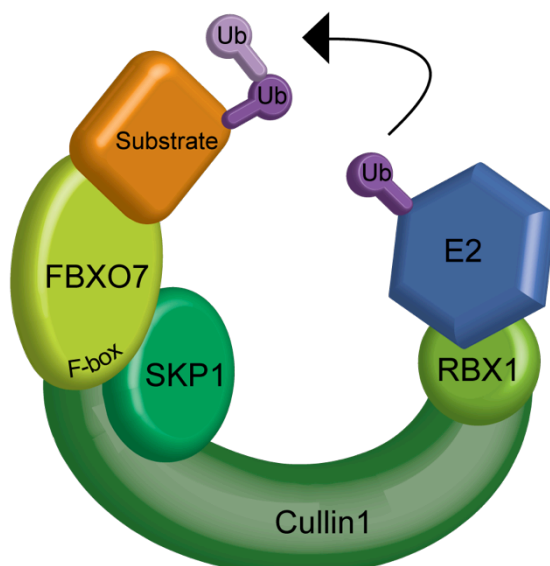


Figure 1.5.6 The *FBXO7* SCF-E3 ubiquitin ligase.

Schematic representation of the SKP1-cullin1-*FBXO7* complex, which mediates the ubiquitination of a target substrate, while simultaneously binding the E2-conjugating enzyme and the substrate. The *FBXO7* SCF-ligase belongs to the RING-type E3-ubiquitinating ligases. Ub: ubiquitin; SKP1: S-phase kinase-associated protein1; RBX1: RING-box1.

1.5.2 Interaction partners of FBXO7

FBXO7 has multiple interaction partners and is involved in various pathways. It was first identified in a yeast two-hybrid analysis together with other F-box proteins, while using SKP1 as bait (Cenciarelli et al., 1999; Winston et al., 1999). After establishing its participation in the SCF-E3 ubiquitin ligase, different studies searched for the interactors and ubiquitination substrates of FBXO7. Soon after, the first interaction partner of FBXO7 and target of ubiquitination was found – HURP (Hsu et al., 2004). The hepatoma up-regulated protein (HURP) is localized at the spindle poles during mitosis. Its abundance is tightly regulated during the cell cycle, with elevated levels of HURP during the G₂/M phase (Chen et al., 2014b; Tsou et al., 2003). FBXO7 interacts with HURP via its C-terminal proline-rich repeat (PRR) and ubiquitinates HURP depending on its phosphorylation by the cyclin B/CDK1 complex (Huang et al., 2003).

FBXO7 was further shown to be involved in cell cycle regulation, when the cyclin D/CDK6 complex was identified as additional interaction partner of FBXO7 (Laman et al., 2005). Within the cyclinD/CDK6 complex, cyclin D activates the cyclin-dependent kinase 6 (CDK6) and converts growth signals into signals for cell cycle progression (Morgan, 1995; Sherr, 1996). It is anticipated that FBXO7 interacts with the cyclinD/CDK6 complex in a ligase-independent manner and promotes a positive regulation of the complex, since knockdown of FBXO7 reduces the levels of cyclinD/CDK6 assembly in immortalized fibroblasts (Laman et al., 2005). FBXO7 interacts with CDK6 by its CDK6-binding domain. Since FBXO7 was found to be present in colon and lung carcinomas but absent in healthy colon and lung tissue, *FBXO7* is suggested to be a potential oncogene (Laman, 2006; Laman et al., 2005). This positive influence of FBXO7 on the cell cycle regulation and proliferation is however only interesting for mitotic cells, rather than for the majority of post-mitotic cells found in the nervous system.

In contrast, FBXO7 has an anti-proliferative function in hematopoietic precursor cells where it promotes the maturation of precursor cells (Meziane et al., 2011). The reduction of FBXO7 in a hypomorphic mouse model resulted in anemia (Randle et al., 2015).

Other proteins that have been reported to be directly ubiquitinated by FBXO7 are the cellular inhibitor of apoptosis 1 (cIAP1) and TNF receptor associated factor 2 (TRAF2) (Chang et al., 2006; Kuiken et al., 2012). Both proteins are involved in the NF- κ B pathway, which is responsible for promoting cell survival by inhibition of apoptosis and initiates an

immune response (Chen and Goeddel, 2002). By ubiquitinating cIAP1 and TRAF2, FBXO7 reduces their function as indirect NF- κ B activators and therefore decreases the NF- κ B signaling pathway (Kuiken et al., 2012). It is anticipated that the ubiquitination of TRAF2 by FBXO7 initiates protein degradation, however so far little is known about the consequences of ubiquitination by FBXO7 for cIAP1 and TRAF2 (Chen et al., 2014a).

Recently, FBXO7 was also shown to be involved in mitochondrial quality control, while interacting with parkin and PINK1. FBXO7 mediates the recruitment of parkin to the depolarized mitochondrial membrane and acts as scaffold protein for the interaction of parkin and PINK1 (Burchell et al., 2013; Scarffe et al., 2014). Further studies show that mutant forms of FBXO7 aggregate in mitochondria and inhibit mitophagy, which eventually leads to increased generation of reactive oxygen species, depolarization of mitochondrial membrane and less ATP production (Delgado-Camprubi et al., 2017; Zhou et al., 2015). However, the exact role of FBXO7 in the mitochondrial maintenance and mitophagy still remains to be further elucidated.

As an E3-ubiquitin ligase, FBXO7 is part of the UPS, but in the past years its interaction with the proteasome could not be thoroughly proven. FBXO7 was first speculated to interact with the proteasome, since it harbors an ubiquitin-related (UbR) domain at its N-terminus, which is commonly shared in proteins that regulate proteasomal function (Hartmann-Petersen and Gordon, 2004). Then, PI31 was discovered as interaction partner of FBXO7 and was shown to share a dimerization domain with FBXO7 – the FBXO7-PI31 (FP) domain (Kirk et al., 2008). The proteasomal inhibitor 31 (PI31) regulates the formation of immunoproteasomes *in vivo* and inhibits the 20S proteasome *in vitro* (McCutchen-Maloney et al., 2000; Zaiss et al., 2002). However its detailed functional relevance and interaction with FBXO7 remained unknown. Recently, our group introduced a novel interaction partner of FBXO7, which is part of the proteasome. With a yeast two-hybrid screen, my colleagues identified the proteasomal subunit α 2 (PSMA2) as direct interactor and ubiquitination substrate of FBXO7. PSMA2 is a subunit of the 26S core particle of the proteasome and like other α -subunits it is crucial for the structural stability and binding of the regulatory particle. In addition, it regulates the access to the proteolytic chamber of the proteasome (Finley, 2009). My colleagues showed that FBXO7 interacts with PSMA2 via its UbR domain and induces a K63-linked ubiquitination, which may lead to a functional modification of PSMA2. *In vitro* and *in vivo* experiments revealed that deletion of FBXO7 reduced proteasome activity. While searching for the cause of decreased activity, FBXO7 was reported to not interfere with the gating and proteolytic activity of the proteasome holoenzyme, but that loss of FBXO7 significantly increases the abundance of free core and regular particles *in vivo* and *in vitro*. Therefore our group

could demonstrate that FBXO7 is a proteasome-associated protein involved in proteasome assembly and activity (Vingill et al., 2016).

In the same yeast two-hybrid screening, my colleague Dr. David Brockelt could also identify the light chain1 of the microtubule-associated protein 1B (MAP1B-LC1), MAP1A-LC2 and MAP1S as novel and potential interactor of FBXO7. MAPs are part of the cytoskeleton arrangement and stabilize microtubules (Mandelkow and Mandelkow, 1995). MAP1A and MAP1B are predominately expressed in neurons and are important for axonal growth, while MAP1S is ubiquitously expressed in different tissues (Noiges et al., 2002; Orban-Nemeth et al., 2005). Microtubules provide a structural network in neurons and form tracks for organelle transport, like mitochondrial transport (Jimenez-Mateos et al., 2006; Mandelkow and Mandelkow, 1995). In an additional mapping analysis Dr. Brockelt could demonstrate that the mitochondrial aggregation and genome destruction (MAGD) domain of MAPs is the specific region of interaction with FBXO7. While performing an ubiquitination assay, David showed that MAP1B-LC1 and MAP1A-LC2 are ubiquitinated by FBXO7 and hypothesized a potential K63 lineage of ubiquitination. However further experiments *in vitro* and *in vivo* are required to elucidate the interaction of MAPs and FBXO7, as well as their function (Brockelt, 2015).

1.5.3 Mutation in *PARK15*

Autosomal-recessive mutations in the *FBXO7* gene were identified in genome-wide linkage analysis of Parkinsonian-Pyramidal Syndrome (PPS) affected family members and soon after *FBXO7* was established as a parkinsonism-associated gene (*PARK15*) (Di Fonzo et al., 2009; Shojaee et al., 2008). Mutations in *FBXO7* cause an early-onset form of parkinsonism, referred to as Parkinsonian-Pyramidal syndrome. Patients affected by PPS display a broad spectrum of disorders, ranging from only Parkinsonism signs, to only Pyramidal tract signs and a mixed form of Parkinsonism and Pyramidal signs, as it is seen in majority of the cases (Di Fonzo et al., 2009; Lohmann et al., 2015; Shojaee et al., 2008). Typical clinical symptoms of Parkinsonism include dyskinesia, rigidity, tremor and postural instability, while spasticity, impaired fine movement and Babinski sign characterize Pyramidal tract signs. Pyramidal tract lesions eventually affect the performance of muscles, which can react with stiffness but also show muscle weakness. PPS patients can have one or more of the listed symptoms and often show additional signs including dystonia, dysphagia, dysarthria, cortical atrophy and/or cognitive decline (Di Fonzo et al., 2009; Lohmann et al., 2015). PPS therefore represents a wide-ranged

disease with a heterogenic pattern of symptoms and signs, but with a disease causing mutation in the *FBXO7* gene that is common to all PPS cases. Different mutations of *FBXO7* have been identified, which include the homozygous missense mutation Arg378Gly, a homozygous nonsense mutation Arg498X and the compound heterozygous mutation of a missense mutation Thr22Met, together with a mutation at the internal splice site (IVS7+1G/T) (Di Fonzo et al., 2009; Shojaee et al., 2008). Recently, new single nucleotide polymorphism (SNP) variants of *Fbxo7* have been found at the side of Tyr52Cys and Met115Ile (Chen et al., 2014a). Moreover, the additional homozygous missense mutation Leu34Arg has been found (Lohmann et al., 2015). However these new mutations remain to be validated, since the novel missense mutation was not further investigated and an association study of the two SNPs, regarding an increased risk of PD was not entirely conclusive (**Figure 1.5.5c**).

Aim of the study

Studies on the role of the UPS in neurodegenerative diseases mainly focus on neurons, as these cell types appear to be affected the most. Lately however, an increasingly important role of glial cells is emerging in neurodegenerative disease. While some studies investigated UPS dysfunction in astrocytes and microglia, very little is known about its influence in myelinating cells. Alterations in the UPS may not only affect the protein homeostasis in myelinating cells, but also impact neuronal function, since both cell types engage in a close interaction, that provides mutual support. Thus, further investigations on the axon-glia interaction and influence of the UPS are crucial to understand the pathophysiological changes in neurodegenerative diseases.

In this study, I investigated the role of the E3-ubiquitin ligase FBXO7 in myelinating cells and its influence on the axon-glia axis. To pursue this goal, we generated a conditional mouse line, in which FBXO7 was deleted from myelinating cells, as FBXO7 is highly expressed in the white matter of cerebellum and corpus callosum. The analyses included the examination of myelinating cells of the CNS and PNS, and associated axons. With this study, I aimed at elucidating the importance of the UPS in myelinating cells and its influence on axonal support. By setting the focus on myelinating cells, it will give a new perspective on neurodegenerative diseases like Parkinsonian-Pyramidal syndrome and contribute to a further understanding and potential therapies for related diseases.

2. Materials and methods

2.1 Materials

2.1.1 Lab equipment and consumables

The following lab equipment was used during the experiments: plastic ware was purchased from Eppendorf (Hamburg, Germany), Sarstedt AG (Nürnbrecht, Germany), Thermo Fisher Scientific (Waltham, USA), Falcon BD (Le Pont de Claix, France), Gilson (Middleton, USA), Corning (New York, USA) and Greiner Bio-One (Frickenhausen, Germany). Pipettes were bought from Gilson, centrifuges from Eppendorf and Thermo Fischer Scientific, heating blocks from Grant Instruments (Shepreth, UK), horizontal platform shakers from Heidolph instruments (Schwabach, Germany) and thermocyclers from Biometra (Göttingen, Germany). The spectrophotometer was obtained from GE Healthcare (New Jersey, USA), the microplate reader from Tecan (Männedorf, Switzerland) and the thermoshaker from Biometra as well as the gel documentation and UV transilluminator system. Power supplies together with all equipment needed for gel electrophoresis were purchased from Biometra or Bio-Rad (Herkules, USA). Microscopes used in this study included the dissection microscope SMZ645 from Nikon (Tokyo, Japan), the light microscope Axiophot from Carl Zeiss (Oberkochen, Germany), the inverted light microscope Eclipse TS 100 from Nikon, the fluorescent microscope BX51 from Olympus (Tokyo, Japan) as well as the Eclipse TI from Nikon. Glassware was used from Schott Duran (Wertheim, Germany), syringes and needles were bought from B. Braun (Melsungen, Germany) and the peristaltic pump drive 5001 was purchased from Heidolph instruments. The rotarod was acquired from Ugo Basile (Monvalle, Italy), all other tools used for mouse behavior analyses were custom-made by the fine mechanical workshop of Max-Planck Institute of Experimental Medicine. The tissue processor HMP 110 was from Microm and the microtome HM 430 from Thermo Fischer Scientific. The cryostat CM3050 S that was used, was from Leica Biosystems (Wetzlar, Germany) and the histo bath HIR-3 was bought from Kunz instruments (Stockholm, Sweden). For cell culture experiments a biological safety cabinet from HERAsafe® by Kendro (Hanau, Germany) was used and the incubator Hera cell 150, was also purchased from Kendro. The water bath was obtained from Memmert (Schwabach, Germany).

2.1.2 Chemicals and reagents

Unless mentioned otherwise, the chemicals used in this study were mainly obtained from Merck Millipore (Darmstadt, Germany), Macherey-Nagel (Dueren, Germany) Sigma-Aldrich (Munich, Germany), Roth (Karlsruhe, Germany), AppliChem (Darmstadt, Germany) Biomol (Hamburg, Germany), Serva Electrophoresis (Heidelberg, Germany), Invitrogen (Darmstadt, Germany), Becton Dickinson and Company (Heidelberg, Germany), Worthington (New Jersey, USA), DAKO (Carpinteria, USA), GE Healthcare, New England BioLabs (Frankfurt, Germany), Promega (Fitchburg, USA), Zytomed Systems (Berlin, Germany) or Th. Geyer (Erlangen, Germany).

Cell culture reagents that were used included Dulbecco's modified eagle's medium (DMEM), Hank's balanced salt solution (HBSS), basal medium eagle (BME), Opti-MEM reduced serum medium, GlutaMAX™, Pen-Strep-Glutamine (PSG), B27 supplement and 0.5% Trypsin-EDTA, which were all purchased from Gibco by Life Technologies (Carlsbad, USA). Poly-L-Lysin (PLL) and goat serum (GS) were bought from Sigma-Aldrich, Trypsin from Worthington, fetal bovine serum (FBS) from Biochrom (Berlin, Germany), calf serum (CS) from Hyclone (Utah, USA), horse serum (HS) from PAA (Coelbe, Germany) and Lipofectamine® 2000 from Invitrogen.

Further on DNA and protein ladders, as well as the ECL western blotting solutions were acquired from Thermo Fischer Scientific. Protein A-Sepharose beads were purchased from GE Healthcare, albumin fraction V from AppliChem and Bio-Rad Protein Assay was from Bio-Rad. Xylazine also known as Rompun was bought from CP Pharma (Burgdorf, Germany) and Ketamine was from Medistar Arzneimittelvertrieb GmbH (Ascheberg, Germany).

2.1.3 Enzymes

A detailed list of used enzymes in this study is shown in **Table 2.1.1**.

Table 2.1.1 List of enzymes used in the study.

Enzyme	Application	Supplier
Proteinase K	Protein digestion	AppliChem
GoTag® DNA polymerase	Polymerase chain reaction	Promega
Superscript III reverse transcriptase	RT-PCR	Invitrogen

2.1.4 Kits

Commercial kits that were used for experiments are listed in **Table 2.1.2**.

Table 2.1.2 List of commercially available kits used in this study.

Kit	Application	Supplier
Nucleobond® Xtra Midi EF Kit	DNA isolation	Macherey-Nagel
SuperScript® III First strand synthesis kit	cDNA synthesis	Invitrogen
SYBER® green	RT-PCR	Thermo Fischer Scientific
Pierce™ Silver Stain Kit	Silver staining	Thermo Fischer Scientific
LSAB₂	Immunohistochemistry	Dako
DAB Zytomed kit	Immunohistochemistry (Veitenhansl et al.)	Zytomed Systems GmbH
DeadEnd™ Fluorometric TUNEL system	Immunohistochemical staining	Promega
Bio-Rad Protein assay	Protein measurement (Bradford)	Bio-Rad
Bio-Rad DC Protein assay	Protein measurement (Lowry)	Bio-Rad
Pierce™ ECL substrate	Western blotting	Thermo Fischer Scientific

2.1.5 Software

In order to record and analyze the mouse behavioral open field and elevated plus maze test, the software Viewer from Biobserve (St. Augustin, Germany) was applied. Moreover immunohistochemical quantification was obtained using ImageJ and various plug-ins accordingly. Pictures were edited using Adobe Photoshop and Illustrator. For statistical analysis and plotting of acquired data, Microsoft Excel and GraphPad Prism were used in this study.

2.1.6 Antibodies

The following primary and secondary antibodies were used for experiments and are listed in **Table 2.1.3** and **Table 2.1.4**. These were purchased from Biolegend (San Diego, USA), Merck Millipore (Darmstadt, Germany), Sigma-Aldrich (Munich, Germany), Santa Cruz Biotechnology (Dallas, USA), Leica Biosystems, Becton Dickinson and Company (Heidelberg, Germany), Wako Chemicals GmbH (Neuss, Germany), Cell Signaling Technology (Cambridge, UK) and Dianova (Hamburg, Germany).

Table 2.1.3 List of commercially available primary antibodies used in this study.

IHC (Immunohistochemistry), WB (Western blot).

Primary antibody	Host species	Application	Dilution	Supplier
α-APP 6E10	mouse monoclonal	IHC	1:200	Biolegend
α-CNPase	mouse monoclonal	WB	1:500	Sigma-Aldrich
α-Cullin1	mouse monoclonal	WB	1:50	Santa Cruz Biotechnology
α-FBXO7	mouse monoclonal	WB	1:50	Santa Cruz Biotechnology
α-Flag	mouse monoclonal	WB	1:1000	Sigma-Aldrich
α-GFAP	mouse monoclonal	IHC	1:200	Leica Biosystems
α-GSTπ1	mouse monoclonal	WB	1:250	BD Biosciences
		IHC	1:200	
α-Iba1	rabbit polyclonal	IHC	1:1000	Wako Chemicals GmbH
α-Mac3	mouse monoclonal	IHC	1:200	BD Biosciences
α-MBP	rabbit monoclonal	IHC	1:200	Cell Signaling Technology
α-Myc	mouse monoclonal	WB	1:1000	Santa Cruz Biotechnology
α-NG2	rat monoclonal	WB	1:200	Dr. Hauke Werners lab
α-PLP	mouse monoclonal	WB	1:50	Prof. Dr. Mikael Simons lab
		IHC	1:200	
α-PSMA2	mouse monoclonal	WB	1:1000	Cell signaling
α-γTubulin	mouse monoclonal	WB	1:1000	Sigma-Aldrich

Table 2.1.4 List of commercially available secondary antibodies used in this study.

IHC (Immunohistochemistry), WB (Western blot).

Secondary antibody	Host species	Conjugated substrate/dye	Application	Dilution	Supplier
α-mouse IgG	goat	HRP	WB	1:10000	Dianova
α-mouse IgG	goat	Cy2/Alexa 488	IHC	1:1000	Dianova
α-mouse IgG	goat	Cy3/Alexa 555	IHC	1:1000	Dianova
α-rabbit IgG	goat	HRP	WB	1:10000	Dianova
α-rabbit IgG	goat	Cy2/Alexa 488	IHC	1:1000	Dianova
α-rabbit IgG	goat	Cy3/Alexa 555	IHC	1:1000	Dianova

2.1.7 Buffers and stock solutions

Buffers and solutions that were used during the course of this study are listed below.

- **Buffer for MSC80 cells**

MSC80 medium: DMEM [+] 4.5g/l glucose [-] glutamine [-] pyruvate, 10% horse serum, 1% GlutaMAX™

- **Buffers and media for HEK293T cells and transfection**

HEK293T medium: DMEM [+] 4.5g/l glucose [-] glutamine [-] pyruvate, 10% FBS, 1% GlutaMAX™

2xHBSS: 50mM HEPES, 10mM KCl 280mM NaCl, 15mM glucose, 1.5mM Na₂HPO₄ in sterile H₂O, pH 7.11

2.5M CaCl₂

Trypsin/EDTA: 10% HBSS(10x), 10% Trypsin/EDTA(10x) in sterile H₂O, pH 7.0

- **Buffers and reagents necessary for biochemical techniques**

Triton®X-100 lysis buffer: 1% Triton®X-100, 150mM NaCl, 50mM Tris-HCl pH 7.5, 1mM EDTA in distilled H₂O (1:1600 aprotinin, 1:1000 pepstatin, leupeptin, Dithiothreitol)*

Co-IP buffer: 1% Nonidet P40, 150mM NaCl, 20mM Tris-HCl pH 7.5, 1mM EDTA, 10% glycerol in distilled H₂O

RIPA buffer: 0.1% SDS, 1% Nonidet P40, 0.5% sodium deoxycholate, 150mM NaCl, 50mM Tris-HCl pH 8.0, 5mM EDTA in distilled H₂O

SDS sample buffer (4x): 300mM Tris-HCl pH 6.8, 50% glycerol, 50% Upper buffer, 10% SDS, 25% β-Mercaptoethanol, 0.05% bromophenol blue in distilled H₂O

- **Buffers used for SDS-PAGE**

Lower buffer: 1.5M Tris, 0.4% SDS in distilled H₂O, pH 8.8

Upper buffer: 0.5M Tris, 0.4% SDS in distilled H₂O, pH 6.8

Running buffer: 125mM Tris, 1.25M glycine, 0.5% SDS in distilled H₂O

Transfer buffer: 20mM Tris 153mM glycine 20% methanol in distilled H₂O

PBS: 137mM NaCl, 10mM KCl, 20mM Na₂HPO₄, 20mM KH₂PO₄ in distilled H₂O, pH7.4

PBST: 1xPBS, 0.1% Tween-20

Blocking buffer: PBST, 4% milk powder

Antibody solution: 3% BSA, 0.02% NaN₃ in PBS

- **Buffers used for genotyping**

Tail lysis buffer: 10mM Tris pH 8.0, 10mM EDTA, 0.5% SDS, 200mM NaCl*, 3µg/µl Proteinase K*

2xTAE buffer: 80mM Tris-acetate, 2mM EDTA in distilled H₂O, pH 8.5

- **Buffers and reagents used for the proteasome activity assay**

Proteasome lysis buffer: 50mM Tris-HCl pH 7.5, 250mM sucrose, 5mM MgCl₂, 0.5mM EDTA, 2mM ATP*, 1mM DTT*, 0.025% Digitonin* in distilled H₂O

Proteasome assay buffer: 50mM Tris-HCl pH 7.5, 40mM KCl, 5mM MgCl₂, 0.5mM ATP*, 1mM DTT* in distilled H₂O

- **Buffers used for myelin preparation**

TBS: 1370mM NaCl, 200mM Tris-HCl in distilled H₂O, pH 7,4

- **Buffers and reagents used for immunohistochemistry**

Anesthetics

Ketamine/Xylazine: 10% Ketamine, 5% Xylazine in sterile PBS

Perfusion

4% PFA for perfusion: 40% of 0.2M NaH₂PO₄, 10% of 0.2M Na₂HPO₄, 50% of 4% Paraformaldehyde in sterile H₂O (6g PFA in 75ml H₂O), pH 7.4

Embedding of Tissue

4% PFA for tissue: 4g Paraformaldehyde, 4g sucrose in 100ml PBS

1% PFA for tissue: 3ml 4%PFA for tissue, 1ml PBS

Gallyas silver impregnation on paraffin sections

Incubating solution: 12.5mM NH₄NO₃, 5.9mM AgNO₃, 3mM NaOH in distilled H₂O

Developing solution: 50% solution A + 35% solution B + 15% solution C

Solution A: 472mM Na₂CO₃ in distilled H₂O

Solution B: 25mM NH₄NO₃, 11.8mM AgNO₃, 3.5mM Silicotungstic acid in distilled H₂O

Solution C: 25mM NH₄NO₃, 11.8mM AgNO₃, 3.5mM Silicotungstic acid, 1.89% formaldehyde in distilled H₂O

DAB staining on paraffin sections

Citrate buffer: 1.8% solution D + 8.2% solution E in distilled H₂O, pH 6.0

Solution D: 0.1M citric acid in distilled H₂O

Solution E: 0.1M sodium citrate in distilled H₂O

Tris buffer: 15.5mM NaCl, 50mM Tris-HCl in distilled H₂O, pH 7.6

Tris buffer + Milk: 2% milk powder in Tris buffer

Blocking buffer: 20% goat serum in BSA/PBS

BSA/PBS: 1% BSA in PBS

Immunofluorescence staining of cryo-sections and free floating sections

Solution to store free floating samples: 0.02% NaN_3 in PBS

Blocking solution: 10% goat serum, 2% BSA, 0.5% TX-100 in PBS

Antibody solutions: 10% goat serum, 2% BSA in PBS

Mounting media

Mowiol mounting media: 6g glycerol (85%), 2.4g Mowiol 4-88, 6ml H_2O , 12ml 0.2M Tris-HCl pH 8.5, 25mg/ml DABCO

Eukitt: [commercially available from Kindler (Freiburg, Germany)]

Aqua-poly/Mount: [commercially available from Polysciences (Eppelheim, Germany)]

Electron microscopy stainings

Karlsson and Schultz buffer: 0.36g $\text{NaH}_2\text{PO}_4 \cdot \text{H}_2\text{O}$, 3.1g $\text{Na}_2\text{HPO}_4 \cdot 2\text{H}_2\text{O}$, 1g NaCl in 100ml distilled H_2O , 25%(20ml) glutaraldehyde, 16%(50ml) formaldehyde, 30ml distilled H_2O

Epon: 21.4g glycidether, 14.4g Dodecenyl succinic anhydride (DDSA), 11.3g methylacid anhydride (MNA) and 0.84ml DMP-30

Methylene blue: 1% sodium tetraborate and 1% methylene blue in H_2O

Azure II staining solution: 1% Azure II in H_2O

* = added freshly before use

2.1.8 Mammalian cell lines

In the course of this study different immortalized cell lines were used as listed in **Table 2.1.5**.

Table 2.1.5 Immortalized cell lines used for experiments.

Cell name	Tissue type	Tissue	Phenotype
HEK-293T	Human	Kidney	Adherent
MSC80	Mouse	Schwann cell	Adherent

2.1.9 Plasmid constructs and primers

For biochemical experiments different plasmid constructs and primers were used as shown in Table 2.1.6.

Table 2.1.6 Plasmid constructs and primers used in this study.

Fwd (forward), rev (reverse) and bp (base pair).

Plasmid constructs for transfection

Vector plasmid	Constructed by
p3xFLAG-CMV10- <i>Fbxo7</i> wt	Siv Vingill
p3xFLAG-CMV10- <i>Fbxo7</i> Δ fbx	David Brockelt
pCMV-myc- <i>Skp1</i>	Judith Stegmüller
pcDNA3- <i>BCL^{XL}</i>	Azad Bonni
pSUPER- FBXO7 shRNA 1	Siv Vingill
pSUPER- FBXO7 shRNA 4	Siv Vingill
pSUPER- PSMA2 shRNA 1	Siv Vingill
pSUPER- PSMA2 shRNA 7	Siv Vingill

Primers for genotyping

Gene	Sequence	Size	Primer number
floxed <i>Fbxo7</i> (fwd)	5'-tcagcatgggttgtaagcatctacta-3'		23988
floxed <i>Fbxo7</i> (rev)	5'-ggctagatctcgcacataactctgtata-3'	600bp	22243
wild type <i>Fbxo7</i> (fwd)	5'-gggctgtatgaaggaagtgtatt-3'		31214
wild type <i>Fbxo7</i> (rev)	5'-ccctgagagtgagggtgctgttc-3'	800bp	31215
Cre (fwd)	5'-caggggtgtataagcaatccc-3'		04193
Cre (rev)	5'-cctggaaaatgcttctgtccg-3'	250bp	04192

Primers for RT-PCR

Gene	Sequence	Primer number
<i>IL-10</i> (fwd)	5'-atgcaggactttaagggttacttg-3'	33860
<i>IL-10</i> (rev)	5'-tagacaccttggtcttgagctta-3'	33861
<i>IL-1RA</i> (fwd)	5'-cagttccaccctgggaaggt-3'	33858
<i>IL-1RA</i> (rev)	5'-gagcggatgaaggtaagcg-3'	33859
<i>IL-1β</i> (fwd)	5'-cctgcagctggagagtgtgga-3'	33157
<i>IL-1β</i> (rev)	5'-cccatcagaggcaaggaggaa-3'	33158
<i>IL-6</i> (fwd)	5'-cggagaggagacttcacagagga-3'	22936
<i>IL-6</i> (rev)	5'-ggagagcattggaattgggg-3'	22937
<i>Tnf-α</i> (fwd)	5'-gcggtgctatgtctcagcc-3'	22942

<i>Tnf-α</i> (rev)	5'-tgaggagcacgtagtcgggg-3'	22943
<i>Ip-10</i> (fwd)	5'-ctgcctcatcctgctgggtctg-3'	12127
<i>Ip-10</i> (rev)	5'-ataggctcgcagggatgattcaagc-3'	12128
<i>Mcp1</i> (fwd)	5'-ggtcctgtcatgcttctgggc-3'	12125
<i>Mcp1</i> (rev)	5'-agcagggtcccaaagaagctgtagt-3'	12126
β - <i>Actin</i> (fwd)	5'-cgtgcgtgacatcaaagagaagctg -3'	6956
β - <i>Actin</i> (rev)	5'-ggatgccacaggattccataccaag -3'	6957
<i>Fbxo7</i> (fwd)	5'-tggaagtcaagtgggtatac-3'	31241
<i>Fbxo7</i> (rev)	5'-tactccagcagcaacgtagga-3'	31242
<i>Gapdh</i> (fwd)	5'-aggaacacggaaggccatg -3'	4876
<i>Gapdh</i> (rev)	5'-atggcccctctggaagct -3'	4877

Target sequence of shRNA

shRNA	Functionality	Sequence	Target region (human)
FBXO7 shRNA 1	functional	5'-gaagagaccttggttcata-3'	178-197 bp
FBXO7 shRNA 4	non-functional	5'-gaaactacgcatctccgac-3'	1017-1037 bp
PSMA2 shRNA 1	non-functional	5'-gctgactacattcagccc-3'	27-45 bp
PSMA2 shRNA 7	functional	5'-ggattacttggtgctgcatagc-3'	680-700 bp

2.2 Methods

2.2.1 Cell culture

All experiments regarding cell culture were performed in a sterile hood under sterile conditions. The cells were kept for growth in a 37°C incubator, supplemented with 5% CO₂.

2.2.1.1 Passage of immortalized cell lines

Prior to splitting a respective cell line (HEK293T or MSC80), the according medium was pre-warmed at 37°C in a water bath. In addition sterile PBS and *Trypsin/EDTA* (TE) buffer were pre-warmed at 37°C. The old medium was aspirated off a 10cm cell culture dish and cells were washed with 10ml of sterile PBS. After aspirating off PBS, 2ml of TE was added and incubated for 2min at 37°C. 10ml of the respective medium (*HEK293T medium* or *MSC80 medium*) was added to the cells and were detached from the plate surface. The

cell suspension was then transferred into a 15ml tube and centrifuged at 800rpm for 5min at 4°C. After centrifugation the supernatant was aspirated off and the cell pellet was resuspended in 5ml of appropriate medium. For the maintenance of the cell line, a 1:10 dilution of the cell suspension was plated into a new 10cm cell culture dish, containing fresh medium. For experiments the cells were further plated in 6-well or 12-well plates. The cells were maintained at 37°C and 5% CO₂ until approximately 90% of confluency was reached. HEK293T cells had to be split every 3 days and MSC80 cells required splitting once a week. MSC80 cells were kindly provided by the group of PD Dr. Burkhard Gess.

2.2.2 Transfection of cultured cells

For the transfection of cultured cells with nucleic acids (DNA or RNA) two methods were used: HEK293T cells were transfected using the modified calcium phosphate method as previously described by Konishi *et al.* (Konishi *et al.*, 2004), while MSC80 cells were transfected with the help of Lipofectamine® 2000. HEK293T cells were split 24 hours prior to the transfection, whereas MSC80 cells were split two days in advance.

2.2.2.1 Calcium phosphate transfection

In order to transfect HEK293T cells in a 6-well plate, 0.5-2µg of plasmid DNA and 0.1µg of farnesylated-GFP (= transfection marker) were diluted in 90µl sterile H₂O and were mixed with 10µl of 2.5M CaCl₂. 100µl of 2xHBSS was added and mixed while introducing air bubbles to the solution. The mixture was incubated for 5min at RT and 200µl of it was drop-wise added onto the cells. The transfected HEK293T cells were maintained for 3 days at 37°C and 5% CO₂ before lysis. The transfection efficiency was monitored, while detecting green fluorescent signals from the co-transfected GFP expression with a fluorescent microscope (Eclipse TS 100, Nikon).

2.2.2.2 Lipofectamine® 2000 transfection

For the transfection of MSC80 cells in a 10cm culture dish 6µg of plasmid DNA or shRNA together with 0.8µg of farnesylated-GFP (transfection marker and selection marker for FACS) and 0.6µg of the anti-apoptotic Bcl^{XL} plasmid were co-transfected and diluted in 1.5ml of Opti-MEM. In an additional tube 15µl of Lipofectamine® 2000 was added to 1.5ml Opti-MEM. The two solutions were incubated for 5min at RT prior to mixing. The mixture was incubated for 20min at RT and then added drop-wise to the cells. About 20h after

transfection the medium was changed twice with fresh 15ml of culture medium. The cells were kept at 37°C and 5% CO₂ for 3 days before lysis or FACS sorting. Again, transfection efficiency was monitored while using the Eclipse TS 100 fluorescent microscope from Nikon.

2.2.3 Biochemical techniques

2.2.3.1 Lysis of tissue

For further biochemical experiments mice were scarified at the desired age and tissue or organs were immediately obtained. The fresh, non-fixated tissue was placed in a reagent tube, snap frozen in liquid nitrogen and stored at -80°C. In order to lyse, the tissue was added to a 2ml dounce or homogenizer containing ice-cold *Triton®X-100 lysis buffer* + proteinase inhibitors (freshly added). By mechanical force the sample was homogenized and incubated for 30min on ice. Subsequently the lysate was centrifuged for 10min at 11000rpm and 4°C. The supernatant was collected in a new tube and the protein concentration was measured.

2.2.3.2 Lysis of cultured cells

Cultured cells were lysed for further biochemical experiments. Therefore proteinase inhibitors (aprotinin, DTT, leupeptin and pepstatin) were freshly added to the *Triton®X-100 lysis buffer* or *Co-IP buffer* if a co-immunoprecipitation was followed. Throughout the lysis, cells and lysate were kept on ice. The culture medium was aspirated off and cells were once washed with cold PBS. After aspirating off PBS, 150µl of the supplemented *Triton®X-100 lysis buffer/Co-IP buffer* was added to each well of a 6-well plate. Using a cell scraper attached cells were removed from the plate. The cell lysate was collected in a 1.5ml tube and incubated for 30min on ice. Subsequently the lysate was centrifuged at 11000rpm for 10min at 4°C. The supernatant was transferred into a new tube and the pellet discarded. For further experiments the samples were kept on ice.

2.2.3.3 Measurement of protein concentration

To measure the protein concentration either a Bradford assay or a Lowry assay was performed.

For a Bradford assay (Bradford, 1976) the Bio-Rad Bradford reagent was used in a 1:5 dilution with PBS. In order to obtain a standard curve 2, 4, 6, 8, and 10µg of bovine

serum albumin (Ip et al.) was diluted in 1ml of Bradford/PBS solution, including a blank. Further on 2 μ l of the desired sample (cell lysate or tissue lysate) was added to 1ml of Bradford/PBS solution. The protein concentration was measured with a spectrophotometer, detecting the shift in absorbance at 595nm wavelength. This reflected the binding of protein to Coomassie Brilliant Blue G-250. The BSA measurement resulted in a standard curve, which was used to calculate the protein concentration of the samples of interest.

For a Lowry assay (Lowry et al., 1951) reagents from Bio-Rad were used. 0.5 μ l of protein assay reagent S were added to 24.5 μ l of reagent A. The 25 μ l of solution mix was pipetted into a 96-well plate, further adding 5 μ l of the lysate of interest and 200 μ l of reagent B. Additionally, a standard curve was generated using 0.2, 0.5, 0.8, 1.0 and 1.5 μ g of BSA as well as a blank. Afterwards the plate was inserted into the Tecan microplate reader, in which it was incubated for 15min at 26°C. Biuret and Folin-Ciocalteu reaction allowed for the measuring of absorption at 750nm wavelength. Using the resulting standard protein curve, the concentration of the lysate of interest was determined. Excel from Microsoft Office was used for calculations.

2.2.3.4 Co-Immunoprecipitation (Co-IP)

In order to investigate the interaction of two proteins a co-immunoprecipitation assay was performed. Cells were transfected with plasmids expressing tagged proteins. Two days after the transfection, the cells were lysed with Co-IP buffer supplemented with protease inhibitors. As a control of expression 100 μ g of input from the cell lysate was mixed with *SDS sample buffer (4x)* and heated at 95°C for 5min. The sample was shortly spun down and either directly pipetted onto the SDS-PAGE or stored at -20°C until usage. For the co-immunoprecipitation 1mg of cell lysate was incubated for 2-3h with 0.6 μ g of either flag- or myc-antibody at 4°C on a rotator. In the meantime, protein A-sepharose beads, which bind to rabbit and mouse IgGs, were washed 3 times with Co-IP buffer and stored in equal amount of Co-IP buffer. Following, the sample was mixed with 15 μ l of protein A-sepharose beads and incubated for 1h at 4°C on a rotator. The beads were then washed 2-3 times with lysis buffer while incubating for 5min at 4°C and centrifuging in between for 1min at 11000rpm. The beads were then subjected to a quick wash with 500 μ l of *RIPA buffer* and centrifuged again. In the final wash step PBS was added and after centrifugation a small volume of PBS was left and mixed with 10 μ l of *SDS samples buffer (4x)*. The sample was boiled at 95°C for 5min, shortly spun down and ran on an SDS-PAGE for subsequent western-blot analysis.

2.2.3.5 SDS-PAGE and western-blot

To separate proteins according their size an SDS-PAGE method was used as described previously (Weber and Osborn, 1969). The polyacrylamide gel, consisting of an upper gel for stacking (3.9% of acrylamide) and a lower gel for separation (10% or 12% of acrylamide), were prepared in a gel casting system from Bio-Rad. The gel was prepared according to the following scheme:

Table 2.2.1 Recipe for SDS-PAGE gels of different acrylamide percentage.

% of acrylamide	Stacking gel	Separating gel	
	3.9%	10%	12%
Acrylamide/bis-acrylamide	0.65ml	2.5ml	3ml
<i>Upper buffer</i>	1.25ml	-	-
<i>Lower buffer</i>	-	1.875ml	1.875ml
H ₂ O	3.05ml	3.125ml	2.625ml
Ammonium persulfate (10%)	30µl	30µl	30µl
Tetramethylethylenediamine	3µl	3µl	3µl

The separating gel was cast first by pouring the gel mixture into the gel casting system. In addition a layer of isopropanol was added onto the separating gel. After polymerization the isopropanol was discarded and H₂O was used for washing. Afterwards the stacking gel was loaded and a 10-well comb inserted. Once the complete polyacrylamide gel was polymerized the gel was inserted into the Trans-Blot® Cell (Bio-Rad) and *running buffer* was added. The previously boiled lysates as well as a protein ladder were loaded into the wells of the gel. Proteins were separated through electrophoresis at 35mA per gel for 1h. Subsequently the proteins were transferred onto a nitrocellulose membrane, again using the Trans-Blot® Cell which contained *transfer buffer*. For the transfer 220mA were applied for 2h at 4°C. After transfer the nitrocellulose membrane was rinsed with PBST and then blocked in *blocking buffer* (4% milk in PBST) for 20min at RT on a shaker. The membrane was then rinsed with PSBT and incubated in *antibody solution* containing the desired dilution of primary antibody for 3h or over night at 4°C on a shaker. A 3 times washing step with PBST for 10min each on a shaker was followed. The secondary HRP-conjugated antibody was diluted in *blocking buffer* and was incubated for 1h at RT on a shaker. Followed by washing thrice with PBST, the membrane was incubated in enhanced chemoluminescent (ECL), a horseradish peroxidase substrate by Thermo Fischer Scientific. Quickly after, the membrane was placed into a membrane developing system by Biometra, which recorded the luminescent signal and captured it as a digital picture. Western blot pictures were edited using Adobe Photoshop and Illustrator.

2.2.4 FACS and proteasome activity assay

The proteasome activity assay was carried out according to a modified method by Kisselev and Goldberg *et al.* (Kisselev and Goldberg, 2005). The assay was performed with cell lysates of transfected MSC80 cells. MSC80 cells were transfected with shRNA and co-transfected with GFP. The cells were washed with PBS and detached from the 10cm cell plate, while using a cell scraper. Afterwards the cells were centrifuged for 5min at 200rpm. The cell pellet was resuspended in 1ml of cold PBS and sorted via FACS cytometer (FACS Calibur, BD). The sorted cells were lysed in *proteasome lysis buffer*, containing the mild detergent digitonin, 100µg BSA and 100µM of fluorogenic peptide substrate Suc-LLVY-AMC was pipetted in triplicates per sample into a 96-well plate containing *proteasome assay buffer* and was incubated for 10min at 37°C. Subsequently, 12µg of cell lysate was added per well (total volume 200µl). The fluorescent signal was measured at 355nm excitation and 460nm emission every half an hour at 0, 30, 60, 90 and 120min using the Tecan microplate reader. In-between measurements the 96-well plate was incubated at 37°C and protected from light. In order to verify the knockdown induced by shRNA, one part of the cell lysate was subjected to western-blot analysis.

2.2.5 Myelin purification

Myelin was purified from brain samples by density centrifugation using a sucrose gradient. According to Norton and Poduslo's previously described method (Norton and Poduslo, 1973a, b), (Larocca and Norton, 2007) the samples were first homogenized in 0.32M sucrose containing protease inhibitors and using the ultraturrax. At all times samples were kept on ice or at 4°C. 200µl of the homogenate was stored at -80°C for later experiments. The remaining homogenate was carefully added onto 0.85M sucrose containing protease inhibitors in an Ultra-Clear Tube (Beckman no. 344060). Afterwards the sucrose gradient was centrifuged for 30min at 75000xg in the Beckman XL-70 ultracentrifuge, using a swing out rotor (SW40Ti Beckman rotor, 24400rpm). The interphase was transferred into a new tube and washed by adding water. After centrifugation at 75000xg for 15min, an osmotic shock was induced by resuspending the pellet in H₂O, incubated for 15min and centrifuged at 12000xg for 15min (SW40Ti Beckman rotor, 9700rpm). This osmotic shock was repeated once more. Subsequently the pellet was resuspended in 0.32M sucrose. Layering the resuspended pellet over 0.85M sucrose generated a second sucrose gradient. After centrifugation for 30min at 75000xg, the interphase was collected in a new tube, H₂O was added and centrifuged at 75000xg for 15min. This final pellet consisted of

enriched myelin and was resuspended in 200µl of TBS containing protease inhibitors and was stored at -80°C. Myelin purification from brain tissue was performed by Ramona Jung (Group of PD. Dr. Hauke Werner, department of Prof. Dr. Klaus-Armin Nave, Max-Planck Institute of Experimental Medicine, Göttingen).

For myelin purification from the sciatic nerve, samples were homogenized in 0.29M sucrose containing protease inhibitors using an ultraturrax. For further experiments 100µl of lysate were stored at -80°C. Similar to the sucrose gradient described before, the lysate was added onto 0.85M sucrose in an Ultra-Clear Tube (Beckman no. 344062). The samples were centrifuged as well for 30min at 75000xg (26900rpm) but in a TH660 Beckman rotor. Again the interphase was washed with water as described before and only one osmotic shock was induced. The pellet was resuspended in 100µl of TBS containing protease inhibitors and stored at -80°C. Myelin purification from sciatic nerves was conducted together with Katja Lüders (Group of PD. Dr. Hauke Werner, department of Prof. Dr. Klaus-Armin Nave, Max-Planck Institute of Experimental Medicine, Göttingen).

2.2.5.1 Silver staining of SDS-PAGE

In order to detect robust changes in protein abundance of purified myelin within and between genotypes, samples were subjected to SDS-PAGE analyses. 12% gels were prepared as previously described and 0.5µg of purified CNS myelin or 5µg of PNS myelin was loaded onto the gels and ran for 1 hour at 200V. The gels were incubated in 40% ethanol + 10% acetic acid over night at 4°C. On the next day a silver impregnation was performed according to the Pierce® Silver staining kit. The gels were incubated twice 5min in 10% ethanol and twice washed for 5min in water. Next, the gels were incubated in sensitizer solution for 1min, washed twice for 1min in H₂O and then incubated for 30min in working solution. After two quick washes in water for 20sec, the developer solution was immediately added and incubated until bands appeared. The solution was replaced with stop solution (5% acetic acid), briefly washed, replaced with new stop solution and incubated for 10min. Finally the gels were washed with H₂O and stored at 4°C.

2.2.5.2 Quantitative Mass spectrometry

The quantitative mass spectrometry was conducted by Dr. Olaf Jahn from the proteomics department of the Max-Planck institute for Experimental Medicine. Here 10µg of purified myelin was lysed and processed according to a filter-aided sample preparation (FASP) protocol ((Wisniewski et al., 2009) and further modified as described by Distler et al

(Distler et al., 2014; Distler et al., 2016). The samples were then subjected to LC-MS analysis, in which a nanoscale reversed-phase UPLC separation of tryptic peptides was performed. Therefore, a nanoAcquity UPLC system was used, equipped with a Symmetry C18 5 μ m, 180 μ m \times 20mm trap column and a HSS T3 C18 1.8 μ m, 75 μ m \times 250mm analytical column maintained at 45°C. Injected peptides were trapped for 4min at a flow rate of 8 μ l/min 0.1% trifluoroacetic acid and then separated over 120min at a flow rate of 300nl/min. The LC-MS data were analyzed while using Waters ProteinLynx Global Server version (Li et al., 2009). To identify proteins, a custom database was used and additionally the false discovery rate (FDR) that was set to 1% threshold was determined. The freely available software ISOQuant (<http://www.isoquant.net>) was used for post-identification analysis and the stringency of identified protein was increased by considering only peptides with a minimum length of six amino acids, which were identified with scores above or equal to 5.5 in at least two runs (Distler et al., 2014; Distler et al., 2016; Kuharev et al., 2015). The final analysis was done using Microsoft Excel and diagrams were prepared with GraphPad Prism.

2.2.6 Transgenic mouse line

All mice used for this study were kept and bred in the mouse facility of the Max-Planck-Institute for Experimental Medicine in Göttingen or the mouse facility of the RWTH university hospital in Aachen. Experiments were performed according to the guidelines for German animal welfare and were approved by the “Verbraucherschutz und Lebensmittelsicherheit” of Lower Saxony, Germany (33.11.42502-04-11/0632). Mice were scarified either by cervical dislocation or by perfusion under anesthesia.

2.2.6.1 Generation of conditional FBXO7 mouse line

Homozygous conditional *Fbxo7*^{fl/fl} mice (Vingill et al., 2016), in which exon 4 was flanked by loxP sites, were either mated with heterozygous *Cnp1*^{Cre/+} mice (Lappe-Siefke et al., 2003) or with heterozygous Tamoxifen-inducible *Plp1*^{CreERT2/+} mice (Leone et al., 2003). In these conditional knockout mice FBXO7 was deleted from myelinating cells.

Cnp- and well as *Plp*-driver line were provided by Prof. Dr. Klaus-Armin Nave (Neurogenetics department, Max-Planck Institute of Experimental Medicine, Göttingen).

2.2.6.2 Tamoxifen induced knock down

Plp1^{CreERT2/+} mice were bred with *Fbxo7*^{fl/fl} mice to generate conditional *Plp1*^{CreERT2/+};*Fbxo7*^{fl/fl} mice. In these inducible mice, Cre recombinase expression will only be activated upon Tamoxifen injection. Hence, 100µl of 20mg/ml Tamoxifen dissolved in corn oil was intraperitoneally injected in mice for 5 consecutive days. The total amount of injected Tamoxifen was 10mg. Injection of mice and thereby the induction of the conditional knock out of the *Fbxo7* gene was performed at two months of age, when myelination was completed. Control mice lacking the *Plp1*-CreERT2 insertion were also injected with the same amount of Tamoxifen.

2.2.6.3 Isolation of genomic DNA

Tail biopsies from mice were used to isolate genomic DNA for subsequent genotyping analysis. The tissue was lysed in 200µl of *tail lysis buffer* with freshly added 3µg/ml Proteinase K and 0.2M NaCl for minimum 2h at 55°C. Once the tail was completely lysed, the sample was centrifuged for 10min at 14000rpm and RT. The supernatant was transferred into a new tube and mixed with 500µl of 100% ethanol and again centrifuged for 10min at 14000rpm and RT. The supernatant was discarded and the pellet of precipitated DNA was washed with 300µl of 70% ethanol. Again the sample was centrifuged for 3min at 14000rpm and RT. After aspirating off the ethanol, the precipitated DNA pellet was air-dried at RT for 15min and then dissolved in 200µl of sterile H₂O. The isolated genomic DNA was then used for genotyping and stored at -20°C.

2.2.6.4 Genotyping

For each sample 3 PCR reactions were set up. The PCR reaction was performed according to Kary Mullis first described and over the years modified protocol (Saiki et al., 1985). Using the Cre, wild type *Fbxo7* as well as the floxed *Fbxo7* primer pairs, the genotype of the conditional knockout mice was determined. For genotyping the GoTaq® DNA polymerase system was used and PCR samples were run on a 1% agarose gel (in *2xTAE buffer*) containing 1:100000 of GelRed for visualization. Pictures were obtained with the UV transilluminator system from Biometra and edited using ImageJ, as well as Adobe Illustrator.

The PCR reaction was pipette the following:

Table 2.2.2 Recipe for PCR reaction.

PCR reaction	
17µl	H ₂ O
5µl	5x GoTaq® buffer
0.4µl	dNTPs (2.5mM)
1µl	forward primer (10pmol/µl)
1µl	reverse primer (10pmol/µl)
0.1µl	GoTaq® DNA polymerase
0.5µl	genomic DNA

The PCR reaction was run according to the following program:

Table 2.2.3 Set up of PCR program for genotyping.

<i>Fbxo7</i> PCR genotyping program			
Denaturation	95°C	3min	
Denaturation	95°C	30sec	
Annealing	55°C / 53°C*	45sec / 30sec*	30 / 28* cycles
Elongation	72°C	45sec	
Final elongation	72°C	5min	
Final hold	16°C	Pause	

* = specifically for the wild-type *Fbxo7* primer pair

2.2.6.5 RNA isolation

Total RNA was isolated for further analysis of mRNA expression levels. Prior to RNA isolation, surface areas were thoroughly cleaned with ethanol and only filter pipette tips were used. Throughout isolation the samples were always kept on ice. 1mL of Trizol® Reagent was added to mouse tissue and homogenized in a 2ml glass dounce. 200µl (1/5 of Trizol® Reagent volume) of chloroform was added and vortexed for 15sec. Next, the sample was incubated for 15min on ice and then centrifuged for 15min at 14000rpm and 4°C. The topmost layer after centrifugation containing isolated RNA was transferred into a new tube and mixed with equal volume of isopropanol followed by vortexing. The sample was incubated over night at -80°C and on the consecutive day was centrifuged for 15min at 14000rpm and 4°C. The supernatant was discarded and the RNA pellet was washed with 100% ethanol, centrifuged and washed with 70% of ethanol. Next, ethanol was removed, the pellet air-dried and dissolved in 50µl of 10mM Tris/ 1mM EDTA, pH 7.5. The concentration of RNA was measured, while using a NanoQuant Tecan plate reader.

2.2.6.6 cDNA synthesis

The previously isolated RNA was further used for cDNA synthesis. Therefore the SuperScript® III First strand synthesis kit was used according to the following scheme:

Table 2.2.4 Protocol for cDNA synthesis I.

cDNA synthesis I	
3µg	isolated RNA
1µl	50µM Oligo dT
1µl	10mM dNTP
10µl	ddH ₂ O (fill up to final volume)

The mixture was incubated for 5min at 65°C and 1min on ice. In a second step, the reverse transcriptase mixture was prepared:

Table 2.2.5 Procedure for cDNA synthesis II.

cDNA synthesis II	
2µl	10x reverse transcriptase buffer
4µl	25mM MgCl ₂
2µl	0.1M DTT
1µl	RNAse OUT
1µl	SuperScript reverse transcriptase
10µl	ddH ₂ O (fill up to final volume)

Both mixtures were combined and incubated for 50min at 50°C. The reaction was stopped at 85°C for 5min and followed by an incubation on ice and the addition of 1µl of RNAseH. The samples were incubated for 20min at 37°C and stored at -20°C until usage for RT-PCR.

2.2.6.7 Quantitative real-time (RT) PCR

To amplify target sequences and quantify the amount of template at the same time, a real-time PCR was conducted. Therefore the Power SYBR Green system was used and prepared as described in table 2.2.6. The primers used are listed in table 2.1.6. The quantitative RT-PCR was monitored via a PCR thermo cycler. For analysis of the obtained data, Microsoft Excel was used applying the Livak - delta delta C_T method for quantification. *β-Actin* was used as a reference gene and the average of all control samples was also used as a reference.

First the C_T value of the target gene was normalized to the C_T value of the reference gene:

$$\Delta C_T(\text{control sample}) = C_T(\text{ctrl sample, target gene}) - C_T(\text{ctrl sample, ref gene})$$

$$\Delta C_T(\text{test sample}) = C_T(\text{test sample, target gene}) - C_T(\text{test sample, ref gene})$$

Then the ΔC_T of the test sample was normalized to the ΔC_T of the control sample:

$$\Delta \Delta C_T = \Delta C_T(\text{test sample}) - \Delta C_T(\text{control sample})$$

Finally the fold difference in expression was calculated:

$$\text{normalized expression ratio} = 2^{-\Delta \Delta C_T}$$

Further on GraphPad Prism was used for generating graphs and statistical analysis.

Table 2.2.6 Protocol for RT-PCR.

RT-PCR	
5 μ l	2x SYBR Green
0.1 μ l	1pmol forward primer
0.1 μ l	1pmol reverse primer
0.14 μ l	cDNA
10 μ l	ddH ₂ O (fill up to final volume)

2.2.6.8 Electrophysiological measurement

In order to investigate the propagation of action potentials along nerve fibers on anesthetized animals, electrophysiological recordings were conducted. The analysis was performed by stimulation of the nervus ischiadicus and the nervus tibialis posterior at the proximal site of the foramen ischiadicum. At the distal area of the knee, a needle electrode was injected and the nerves were stimulated for 0.1ms. By doing so, the delay between initiating an action potential and the response of the muscles was measured. The nerve conductance velocity (NCV) was calculated, by measuring the time between proximal stimulation and distal recording of a given distance. Another measurement is the compound muscle action potential (CMAP), which was calculated from the amplitude of the highest and lowest value. Further on the distal motor latency (DML) was measured from the delay between initiating a stimulus and the evoked potential. Data retrieved were analyzed using Microsoft Excel and GraphPad Prism. This experiment was performed by Dr. Robert Fledrich (Group of Prof. Dr. Michael W. Sereda, Max-Planck Institute of Experimental Medicine, Göttingen).

2.2.7 Histological analysis

2.2.7.1 Transcardial perfusion and fixation

Mice were anesthetized by intraperitoneal injection of 10% Ketamine (CP Pharma) and 5% Xylazine (Medistar Arzneimittelvertrieb GmbH), using 100µl per 10g of weight. Reflexes were tested at all four paws. Once all signs of reflexes were suppressed, the thorax was opened by a long incision along the diaphragm and sternum, exposing the heart. A small G21 butterfly canula, which was connected to a peristaltic pump (rate set to 12rpm), was inserted into the left ventricle of the heart and simultaneously the right atrium was cut. First 10ml sterile PBS was pumped into the vascular system to clear blood from body. Subsequently, the tissue was fixed with 10ml of 4% PFA for perfusion or with *Karlsson and Schultz buffer*, if the tissue was subjected to electron microscopic analysis. Organs were dissected and incubated in 4% PFA for tissue over night at 4°C and then further post-fixed, depending on the experimental procedure.

2.2.7.2 Immunohistochemistry on cryo-sections

The previously dissected and PFA-fixed sample was incubated in 30% sucrose/PBS over night at 4°C, embedded in OCT (Tissue Tek, Sakura, Torrance, USA) and stored at -80°C. For sectioning, the samples were cut into 10µm thin sagittal or coronal sections, as per experimental design, using a cryostat (CM3050 S, Leica). The sections were either mounted onto glass slides or stored in PBS+0.02% of NaN₃ as free-floating sections at 4°C. For fluorescent staining, cryo-sections were washed twice 5min with PBST on a shaker at RT, permeabilized with 0.5% Triton®X-100 in PBS for 30min and then blocked for 1h in blocking solution. After a 5min wash in PBST the samples were incubated over night at 4°C in *antibody solution* containing the respective dilution of primary antibody. Next, the samples were washed thrice for 10min in PBST and further incubated for 1h at RT in a secondary antibody conjugated to a fluorescent dye, diluted in *antibody solution* and nuclei staining dye DAPI (1:8000). The samples were washed three times for 5min in PBST at RT. In case of free-floating sections, the samples were mounted on a glass slide and shortly dried at 37°C for 15min. Cryo-sections were mounted using *Mowiol mounting medium* and stored at 4°C. Pictures were taken using the fluorescent microscope BX51 from Olympus and for quantification ImageJ was used. In case of a double staining, non-specific background staining was removed by using the SpectralUnmixing plugin generated by Joachim Walter. Pictures were further stitched by applying the plugin from Preibisch *et al.* (Preibisch *et al.*, 2009) and quantified using a customized macro written by Dr. Miso Mitkovski. This customized macro quantified the area that is stained in pixel, as

well as the total area of the sample, in order to calculate the percentage of area stained. Statistical analysis and graphs were performed using GraphPad Prism.

2.2.7.3 Immunohistochemistry on paraffin-sections

Post-fixation of mice tissue that was destined for paraffin embedding, was incubated over night in 4% PFA for tissue at 4°C after perfusion. The samples were then embedded in paraffin using an automated embedding machine (HMP110, MICROM) and following the protocol was applied:

Reagent	Duration
50% ethanol	1h
70% ethanol	2x 2h
96% ethanol	2x 1h
100% ethanol	2x 1h
isopropanol	1h
xylene	2x 2h
paraffin	2x 2h

The tissue embedded in paraffin, was cut into 5µm sagittal sections using a microtome (HM 430, Thermo Fischer Scientific), mounted on glass slides and air-dried at RT. Paraffin-sections were stained using the LSAB₂ detection system. Here, sections were de-paraffinized by heating for 10min at 60°C, followed by 2x 10min incubation in xylene and 10min in a xylene/isopropanol mixture (1:2). The samples were further incubated in 100%, 90%, 70% and finally 50% of ethanol for 5min, respectively. Lastly, tissue was hydrated in ddH₂O for 5min. For DAB staining, the sections were incubated in *citrate buffer* for 5min at RT and further boiled in *citrate buffer* for 10min in a microwave oven to un-mask the antigen and permeabilize the tissue. The samples were given 20min at RT to cool down, followed by incubation in *Tris buffer + 2% milk* for 5min. Afterwards the slides were placed into a Shandon cover plate by Thermo Fischer Scientific, allowing an even distribution of solution on the slide. Since the secondary antibody was conjugated with HRP (horseradish peroxidase), the slides were incubated for 5min with 3% H₂O₂ to inactivate endogenous peroxidase. The samples were rinsed with *Tris-buffer + milk* and then blocked in 100µl *blocking buffer* for 10min at RT. Subsequently, the samples were incubated in primary antibody diluted in BSA/PBS at 4°C over night. The next day, the slides were rinsed with *Tris buffer + milk* and incubated for 10min at RT in 100µl of a bridging, biotinylated antibody of the LSAB₂ kit (Dako). Again, the slides were washed with *Tris buffer + milk* and then incubated in 100µl of horseradish peroxidase streptavidin

complex for 10min at RT (LSAB₂ kit). The slides were washed with Tris buffer, disassembled from the Shandon cover plate and placed in Tris buffer. Diaminobenzidine (Veitenhansl et al.), the substrate of HRP, was applied onto the slides using a DAB kit and incubated for 5-10min. The sections were washed twice with H₂O for each 5min and then counter-stained in hemalaun for 30seconds. The sections were washed with distilled H₂O, shortly incubated in HCL/ethanol and again rinsed with H₂O. After 5min incubation in Scott's solution and a wash step in water, the sections were subjected to increasing ethanol dehydration in 50%, 70%, 90% and 100% ethanol for each 5min at RT. Subsequently, the sections were immersed in isopropanol/xylene for 10min and twice for 10min in xylene. Finally, a coverslip was mounted onto the slides using Eukitt mounting medium. The light microscope Axiophot from Zeiss was used for imaging. The resulting pictures were then further analyzed with ImageJ. Graphs and statistical analyses were done using GraphPad Prism.

2.2.7.4 Tunnel assays

Staining of apoptotic cells was performed by using the DeadEnd™ Colorimetric TUNEL System kit. Once the paraffin-embedded 5µm tissue was deparaffinized as previously described, a TUNEL (TdT-mediated dUTP Nick-End Labeling) assay was performed according to the instruction from the kit. Terminal deoxynucleotidyl transferase (TdT) mediates the binding of biotinylated nucleotids at the 3'-OH of fragmented DNA sites, which will be detected by streptavidin-HRP. Finally, the peroxidase substrate DAB binds to the complex and precipitates as brown staining. The sections were mounted with coverslips using Aqua-Poly/Mount mounting medium. Quantification and statistical analyses were conducted as described in "immunohistochemistry on paraffin-sections".

2.2.7.5 Gallyas silver impregnation

Myelin fibers were stained using the protocol developed by Gallyas (Gallyas, 1979), in which colloidal silver particles bind to myelin. 5µm sections of tissue embedded in paraffin were de-paraffinized as described before and incubated in a 2:1 mixture of pyridine and acetic anhydride for 30min at RT, preventing staining of any other tissue but myelin. The samples were rinsed three times with water for 10min and then incubated in warm *incubating solution* for 10min at RT. Afterwards the slides were washed three times with 0.5% acetic acid for 5min and incubated in *developing solution* for 3-15min until the desired intensity of staining was reached. The reaction was stopped by applying 1% acetic acid three times for 5min. The samples were washed twice for 3min with H₂O and incubated in 2% sodium thiosulfate solution for 5min, stabilizing the silver staining. After

rinsing twice with water for 5min, the samples were dehydrated using an ethanol gradient (50%, 70%, 90% and 100% of ethanol for 5min each) and incubated for 10min in isopropanol/xylene (1:1) and twice in xylene. The slides were mounted using Eukitt mounting medium. Quantification and statistical analyses were conducted as described in "immunohistochemistry on paraffin-sections".

2.2.8 Electron microscopic analysis

2.2.8.1 Tissue preparation and epon embedding

Mouse tissues were dissected from animals, which were perfused with *Karlsson and Schultz buffer* and post-fixed in Karlsson-Schulz fixative. The tissue was rinsed once in 0.1M PBS and embedded in epon according to a modified method described by Luft *et al.* (Luft, 1961). Using an automated embedding machine (EMTP, Leica), the following protocol was applied:

Solution	Duration	Temperature
phosphate buffer	3 x 10min	4°C
2% OsO ₄	4h	4°C
ddH ₂ O	3 x 10min	4°C
30% ethanol	20min	4°C
50% ethanol	20min	4°C
70% ethanol	20min	4°C
90% ethanol	20min	4°C
100% ethanol	4 x 10min	4°C
propylenoxid	3x 10min	RT
propylenoxid/ epon (2:1)	2h	RT
propylenoxid/ epon (1:1)	2h	RT
propylenoxid/ epon (1:2)	4h	RT
epon	4h	RT

The tissue was embedded further in an epon-filled mold and kept over night at 60°C for polymerization.

2.2.8.2 Staining of semi-thin sections

The embedded samples were sectioned using a microtome (Ultracut S, Leica), while cutting with a diamond knife (Diatome Ultra 45°) semi-thin section of 500nm thickness. The samples were placed onto a glass slide and dried on a 60°C hot plate. For staining of semi-thin sections, *methylene blue* and *Azure II staining solution* were freshly mixed 1:1 and applied onto the sections (Richardson et al., 1960). The sections were incubated for 1min on a 60°C hot plate, thoroughly rinsed with ddH₂O, dried and mounted with Eukitt. Semi-thin sections were observed under a light microscope, in order to judge the position within a sample.

2.2.8.3 Contrasting of ultra-thin sections

Ultra-thin sections were cut similarly to semi-thin section, but of 50nm thickness. The samples were placed onto formvar-polyvinyl coated copper grids (2mm-1mm, AGRA scientific) and dried at RT. For contrasting, the grids were placed upside-down onto drops of uranyl acetate for 30min at RT and covered from light. Then, the grids were washed three times with ddH₂O for 1min, incubated for 6min onto drops of Reynolds lead citrate (Reynolds, 1963) and finally washed four times 1min with ddH₂O. The grids were dried by placing them on filter paper. Electron micrographs of the ultra-thin sections were obtained by using the electron microscope EM900 from Zeiss combined with a wide-angle dual speed 2K-CCD camera from TRS. Afterwards, images were analyzed by measuring the g-ratio and by assessing distinctive histological features. ImageJ, Microsoft Excel and GraphPad Prism were used for further analyses.

For g-ratio measurement, 10 randomly chosen images of a section (3000x magnification) were taken. Of those, 100 axons per section were quantified. By this measurement the thickness of myelinated fibers was calculated. The outer circumference of the myelin sheath, as well as the inner circumference was calculated with ImageJ. The ratio of inner circumference divided by the circumference of the outer myelin sheath equals the g-ratio. A baseline g-ratio value is approximately 0.77 in the central nervous system and 0.6 in the peripheral nervous system. Values higher indicate a hypomyelination, whereas smaller values indicate hypermyelination.

Cnp1^{Cre/+};Fbxo7^{fl/fl} mice: embedding and sectioning of samples, as well as obtaining electron microscopic pictures were done with the help of Torben Ruhwedel and Boguscha Sadowski (EM facility, group of Dr. Wiebke Möbius, department of Prof. Dr. Klaus-Armin Nave, Max-Planck Institute of Experimental Medicine, Göttingen). Siv Vingill measured the g-ratio of optic nerve samples.

Pip1^{CreERT2/+}; *Fbxo7*^{fl/fl} mice: preparation of samples and acquisition of electron microscopic images were obtained with the support of Claudia Krude, Hannelore Mader and Dr. Istvan Katona (EM facility, department of Prof. Dr. Joachim Weis, RWTH University, Aachen). Quantifications of the g-ratio of sciatic nerve samples were done together with Yuhao Huang.

2.2.9 Mouse behavioral analyses

Transgenic mice underwent behavioral analyses at different time points to assess motor and sensory phenotypes. All tests were conducted under standardized conditions, at fixed light intensity of 90 lux and protected from disturbance. Male mice were used throughout the study for behavior analyses. Prior to each session, mice were allowed to acclimate for 30min in the test room. Afterwards the weight of the mice was determined and the behavioral tests were performed in a distinct order: first elevated plus maze for assessing anxiety, then open field test for ambulation and exploratory behavior, followed by tail suspension test, inverted grid, pole test, wire hang, balance beam and Rotarod for motor endurance and coordination. For sensory assessment the hot plate test was performed. In-between each mouse to be tested, the equipment was cleaned with water and 70% ethanol. The animals were monitored using the software Viewer from Bioobserve. Further on obtained data were analyzed using Microsoft Excel and GraphPad Prism.

2.2.9.1 Elevated plus maze

In order to evaluate the anxiety of mice, an elevated plus maze test was conducted according to published protocol (Pellow et al., 1985). The apparatus is comprised of 4 arms, all measuring 5x30cm. Two arms are open, whereas a 15cm high wall encloses the other two arms. The maze is elevated 40cm from the ground. Mice were placed in the center of the plus maze, facing an open arm, and both activity and exploratory behavior were recorded for 5min with the Viewer software. The time spent in open and closed arms was analyzed, since intensive time spent in an open arm indicates reduced anxiety.

2.2.9.2 Open field

General locomotion and exploratory behavior was measured in an open field test, as previously demonstrated (Hall, 1932). The round arena had a diameter of 60cm and was surrounded by a 20cm high wall. Further on the open field was subdivided into 3 zones, the central circle of 20cm in diameter, an intermediate zone of 40cm in diameter and the

peripheral zone of 60cm in diameter. The mice were placed in the center and movement was monitored for 7min with the Viewer animal tracking system. The travelled distance, velocity and time spent in different zones were analysed.

2.2.9.3 Tail suspension test

To assess signs of neurological deficits and neurodegenerative disease progression, a modified form of the tail suspension test described by Steru *et al.* (Steru *et al.*, 1985) was performed. Mice were lifted by their tail and hold closely over their cage for 10 seconds. The position of the hind limbs were scored from 0-3, with 0 representing normal, splayed hind limbs and 3 indicating strong claspings of the hind paws. An average out of three repetitive measurements was considered as final score. In-between repeated measurements a 30sec pause was given.

2.2.9.4 Kyphosis

The determination of kyphosis was conducted as previously described (Guyenet *et al.*, 2010). Mice were observed while walking and the curvature of the spin was scored from 0-3. A score of 0 implied no signs of kyphosis, were as 1 indicated an arched spin while sitting, but not while walking. A score of 2 was given when the back was curved while sitting and mildly during movement and a score of 3 marked a severe kyphosis during sitting and walking.

2.2.9.5 Inverted grid

Muscle strength was assessed by the inverted grid test. Therefore mice were placed onto the grid of their home cage and the grid was inverted, holding it above the cage. The time mice could hold on to the grid, while being upside down, was measured with a cut-off time at 60sec. Three repeated measurements were done with a break of 1min in-between and the average of all measurements were calculated (Kondziela, 1964).

2.2.9.6 Pole test

The pole test has been previously described as an assessment for basal ganglia related motor function (Matsuura *et al.*, 1997), (Ogawa *et al.*, 1985). Mice were placed onto a vertical 50cm long pole facing upwards and had to turn in order to walk down the pole. The pole was placed in the home cage of the mice and the time needed to reach the bottom of the pole was taken. The animals were trained 2 days before testing, where

three consecutive measurements were done, with an interval of 1min. Finally, the average of all measurements were calculated.

2.2.9.7 Wire hang

Another test for muscle strength is the wire hang test, as previously described (Aartsma-Rus and van Putten, 2014). The wire apparatus consists of an 80cm long steel wire, which was affixed at 30cm to poles. The ground was covered with soft tissue and the mice were suspended in the middle of the wire with their front paws. Then the time was measured that the mice needed to reach one of the poles. Three repeats were performed with an interval of 1min and the average time was calculated.

2.2.9.8 Balance beam

For testing balance and coordination, a balance beam test was conducted as previously described (Luong et al., 2011). The apparatus consists of either a 6mm or a 12mm wide and 80cm long beam, which is attached to a black box (15x15x15cm). The beam is elevated 50cm from the ground, with a safety net placed underneath. Prior to testing the mice, the animals were acclimated for 1min inside the black box containing food pellets. Afterwards, the mice were placed on the opposite end of the beam and time, as well as numbers of slips were counted until the black box was reached. The training was performed on two consecutive days and on the third days the animals were tested. For each beam, three repetitions were done, with a 1min break in-between repetitions and 10min resting time in-between the beams. The average of time required to cross the beam, as well as numbers of slips was calculated.

2.2.9.9 Rota-Rod

While subjecting the mice to the Rotarod test, the motor coordination and endurance was tested. The program of the Rotarod was set for an increase of acceleration every 5 seconds starting with 4rpm and reaching 40rpm after 3min. The average time spent on the moving rod was measured and each mouse was tested three times, with a 10min break in-between. The cut-off time was set for 5min. Furthermore a learning curve was established by performing tests at 0h, 3h and 24h.

2.2.9.10 Hot plate

To assess sensory deficits, especially pain, a hot plate test was conducted. (Eddy and Leimbach, 1953) Mice were placed in a 1000ml round glass beaker on a 55°C metal plate. The time was stopped when mice showed any sign of irritation due to the heat, indicated in paws licking or jumping. The animals were immediately removed from the plate once showing signs of irritation. Further on a cut-off time of 30sec was set. Three repeated measurements were taken with a 10min break in-between. The average time was calculated.

Behavioral analyses of the *Cnp1^{Cre/+};Fbxo7^{fl/fl}* mice was performed by Siv Vingill.

2.2.10 Statistical analysis

All data obtained were further analyzed using Microsoft Excel. For statistical analysis GraphPad Prism was used. Normally distributed data of two groups were compared using the student T-test. For the analysis of data from more than two groups a one-way ANOVA were used. In case of two different independent variables, the influence on the depended variable was calculated by using a two-way ANOVA. Statistical differences were considered as significant if $P < 0.05$ (* $P < 0.05$, ** $P < 0.01$, *** $P < 0.001$). All data are displayed as standard error of the mean (s.e.m.), unless otherwise stated.

Fluorescent images were analyzed, using a customized macro designed by Dr. Miso Mitkovski (Light microscopy facility, Max-Planck Institute of Experimental Medicine, Göttingen).

3. Results

3.1 Systemic characterization of *Cnp1*^{Cre/+};*Fbxo7*^{fl/fl} mice

The proper functioning of the UPS is essential to CNS and PNS integrity. FBXO7, which is part of the UPS, was shown to have crucial functions within neurons, since analyses of mice with conditional deletions of *Fbxo7* display severe motor deficits. While recent studies focused on the importance of FBXO7 in neurons, its impact on myelinating cells remains unknown. Owing to FBXO7's strong expression in myelinating cells and the intimate interaction of myelinating cells and neurons, I investigated if FBXO7 is equally essential for myelinating cells and the axonal integrity in the *Cnp1*^{Cre/+};*Fbxo7*^{fl/fl} mouse line. Investigating the role of the UPS in myelinating cells, will elucidate its importance for the axon-glia interaction and opens a new perspective on the underlying and contributing mechanisms in neurodegenerative diseases.

3.1.1 Deletion of *Fbxo7* in myelinating cells by generating a conventional *Cnp1*^{Cre/+};*Fbxo7*^{fl/fl} mouse line

FBXO7 is ubiquitously expressed in various tissues of mice and men (Ilyin et al., 2000; Winston et al., 1999). The widespread expression of FBXO7 in the murine brain was shown by my colleague Dr. David Brockelt, who performed a β -galactosidase staining of brain sections from conventional *Fbxo7* knockout mice, in which the lacZ expression cassette was under the control of the endogenous *Fbxo7* promoter (Brockelt, 2015). The staining revealed that FBXO7 is predominantly expressed in the cortex, hippocampus and substantia nigra, as well as in the white matter of the cerebellum and corpus callosum. While my colleagues investigated the importance of FBXO7 in neurons, I investigated its function in myelinating cells. In collaboration with the department of Prof. Dr. Klaus-Armin Nave, we generated the *Cnp1*^{Cre/+};*Fbxo7*^{fl/fl} conditional knockout (cKO) mouse, by breeding the *Fbxo7*^{fl/fl} line (Vingill et al., 2016) with the *Cnp1*^{Cre/+} driver line (Lappe-Siefke et al., 2003) (**Figure 3.1.1a**). *Cnp1* encodes for CNPase (2',3'-cyclic-nucleotide 3'-phosphodiesterase), a myelin-associated enzyme, which is present in myelin of the central- (CNS) and peripheral nervous system (PNS) (Sprinkle et al., 1985). The *Cnp1*-*Cre* mice were kept heterozygous, whereas the *Fbxo7* floxed line was bred to homozygosity. Throughout this study *Fbxo7*^{fl/fl} and *Cnp1*^{Cre/+} mice were used as controls for the *Cnp1*^{Cre/+};*Fbxo7*^{fl/fl} knockout mice. The correct breeding was confirmed and monitored, while genotyping of the Cre, floxed *Fbxo7* and wild type *Fbxo7* allele (**Figure**

3.1 Systemic characterization of *Cnp1*^{Cre/+};*Fbxo7*^{fl/fl} mice

3.1.1b). Further on, the deletion of *Fbxo7* from myelinating cells was validated at the mRNA level. Therefore, a RT-PCR was performed on cerebellum samples from 2-month-old *Fbxo7*^{fl/fl} and *Cnp1*^{Cre/+};*Fbxo7*^{fl/fl} mice. The *Fbxo7* mRNA was reduced by about 73% in the cKO samples as compared to control confirming the knockout of *Fbxo7* in myelinating cells (**Figure 3.1.1c**). These findings confirm the deletion of *Fbxo7* from myelinating cells in the *Cnp1*^{Cre/+};*Fbxo7*^{fl/fl} mouse line.

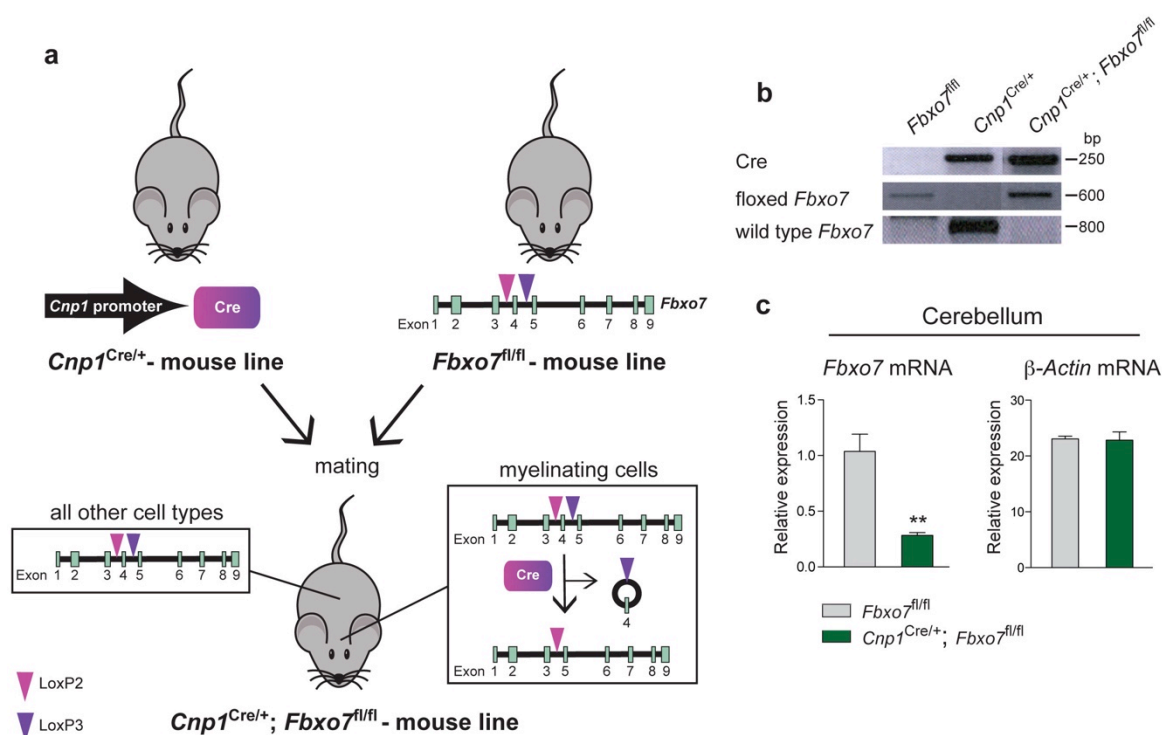


Figure 3.1.1 Validation of *Cnp1*^{Cre/+};*Fbxo7*^{fl/fl} knockout mouse line.

(a) Schematic representation of *Cnp1*^{Cre/+};*Fbxo7*^{fl/fl} breeding including schematic of floxed *Fbxo7* gene. Modified from Erdmann *et al.* (Erdmann *et al.*, 2008). *Fbxo7*^{fl/fl} mice were generated by Nicola Schwedhelm-Domeyer. (b) Genotyping PCR of *Fbxo7*^{fl/fl}, *Cnp1*^{Cre/+} and *Cnp1*^{Cre/+};*Fbxo7*^{fl/fl} mice using primers for Cre, floxed allele and wild type *Fbxo7*. (c) RT-PCR of 2-month-old *Fbxo7*^{fl/fl} and *Cnp1*^{Cre/+};*Fbxo7*^{fl/fl} mice from cerebellar cDNA. Primers for *Fbxo7* and β -Actin (reference) were used. n = 4 for both groups (unpaired t-test, **P < 0.01, mean \pm s.e.m.).

3.1.2 *Cnp1*^{Cre/+};*Fbxo7*^{fl/fl} mice display a distinct phenotype

At 6 weeks of age, the phenotype of *Cnp1*^{Cre/+};*Fbxo7*^{fl/fl} mice was clearly distinguishable from control mice. When examining *Cnp1*^{Cre/+};*Fbxo7*^{fl/fl} and control mice at 3 months of age, I found cKO mice to be smaller in size and harboring a prominent kyphosis (**Figure 3.1.2a**). Moreover, *Cnp1*^{Cre/+};*Fbxo7*^{fl/fl} mice died very early, already around 4 months of age. Therefore analyses in this study were performed latest at 3 months of age. To

3.1 Systemic characterization of $Cnp1^{Cre/+};Fbxo7^{fl/fl}$ mice

determine the cause of the premature death, I examined the mice for pathological changes. I found that the cKO mice displayed a severe muscle atrophy of the musculoskeletal system (**Figure 3.1.2b**), as well as atrophic lungs (**Figure 3.1.2c**). Further on the animals showed a severe paresis of the hind limbs and a loss of tail tone. These preliminary observations indicate that FBXO7 is essential in myelinating cells.

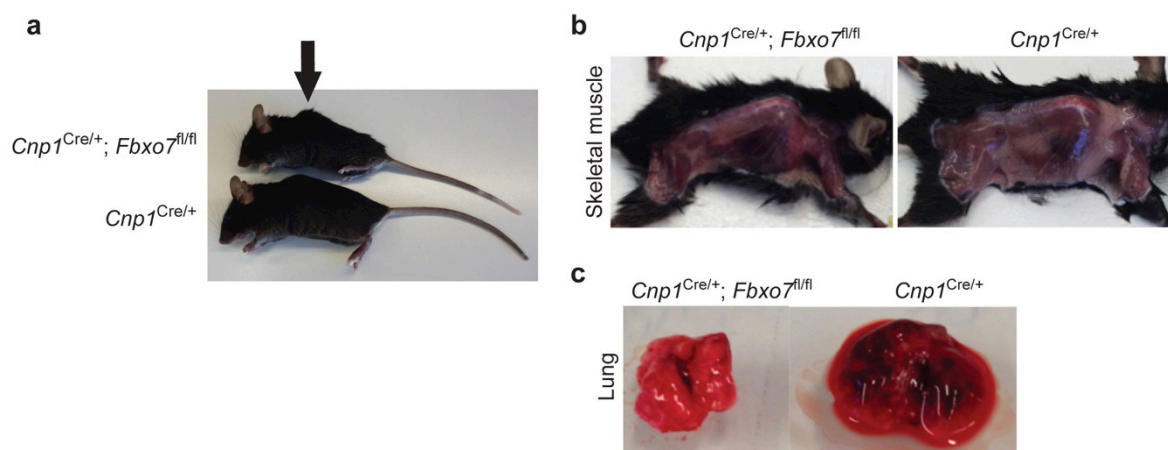


Figure 3.1.2 $Cnp1^{Cre/+};Fbxo7^{fl/fl}$ mice display kyphosis, muscle and lung atrophy.

(a)-(c) Representative images of a 3-month-old $Cnp1^{Cre/+};Fbxo7^{fl/fl}$ and an age-matched $Cnp1^{Cre/+}$ mouse show (a) kyphosis, indicated by arrow, (b) atrophy of skeletal muscle and (c) atrophic lungs.

3.1.3 $Cnp1^{Cre/+};Fbxo7^{fl/fl}$ mice show paresis of the hind limbs caused by muscle weakness

To examine the motor performance of $Cnp1^{Cre/+};Fbxo7^{fl/fl}$ mice, my colleague Dr. Siv Vingill performed a battery of behavioral tests. 6 week-old $Cnp1^{Cre/+};Fbxo7^{fl/fl}$ mice were tested together with $Cnp1^{Cre/+}$ and $Fbxo7^{fl/fl}$ mice as control. Dr. Siv Vingill has previously demonstrated that $Fbxo7^{fl/fl}$ mice show normal behavior up to 12 months of age (Vingill, 2016). Further on, the study by Hagemeyer *et al.*, showed that up to 24 months of age, $Cnp1^{Cre/+}$ mice display normal motor activity, coordination and strength (Hagemeyer *et al.*, 2012). The behavioral analyses revealed a significantly reduced bodyweight of $Cnp1^{Cre/+};Fbxo7^{fl/fl}$ mice as compared to controls, likely due to the aforementioned muscle atrophy (**Figure 3.1.3a**). While analyzing hind limb claspings, $Cnp1^{Cre/+};Fbxo7^{fl/fl}$ mice scored significantly worse than control mice. However, cKO mice displayed rather a weakness of the hind limbs, than a claspings phenotype (**Figure 3.1.3b**). In addition, $Cnp1^{Cre/+};Fbxo7^{fl/fl}$ mice demonstrated muscle weakness, as their ability to hold on to the inverted grid was significantly reduced (**Figure 3.1.3c**). In order to assess motor coordination, mice performed the rotarod test. The procedure was repeated 3 and 24

3.1 Systemic characterization of *Cnp1*^{Cre/+};*Fbxo7*^{fl/fl} mice

hours after the initial examination. The endurance of cKO mice was decreased, as mice fell off the rotating rod much faster than control mice. Moreover, the performance of *Cnp1*^{Cre/+};*Fbxo7*^{fl/fl} mice on the rotarod did not improve, since their learning curve did not increase over time (**Figure 3.1.3d**). To further examine motor coordination, a balance beam test was performed. While running across a 12mm and 6mm beam, the cKO mice required more time and showed a lower coordination score on the 6mm beam than control mice, due to more frequent slips (**Figure 3.1.3e**). Anxiety and locomotion was tested by performing an open field test. *Cnp1*^{Cre/+};*Fbxo7*^{fl/fl} mice did not show any signs of anxiety, but the distance they travelled was significantly shorter than of controls (**Figure 3.1.3f**). Taken together, these results provide strong evidence that loss of *Fbxo7* in myelinating cells leads to decreased mobility, paresis of the hind limbs, resulting from muscle weakness and an overall reduced motor performance.

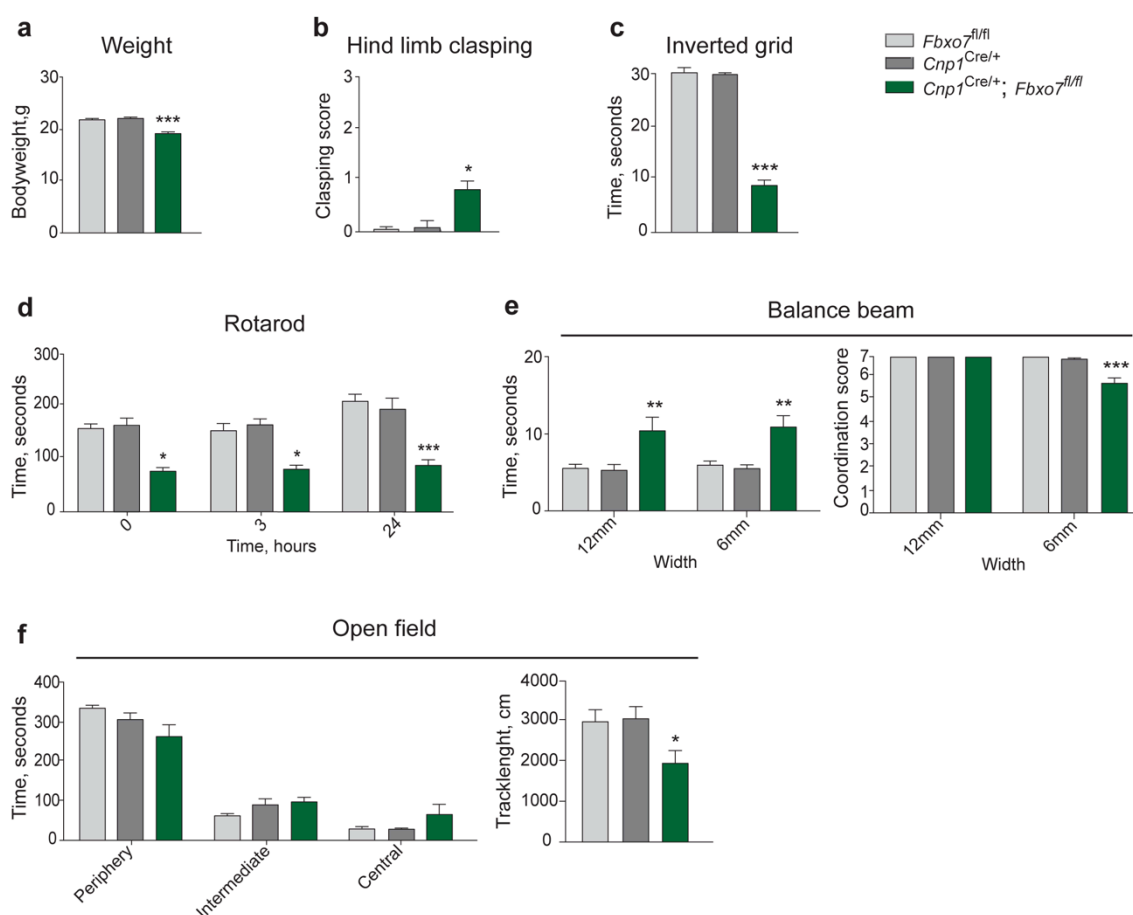


Figure 3.1.3 *Cnp1*^{Cre/+};*Fbxo7*^{fl/fl} mice show reduced motor performance, due to paresis of hind limbs and muscle weakness.

(a)-(f) 6 week-old *Fbxo7*^{fl/fl} (n = 8), *Cnp1*^{Cre/+} (n = 9) and *Cnp1*^{Cre/+};*Fbxo7*^{fl/fl} (n = 10) mice were subjected to the following tests: (a) body weight, (b) tail suspension test (0 = normal, 3 = strong hind limb clasp) and (c) time spent on inverted grid. Further on, a (d) rotarod test at 0, 3 and 24h was performed, as well as a (e) balance beam test with a beam of 6mm or 12mm width, respectively. Here, the time to cross the beam and a

3.2 Cellular characterization of *Cnp1*^{Cre/+};*Fbxo7*^{fl/fl} mice

coordination score were measured (0 = unable to cross beam, 7 = normal). Finally an (f) open field test was conducted and the track lengths as well as the time spent in a specific area were monitored. (One-way ANOVA or two-way ANOVA, including Bonferroni post-test, *P < 0.05, **P < 0.01, ***P < 0.001, mean ± s.e.m.). These analyses were performed by Dr. Siv Vingill.

3.2 Cellular characterization of *Cnp1*^{Cre/+};*Fbxo7*^{fl/fl} mice

In our lab, we investigated the impact of *Fbxo7* deletion on different cell types of the nervous system, dissecting its functions at the cellular level. Conditional knockout mice, in which *Fbxo7* was deleted from the forebrain, did not exhibit neuronal loss in the cortex, however demonstrated astrogliosis and microgliosis (Vingill et al., 2016). In addition, deletion of *Fbxo7* from dopaminergic neurons did not induce neuronal cell death in the substantia nigra, but led to an increase in astrogliosis in the midbrain. The conventional *Fbxo7* knockout mice, which died prematurely at P21, also showed astrogliosis and only a minimal increase in apoptosis in the cortex (Brockelt, 2015; Vingill, 2016). In the following experiments, I analyzed the effect of *Fbxo7* deletion on myelinating cells, the axon-glia interaction and their environment.

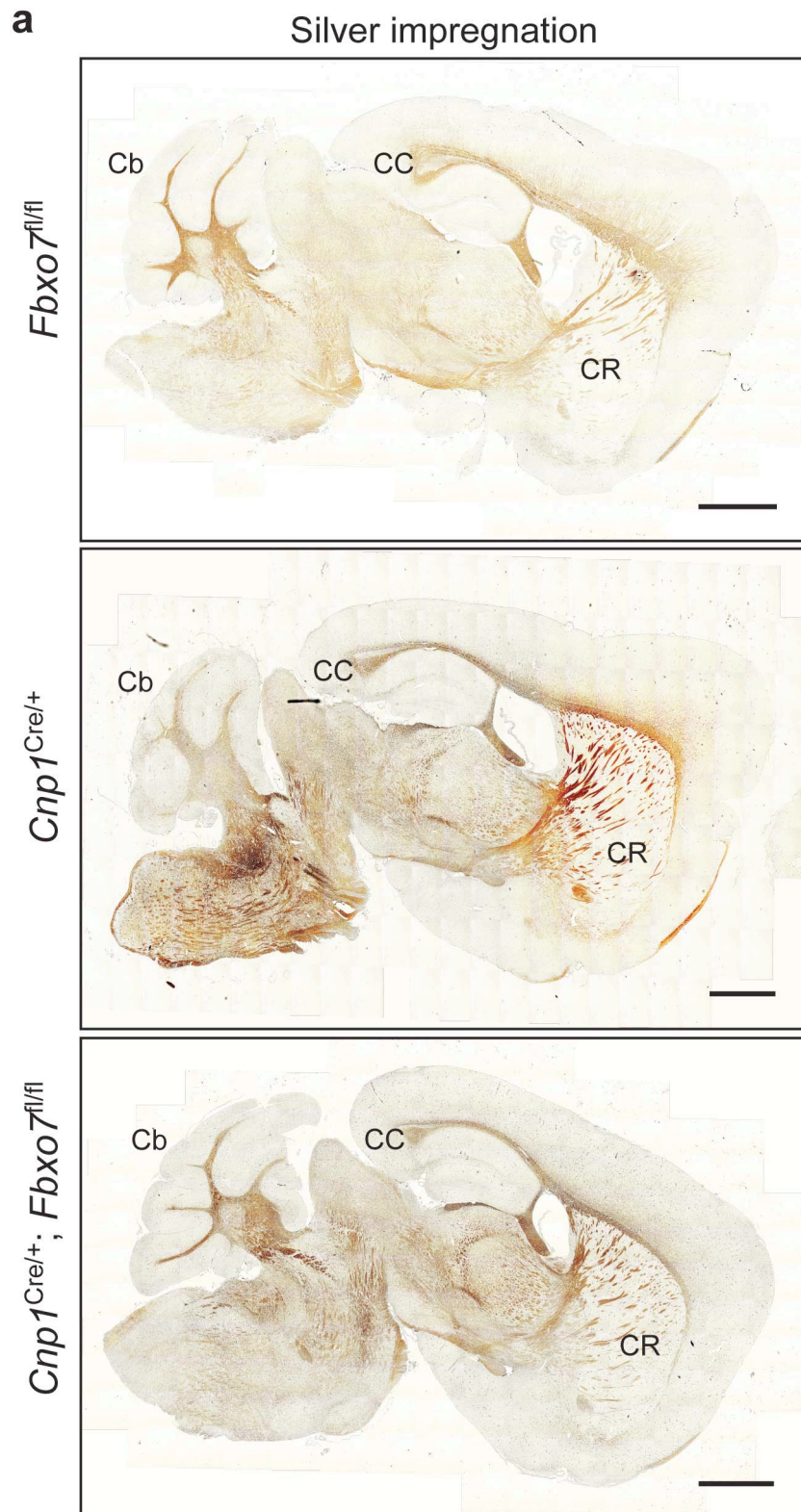
3.2.1 Loss of *Fbxo7* does not affect myelination but leads to a shift in axon caliber

To characterize the presented phenotype at the neuropathological level, I carried out histological analyses and determined if deletion of *Fbxo7* led to structural changes within myelinating cells. Therefore, I stained myelinated fiber tracts on sagittal brain sections of 3-month-old *Fbxo7*^{fl/fl}, *Cnp1*^{Cre/+} and *Cnp1*^{Cre/+};*Fbxo7*^{fl/fl} mice according to the Gallya's silver impregnation protocol, but found no obvious difference between genotypes. There was no sign of increased or decreased thickness of myelinated fiber tracts that would indicate abnormalities in myelinated axons (**Figure 3.2.1a**).

Furthermore, I performed immunohistological stainings of spinal cord cross-sections of 3-month-old *Cnp1*^{Cre/+};*Fbxo7*^{fl/+} and *Cnp1*^{Cre/+};*Fbxo7*^{fl/fl} mice and used myelin proteolipid protein (PLP) as marker. Quantification of PLP⁺ area showed no difference in myelinated tracts of the CNS between cKO and control mice (**Figure 3.2.1b**).

To investigate changes in myelination in the PNS, I stained longitudinal sections of sciatic nerve from 3-month-old *Fbxo7*^{fl/fl} and *Cnp1*^{Cre/+};*Fbxo7*^{fl/fl} mice, with an antibody against myelin basic protein (MBP). Since PLP is of lower abundance in Schwann cells, but only of very low abundance in Schwann cell myelin, a staining with MBP was preferred

(Kamholz et al., 1992). The analysis of MBP⁺ area did not reveal any change in MBP levels in the PNS between cKO and control mice (**Figure 3.2.1c**). I analyzed and quantified fluorescent images, using a customized macro designed by Dr. Miso Mitkovski. Taken together, I did not detect any structural changes in myelination in the CNS or PNS.



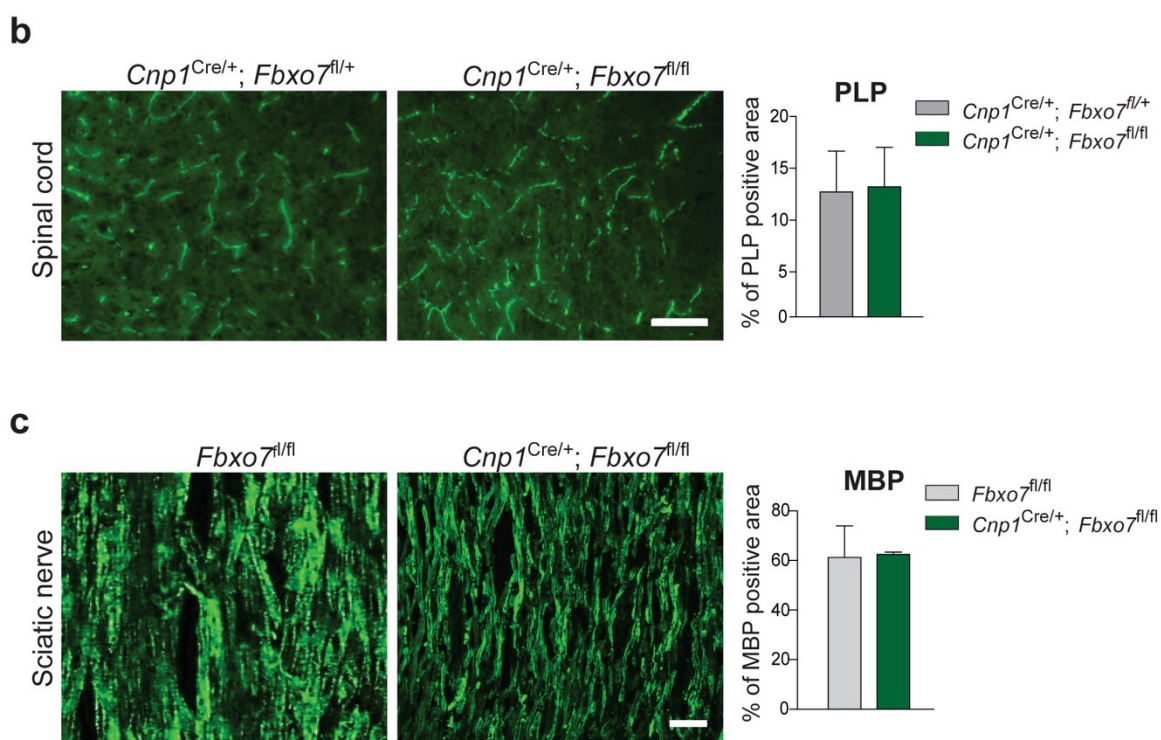
3.2 Cellular characterization of *Cnp1*^{Cre/+};*Fbxo7*^{fl/fl} mice

Figure 3.2.1 *Cnp1*^{Cre/+};*Fbxo7*^{fl/fl} mice present no histological changes in myelination.

(a) Gallyas staining of 3-month-old *Fbxo7*^{fl/fl}, *Cnp1*^{Cre/+} and *Cnp1*^{Cre/+};*Fbxo7*^{fl/fl} sagittal brain sections. Cb = cerebellum, CC = corpus callosum, CR = corona radiata. Scale bar = 0.5mm. (b) Cryo-cross-sections of spinal cords from 3-month-old *Cnp1*^{Cre/+};*Fbxo7*^{fl/+} and *Cnp1*^{Cre/+};*Fbxo7*^{fl/fl} mice were subjected to immunohistochemistry using PLP antibody. Sections were taken from lumbar segment 1-3 of the spinal cord. Three mice per genotype and two technical repeats per animal were included in the analyses. The percentage of area stained was quantified using a customized macro (unpaired t-test, mean \pm s.e.m.). Scale bar = 50 μ m. (c) Representative images of longitudinal cryo-sections of sciatic nerves from 3-month-old *Fbxo7*^{fl/fl} and *Cnp1*^{Cre/+};*Fbxo7*^{fl/fl} mice that were subjected to immunohistochemistry with an MBP antibody. Three biological and two technical repeats per genotype were included in the analyses. The percentage of area stained was quantified using a customized macro (unpaired t-test, mean \pm s.e.m.). Scale bar = 50 μ m.

To investigate ultrastructural changes and the compaction of myelin layers, I decided to take advantage of electron microscopy. In collaboration with Dr. Wiebke Möbius, I subjected optic nerve and sciatic nerve samples of 3-month-old *Cnp1*^{Cre/+} and *Cnp1*^{Cre/+};*Fbxo7*^{fl/fl} mice to electron microscopic analyses. Both, embedding of samples and acquisition of pictures were done with the support from Boguscha Sadowski and Torben Ruhweden. Cross-sections were quantified by calculating the g-ratio, which serves as benchmark for myelin thickness. The analysis of optic nerve was performed by Dr. Siv Vingill and showed an equal distribution of g-ratio values for cKO and control mice, indicating no change in myelination in the CNS of *Cnp1*^{Cre/+};*Fbxo7*^{fl/fl} mice (**Figure 3.2.2a**). The average g-ratio for myelinated axons in the CNS is approximately 0.77 according to

literature, however the quantification of our measurements revealed an average value of 0.7 for both cKO and control (Chomiak and Hu, 2009) (**Figure 3.2.2b**). To detect more subtle changes, which might only be appreciated within smaller subpopulations, I grouped the measured g-ratio values as following: Values from 0 – 0.64 represented hypermyelination, values between 0.65 – 0.75 reflected normal myelination and g-ratios from 0.76 – 0.90 identified hypomyelination. The data showed that the majority of measured axons (76% in cKO, 65% in control mice) displayed a normal myelination. The percentage of axons that displayed hyper- or hypomyelination was negligibly small (hypermyelination: 7% in cKO, 10% in control mice; hypomyelination: 17% in cKO, 25% in control mice) and only represented the edges of a Gaussian distribution. Interestingly, axons of *Cnp1*^{Cre/+};*Fbxo7*^{fl/fl} mice presented a significant shift towards large-caliber axons throughout all groups as compared to control (**Figure 3.2.2c**). With these results, I show that loss of *Fbxo7* in oligodendrocytes does not severely influence myelination in the CNS. However deletion of *Fbxo7* triggers a shift in axon caliber in the optic nerve of *Cnp1*^{Cre/+};*Fbxo7*^{fl/fl} mice.

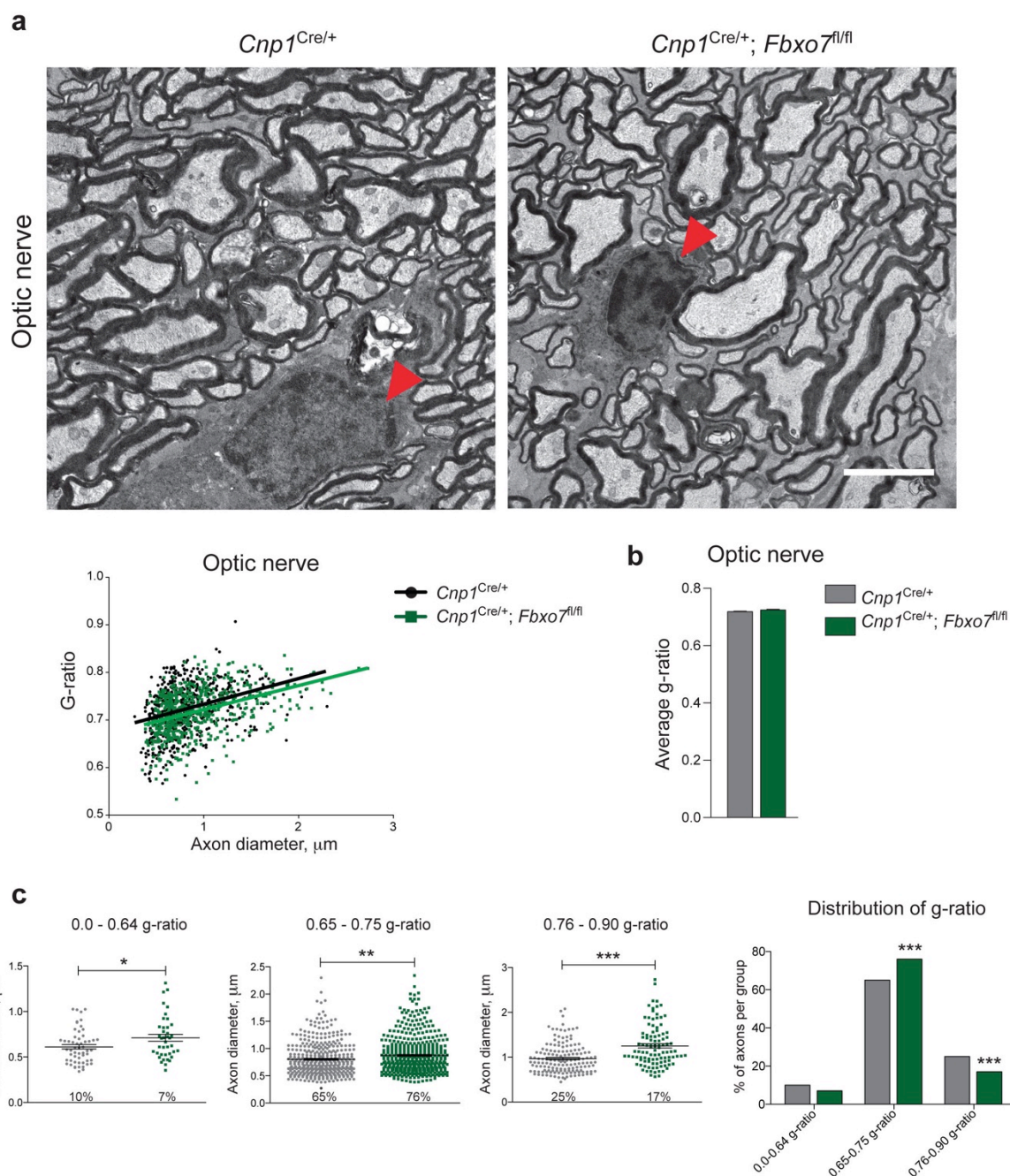
3.2 Cellular characterization of *Cnp1*^{Cre/+};*Fbxo7*^{fl/fl} mice

Figure 3.2.2 *Cnp1*^{Cre/+};*Fbxo7*^{fl/fl} mice do not display any major alterations in CNS myelination, but a shift in axon caliber.

(a) Cross-sections of optic nerve from 3-month-old *Cnp1*^{Cre/+} and *Cnp1*^{Cre/+};*Fbxo7*^{fl/fl} mice were obtained by electron microscopy. G-ratio was measured from three mice per genotype and displayed as scatter plot. 600 axons per genotype were quantified. Arrowheads indicate oligodendrocyte nuclei. Scale bar = 3 μm . Analysis was performed by Dr. Siv Vingill. (b) Average g-ratio of all measured axons from *Cnp1*^{Cre/+} and *Cnp1*^{Cre/+};*Fbxo7*^{fl/fl} mice (unpaired t-test, mean \pm s.e.m.). (c) Data obtained in (a) were sorted into 3 groups. G-ratio values 0 – 0.64 = hypermyelination, 0.65 – 0.75 = normal myelination and 0.76 – 0.90 = hypomyelination (unpaired t-test, *P < 0.05, **P < 0.01, ***P < 0.001, mean \pm s.e.m.). The quantity of axons per group was analyzed and displayed as percentage (Chi-squared test, ***P < 0.001).

3.2 Cellular characterization of *Cnp1*^{Cre/+};*Fbxo7*^{fl/fl} mice

Analogously to the CNS, I examined myelination in the PNS. I measured the g-ratio of sciatic nerve cross-sections from *Cnp1*^{Cre/+};*Fbxo7*^{fl/fl} and control mice, and found that the distribution of values of cKO and control mice was comparable. However, I observed that while the majority of data from both groups were similarly scattered, a small but noticeable fractions seemed to differ: a small population of axons in the cKO group indicated greater g-ratios (i) and in addition a second population of axons in the control group displayed larger diameter (ii) (**Figure 3.2.3a**). According to literature, the average g-ratio in the PNS equals approximately 0.6 (Rushton, 1951), however both our cKO and control mice revealed an average g-ratio of approximately 0.53 (**Figure 3.2.3b**). To flesh out the differences (i) in more detail, I subdivided the g-ratio measurements into classes. I chose values from 0 – 0.40 to represent hypermyelination, values from 0.41 – 0.62 should indicating normal myelination and g-ratios between 0.63 – 1 reflected hypomyelination. The results showed that majority of axons from cKO and control mice displayed a normal myelination (69% in cKO, 79% in control mice). Although the percentage of hypermyelinated and hypomyelinated axons in both genotypes were negligibly small (hypermyelination: 4% in cKO, 6% in control mice), cKO mice presented surprisingly more significant axons, which were hypomyelinated as compared to control (27% in cKO, 15% in control mice). However, this small population of hypermyelinated axons in cKO and control mice only displays a small percentage of measured axons in the PNS. Regarding axon caliber (ii), cKO mice displayed significantly smaller axons and a lack of large caliber axons as compared to control. (**Figure 3.2.3c**). With these results I show that *Fbxo7* deletion in Schwann cells did not cause major structural changes in myelin, however 12% more axons of cKO mice displayed increased hypomyelination than in control mice. Moreover the sciatic nerve of *Cnp1*^{Cre/+};*Fbxo7*^{fl/fl} mice contained significantly smaller axons, indicating a change in axon caliber upon loss of *Fbxo7* from Schwann cells.

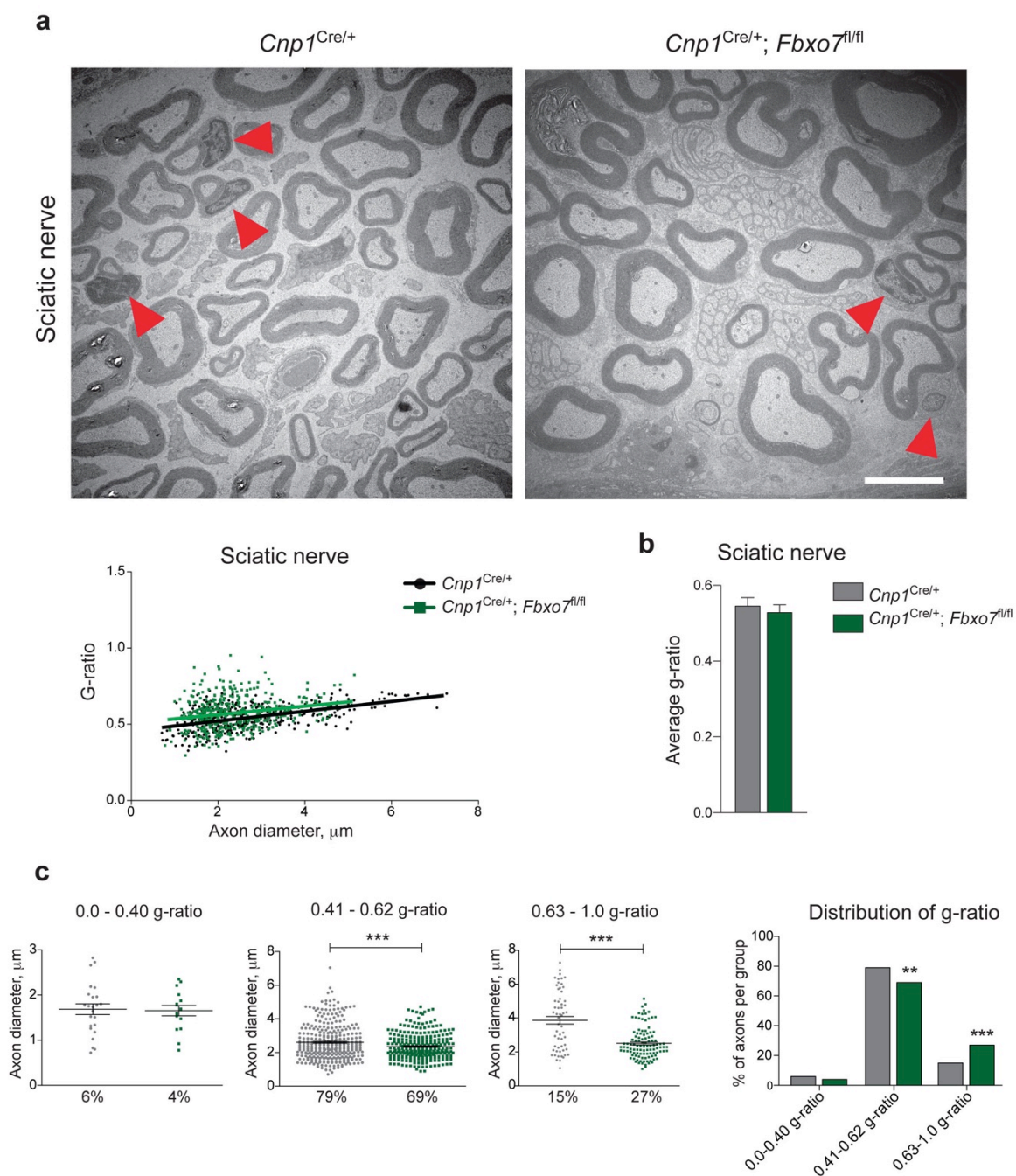
3.2 Cellular characterization of *Cnp1*^{Cre/+};*Fbxo7*^{fl/fl} mice

Figure 3.2.3 *Cnp1*^{Cre/+};*Fbxo7*^{fl/fl} mice show no severe changes in PNS myelination, but a shift in axon caliber.

(a) Representative images of sciatic nerve cross-sections from 3-month-old *Cnp1*^{Cre/+} and *Cnp1*^{Cre/+};*Fbxo7*^{fl/fl} mice. Images were obtained by electron microscopy and g-ratio was measured from four mice per genotype. Scatter plot presents 400 axons per genotype. Arrowheads indicate Schwann cell nuclei of myelinated axons. Scale bar = 3 μm . (b) Average g-ratio of all measured axons from *Cnp1*^{Cre/+} and *Cnp1*^{Cre/+};*Fbxo7*^{fl/fl} mice (unpaired t-test, mean \pm s.e.m.). (c) Analysis of (a) was grouped into 3 classes: g-ratio of 0 – 0.40 = hypermyelination, 0.41 – 0.62 = normal myelination group and 0.63 – 1 = hypomyelination (unpaired t-test, *** $P < 0.001$, mean \pm s.e.m.). Percentage of axons per group was analyzed (N-1 Chi-squared test, * $P < 0.05$, *** $P < 0.001$).

3.2 Cellular characterization of *Cnp1*^{Cre/+};*Fbxo7*^{fl/fl} mice

To examine if knockout of *Fbxo7* might influence the abundance of myelinating cells, I counted oligodendrocyte and Schwann cell nuclei in optic and sciatic nerve, respectively. Nuclei were counted from the same electron microscopic images that were used for g-ratio measurement. The results showed no significant change in the quantity of oligodendrocyte nuclei (**Figure 3.2.4a**) or Schwann cell nuclei. However a trend of slightly less Schwann cell nuclei was seen in *Cnp1*^{Cre/+};*Fbxo7*^{fl/fl} mice as compared to control (**Figure 3.2.4b**).

While evaluating morphological changes within the sciatic nerve, I primarily focused on myelinated axons. However, non-myelinated small diameter axons, so-called C fibers, are also found in the sciatic nerve. C fibers are grouped together and form so-called Remak bundles, in which Remak cells engulf the fibers and cluster them together. To analyze the effect of *Fbxo7* deletion on Remak bundles, I counted the nuclei of Remak cells. As depicted in **Figure 3.2.4c**, the number of Remak cells was not altered.

Moreover, I performed a TUNEL assay on 3-month-old sagittal brain sections from *Fbxo7*^{fl/fl}, *Cnp1*^{Cre/+} and *Cnp1*^{Cre/+};*Fbxo7*^{fl/fl} mice, to determine cell death within white matter of the CNS. There were slightly more apoptotic cells present in the white matter of cerebellum of cKO mice than compared to controls, but this reached not significance. Further on, there was no significant increase in apoptotic cells in corpus callosum in cKO mice when compared to control mice (**Figure 3.2.4d**).

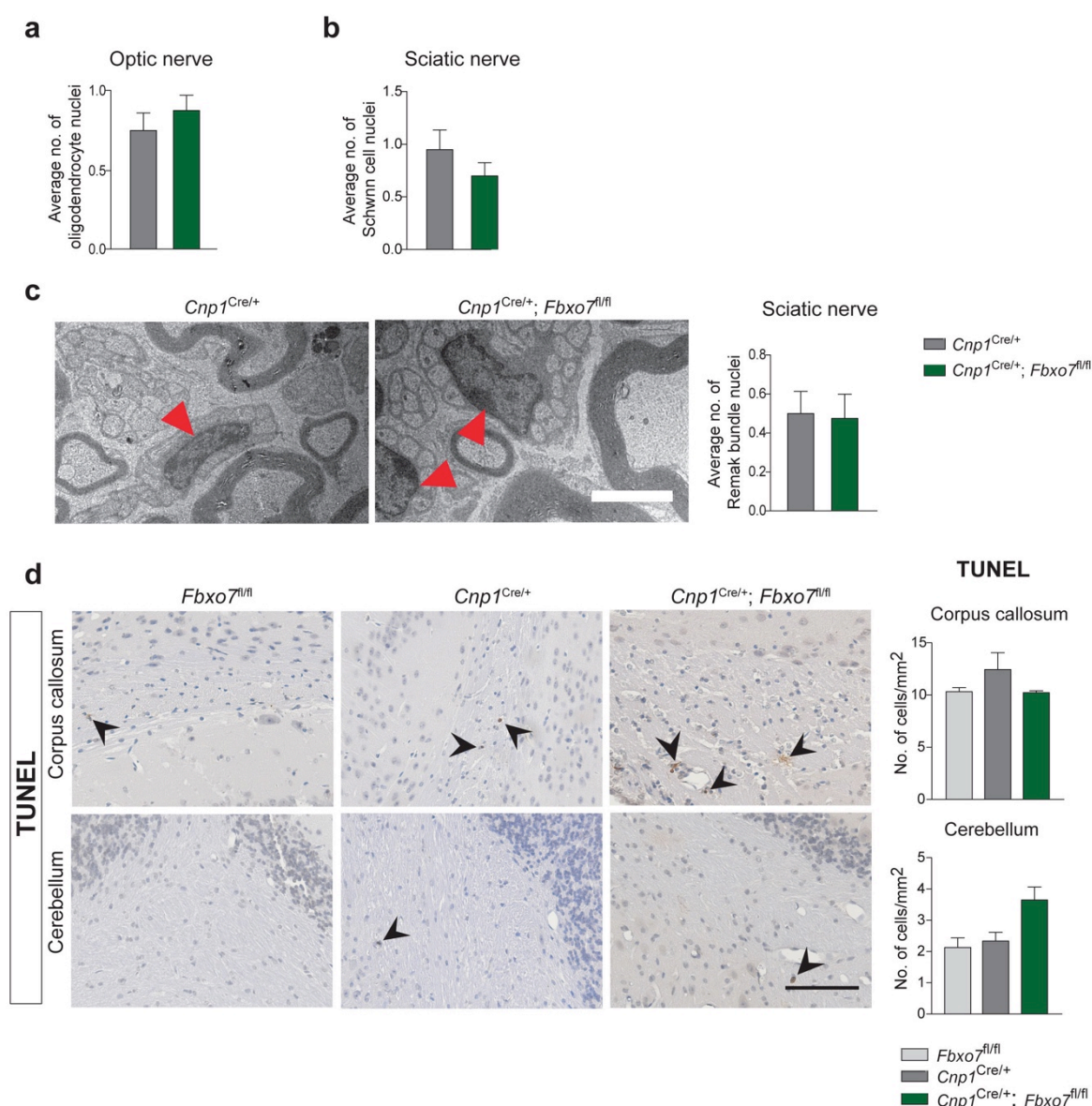
3.2 Cellular characterization of *Cnp1*^{Cre/+};*Fbxo7*^{fl/fl} mice

Figure 3.2.4 *Cnp1*^{Cre/+};*Fbxo7*^{fl/fl} mice display a normal abundance of oligodendrocyte, Schwann cell and Remak cell nuclei.

(a) Number of oligodendrocyte nuclei in optic nerve cross-section of 3-month-old *Cnp1*^{Cre/+} and *Cnp1*^{Cre/+};*Fbxo7*^{fl/fl} mice. Nuclei were counted in the same images as described in 3.2.1.2a. (unpaired t-test, mean \pm s.e.m.). (b) Analysis of Schwann cell nuclei in cross-sections of sciatic nerve from 3-month-old *Cnp1*^{Cre/+} and *Cnp1*^{Cre/+};*Fbxo7*^{fl/fl} mice (same images as described in 3.2.1.3a) (unpaired t-test, mean \pm s.e.m.). (c) Electron microscopy images of sciatic nerve cross-sections from *Cnp1*^{Cre/+} and *Cnp1*^{Cre/+};*Fbxo7*^{fl/fl} mice were analyzed counting Remak bundle nuclei (unpaired t-test, mean \pm s.e.m.). Arrowheads indicate Remak bundle nuclei. Scale bar = 1.5 μ m. (d) TUNEL assay was performed on sagittal paraffin sections of brains from 3-month-old *Fbxo7*^{fl/fl}, *Cnp1*^{Cre/+} and *Cnp1*^{Cre/+};*Fbxo7*^{fl/fl} mice. Three independent animals per group and two technical replicates were analyzed. TUNEL positive cells were counted in corpus callosum and white matter of cerebellum (One-way ANOVA, including Bonferroni post-test, mean \pm s.e.m.). Arrowheads indicate TUNEL⁺ cells. Scale bar = 100 μ m.

3.2.2 *Cnp1*^{Cre/+};*Fbxo7*^{fl/fl} mice display prominent axonal degeneration in the periphery

Although *Fbxo7* was deleted from myelinating cells, my investigations showed no striking impact on myelination in the CNS or PNS. The interaction between myelinating cells and axons is essential for fast propagation of the action potential but also to ensure mutual support and stabilization. Owing to this strong cooperation and growing evidence that bolsters a critical trophic support for axons by myelinating cells (Corfas et al., 2004; Nave, 2010a; Simons and Nave, 2015), I investigated the effects of *Fbxo7* deletion on axonal integrity. I subjected sagittal brain sections of 3-months-old *Fbxo7*^{fl/fl} and *Cnp1*^{Cre/+};*Fbxo7*^{fl/fl} mice to immunohistochemistry using an antibody against amyloid precursor protein (APP). APP is anticipated to accumulate as a result of axonal damage (An et al., 1997). However, I did not observe any change in APP distribution in cKO as compared to control mice, indicating no difference in axonal integrity within corpus callosum and white matter of cerebellum (**Figure 3.2.5a**). While there was no APP accumulation present in the CNS, quantifications of APP staining on longitudinal sciatic nerve sections from 3-month-old *Fbxo7*^{fl/fl}, *Cnp1*^{Cre/+} and *Cnp1*^{Cre/+};*Fbxo7*^{fl/fl} mice showed significant accumulation of APP in cKO tissue (**Figure 3.2.5b**). Collectively, my findings demonstrate that loss of *Fbxo7* results in axonal damage in the sciatic but not optic nerve and thus suggests a greater vulnerability in Schwann cells.

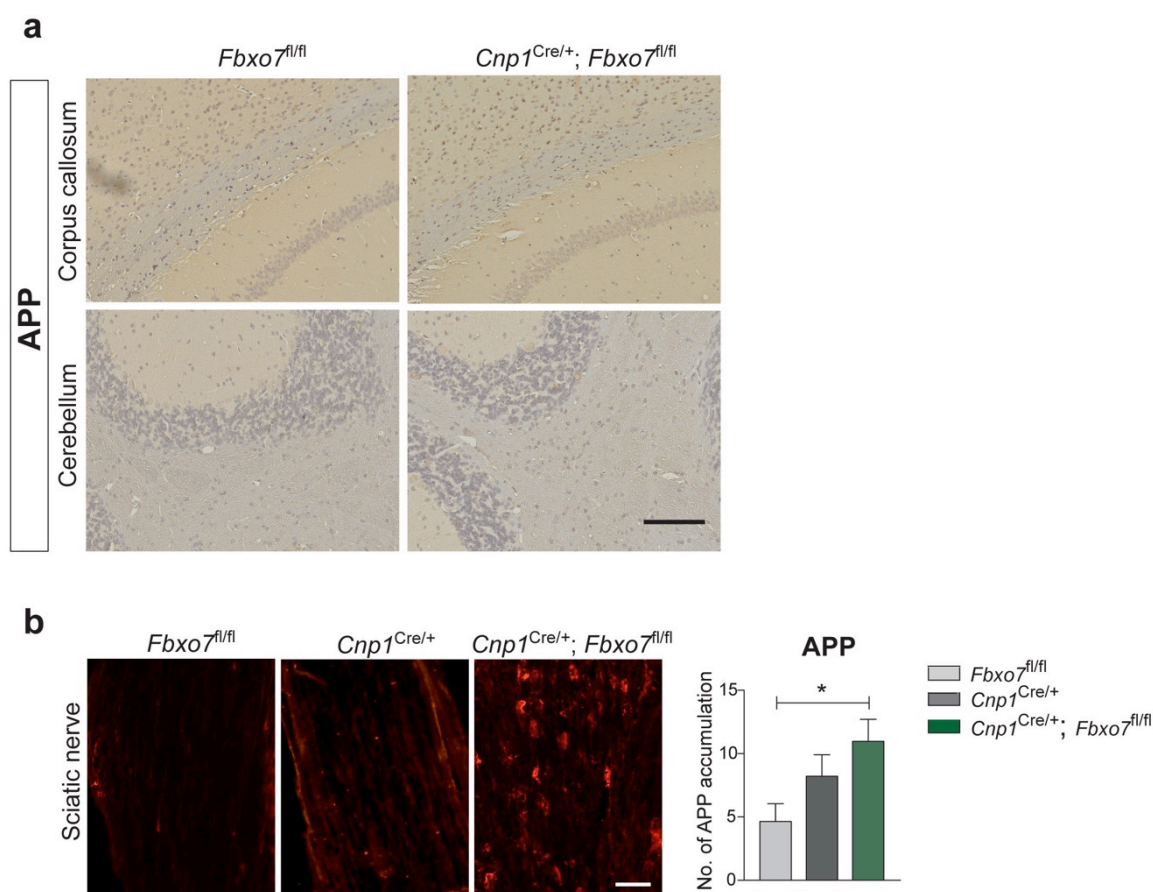
3.2 Cellular characterization of *Cnp1*^{Cre/+};*Fbxo7*^{fl/fl} mice

Figure 3.2.5 *Cnp1*^{Cre/+};*Fbxo7*^{fl/fl} mice show axonal damage in the PNS.

(a) Representative images of sagittal paraffin brain sections of 3-month-old *Fbxo7*^{fl/fl} and *Cnp1*^{Cre/+};*Fbxo7*^{fl/fl} mice, which were immunostained with an APP antibody. Images depict white matter of cerebellum and corpus callosum. Scale bar = 100µm. **(b)** Longitudinal cryo-section of sciatic nerves from 3-month-old *Fbxo7*^{fl/fl}, *Cnp1*^{Cre/+} and *Cnp1*^{Cre/+};*Fbxo7*^{fl/fl} mice were subjected to immunohistochemistry using an antibody against APP. Three independent mice per genotype and three sections from each animal were analyzed. (one-way ANOVA, including Bonferroni post-test, *P < 0.05, mean ± s.e.m). The images were analyzed by applying a customized macro designed by Dr. Miso Mitkovski and further the numbers of APP accumulations were counted. Scale bar = 40µm.

Owing to the observed axonal damage, I decided to analyze any changes in axon morphology and abundance using electron microscopic images of 3-month-old *Cnp1*^{Cre/+} and *Cnp1*^{Cre/+};*Fbxo7*^{fl/fl} mice. Similar to previous analyses, g-ratio measurements of optic nerve samples were grouped but this time according to axon diameter. The groups included axons of either < 1µm or > 1µm in diameter. The results showed that the majority of axons from control and cKO mice displayed a diameter of < 1µm (75% in control, 66% in cKO). Interestingly, the distribution of axon sizes further revealed that *Cnp1*^{Cre/+};*Fbxo7*^{fl/fl} mice harbored significantly more axons with a diameter greater than 1µm as compared to control (25% in control, 34% in cKO). This indicates that loss of *Fbxo7* in oligodendrocytes

3.2 Cellular characterization of *Cnp1*^{Cre/+};*Fbxo7*^{fl/fl} mice

leads to a mild shift towards large caliber axons in the optic nerve. Moreover, the analysis showed no difference in g-ratio between cKO and control mice, which matched my previous result (**Figure 3.2.6a**).

For the quantification of PNS axon calibers, g-ratio values from sciatic nerve were grouped as follows: axon diameter from 0 – 1 μ m, 2 – 3 μ m and > 4 μ m. The results showed that the majority of axons of *Cnp1*^{Cre/+};*Fbxo7*^{fl/fl} and *Cnp1*^{Cre/+} mice had a diameter in the range of 2 – 3 μ m (57% in cKO, 50% in control). Interestingly, *Cnp1*^{Cre/+};*Fbxo7*^{fl/fl} mice revealed a shift in axon caliber within the sciatic nerve: while axons larger than 4 μ m were significantly less abundant in cKO mice (5% in cKO and 17% in control), the number of small caliber axons that were < 4 μ m in diameter were increased in *Cnp1*^{Cre/+};*Fbxo7*^{fl/fl} mice as compared to controls (summarized from both groups: 95% in cKO, 83% in control). Additionally, the analysis confirmed my previous result and showed that sciatic nerve axons of cKO mice were rather hypomyelinated than axons of controls (**Figure 3.2.6b**). In conclusion, *Fbxo7* deletion within oligodendrocytes leads to an increase in axon diameter, without significant changes in myelination, whereas in Schwann cells loss of *Fbxo7* leads to a reduction in large caliber axons. Supporting my previous assumption, this analysis further indicated a moderate hypomyelination of PNS axons.

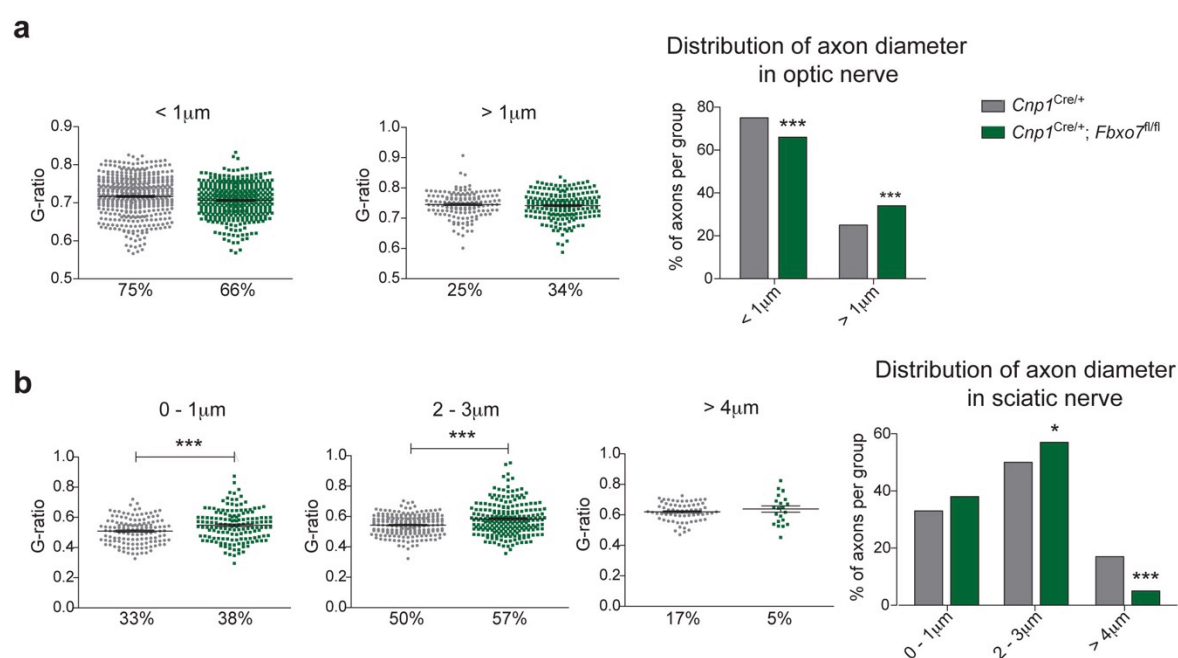


Figure 3.2.6 Loss of FBXO7 induces an increase in axon caliber in the CNS and a shift towards small caliber axons in the PNS of *Cnp1*^{Cre/+};*Fbxo7*^{fl/fl} mice.

(a) G-ratio measurement from optic nerve cross-sections of 3-month-old *Cnp1*^{Cre/+} and *Cnp1*^{Cre/+};*Fbxo7*^{fl/fl} mice were grouped according to axonal diameter (< 1 μ m, > 1 μ m). Three independent mice per genotype were included and 600 axons per condition analyzed (unpaired t-test, mean \pm s.e.m.). The percentage of axons per group was analyzed (N-1 Chi-squared test, ***P < 0.001). (b) Measured g-ratios from sciatic nerve cross-

3.2 Cellular characterization of *Cnp1*^{Cre/+};*Fbxo7*^{fl/fl} mice

sections of 3-month-old *Cnp1*^{Cre/+} and *Cnp1*^{Cre/+};*Fbxo7*^{fl/fl} mice were classified according to the axonal diameter (0 – 1µm, 2 – 3µm, > 4µm). Four independent animals were analyzed per genotype and 400 axons per condition measured (unpaired t-test, ***P < 0.001, mean ± s.e.m.). The percentage of axons per group was analyzed (N-1 Chi-squared test, *P < 0.05, ***P < 0.001).

Deletion of *Fbxo7* induced a shift in axon diameter within the optic nerve and sciatic nerve. To investigate whether or not this shift in axon caliber correlates with changes in axon number, I counted myelinated axons. I analyzed axons on electron microscopic images from optic nerve sections of 3-month-old *Cnp1*^{Cre/+} and *Cnp1*^{Cre/+};*Fbxo7*^{fl/fl} mice, but found no difference in the number of axons within the optic nerve of cKO and control mice (**Figure 3.2.7a**). In addition, I assessed the number of degenerated axons in the optic nerve. Here, *Cnp1*^{Cre/+};*Fbxo7*^{fl/fl} mice displayed a slight but not significant increase in degenerated axons (**Figure 3.2.7b**).

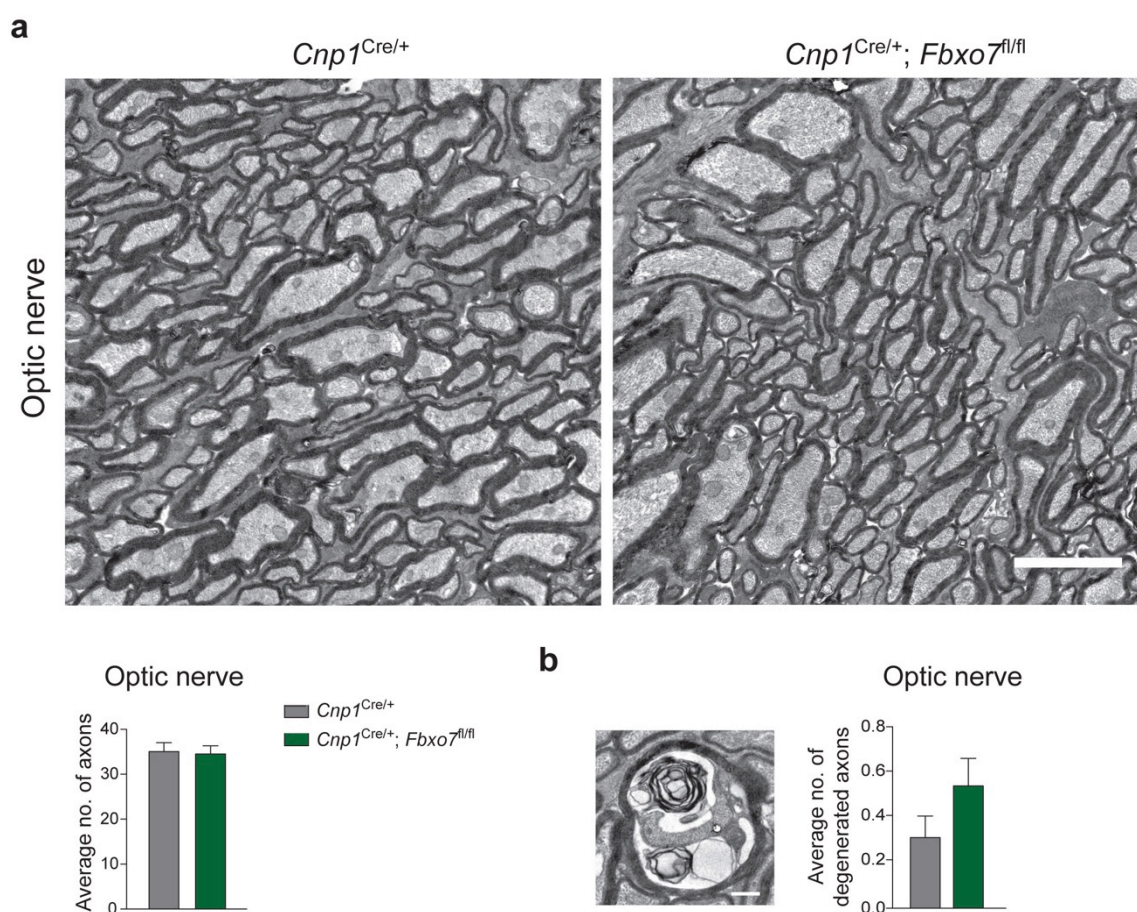


Figure 3.2.7 *Cnp1*^{Cre/+};*Fbxo7*^{fl/fl} mice show no significant increase in the number of axons as well as degenerated axons in the optic nerve.

(a) Average number of axons within optic nerve of 3-month-old *Cnp1*^{Cre/+} and *Cnp1*^{Cre/+};*Fbxo7*^{fl/fl} mice. Three mice per condition and 10 images per mouse were analyzed (unpaired t-test, mean ± s.e.m.). Images depict

3.2 Cellular characterization of *Cnp1*^{Cre/+};*Fbxo7*^{fl/fl} mice

cross-sections of optic nerve. Scale bar = 3 μ m. **(b)** Representative image of degenerated axon from optic nerve of 3-month-old *Cnp1*^{Cre/+};*Fbxo7*^{fl/fl} mouse. Images described in (a) were used to count the average number of degenerated axons from three mice per genotype and within 10 images per mouse (unpaired t-test, mean \pm s.e.m.). Scale bar = 0.5 μ m.

I further quantified the abundance of myelinated axons and axonal degeneration depicted on electron microscopic images from sciatic nerve sections of 3-month-old *Cnp1*^{Cre/+} and *Cnp1*^{Cre/+};*Fbxo7*^{fl/fl} mice. The results showed a significant loss of myelinated axons in cKO mice as compared to control (**Figure 3.2.8a**). Moreover, *Cnp1*^{Cre/+};*Fbxo7*^{fl/fl} mice revealed a significant increase in degenerated axons within the sciatic nerve (**Figure 3.2.8b**). Furthermore, I counted the number of Remak bundles in the sciatic nerve, but saw no difference between *Cnp1*^{Cre/+};*Fbxo7*^{fl/fl} and control mice (**Figure 3.2.8c**). The number of degenerated Remak bundles was slightly but not significantly higher in cKO mice than in controls (**Figure 3.2.8d**). Overall, loss of *Fbxo7* in myelinating cells leads to axonal degeneration in the optic and sciatic nerve. However, knockout of *Fbxo7* appears to be more detrimental for large caliber axons in the PNS as compared to axons in the CNS, since the PNS shows a greater axonal loss.

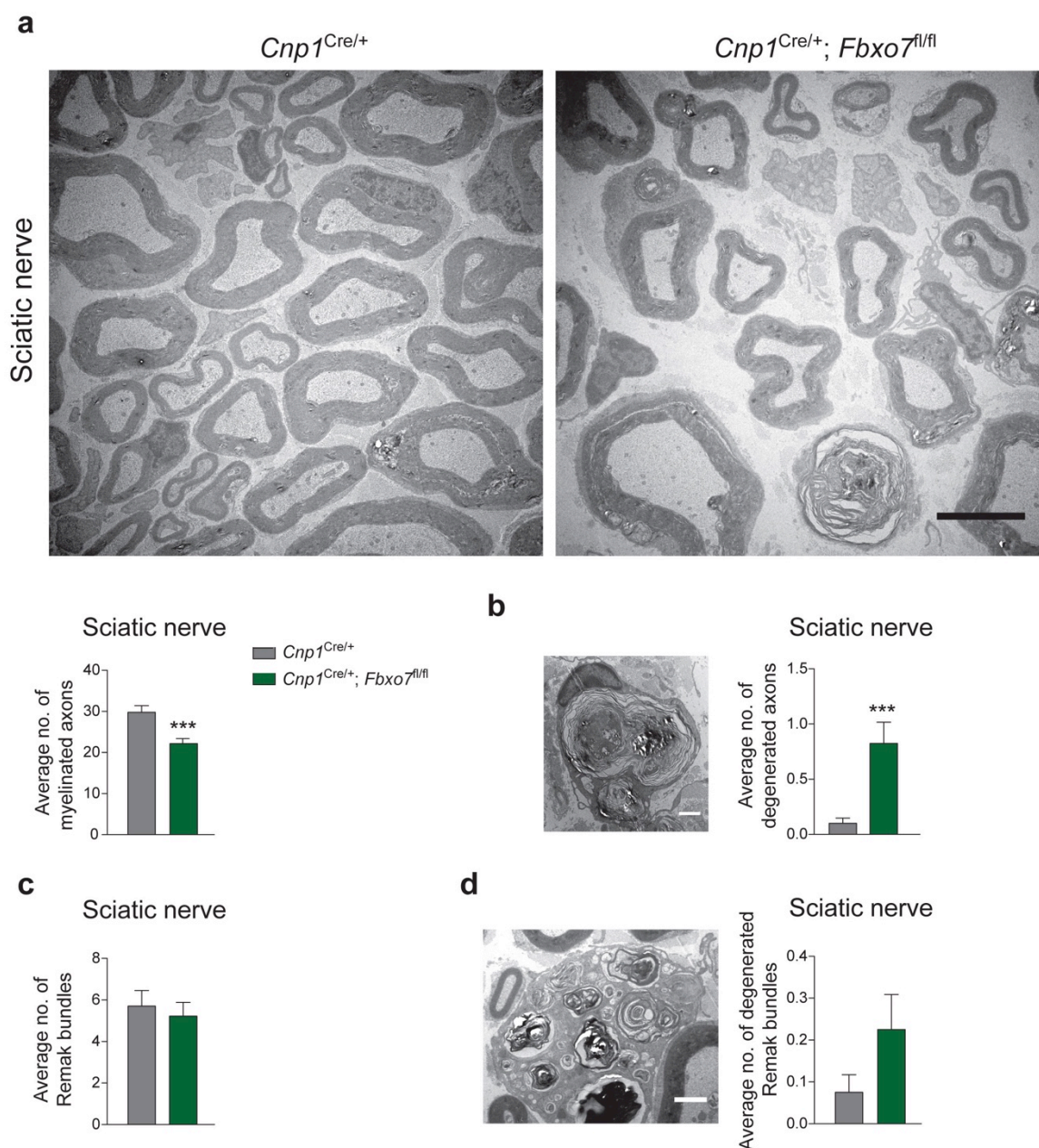


Figure 3.2.8 Loss of *Fbxo7* leads to increased axonal degeneration within the sciatic nerve of *Cnp1*^{Cre/+};*Fbxo7*^{fl/fl} mice.

(a)-(d) Sciatic nerve cross-sections of 3-month-old *Cnp1*^{Cre/+} and *Cnp1*^{Cre/+};*Fbxo7*^{fl/fl} mice were analyzed. Four independent animals per condition and 10 images per mouse were included in the analyses (unpaired t-test, ****P* < 0.001, mean ± s.e.m.). (a) Representative electron microscopic images of cross-sections from sciatic nerve. The average number of myelinated axons was counted. Scale bar = 3µm. (b) Further on, the average number of degenerated axons was counted. Electron microscopic image from sciatic nerve represents axonal degeneration. Scale bar = 1µm. (c) The number of Remak bundles was assessed. (d) Analysis of degenerated Remak bundles. Electron microscopic image represents degenerated Remak bundles in sciatic nerve of 3-month-old *Cnp1*^{Cre/+};*Fbxo7*^{fl/fl} mouse. Scale bar = 1µm.

3.2 Cellular characterization of *Cnp1*^{Cre/+};*Fbxo7*^{fl/fl} mice

In order to further understand the underlying pathophysiology of *Cnp1*^{Cre/+};*Fbxo7*^{fl/fl} mice, we performed electrophysiological recordings. The pathology of knockout mice was predominantly located in the periphery and *Fbxo7* deletion led to a greater deterioration of PNS than of CNS axons. Thus, we decided to examine electrophysiological changes of the sciatic nerve. Electrophysiological recordings were performed by Dr. Robert Fledrich, who analyzed 2-month-old *Cnp1*^{Cre/+};*Fbxo7*^{fl/+} and *Cnp1*^{Cre/+};*Fbxo7*^{fl/fl} mice. The key parameters for quantification of peripheral nerve function included the compound muscle action potential (CMAP), nerve conduction velocity (NCV) and distal motor latency (DML). The CMAP is an indicator for the quantity of functional axons. Analysis of *Cnp1*^{Cre/+};*Fbxo7*^{fl/fl} mice showed significant decrease in CMAP at distal and proximal position, thus demonstrating loss of axons in the sciatic nerve (**Figure 3.2.9a**). In addition, *Cnp1*^{Cre/+};*Fbxo7*^{fl/fl} mice exhibited a significant reduction in NCV, further indicating axonal loss. However, a significant decrease in NCV could also imply segmental demyelination (Somlai, 2016) (**Figure 3.2.9b**). These potential changes in myelination can further be elucidated by measuring the DML as demyelination would lead to a prolonged DML. The measurements of the DML did not show any difference between cKO and control mice, suggesting no significant alteration of myelination (**Figure 3.2.9c**). These analyses supported my previous results and showed that ablation of *Fbxo7* from myelinating cells leads to severe axonal loss without significantly affecting myelination in the sciatic nerve.

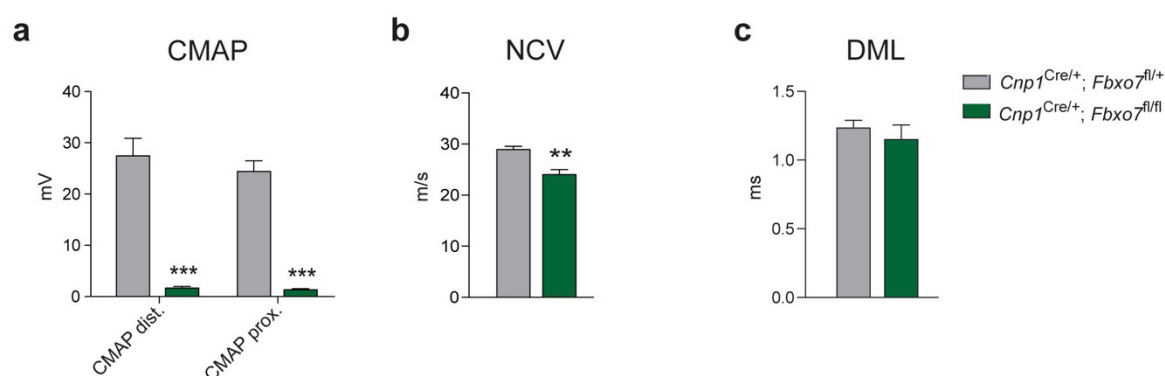


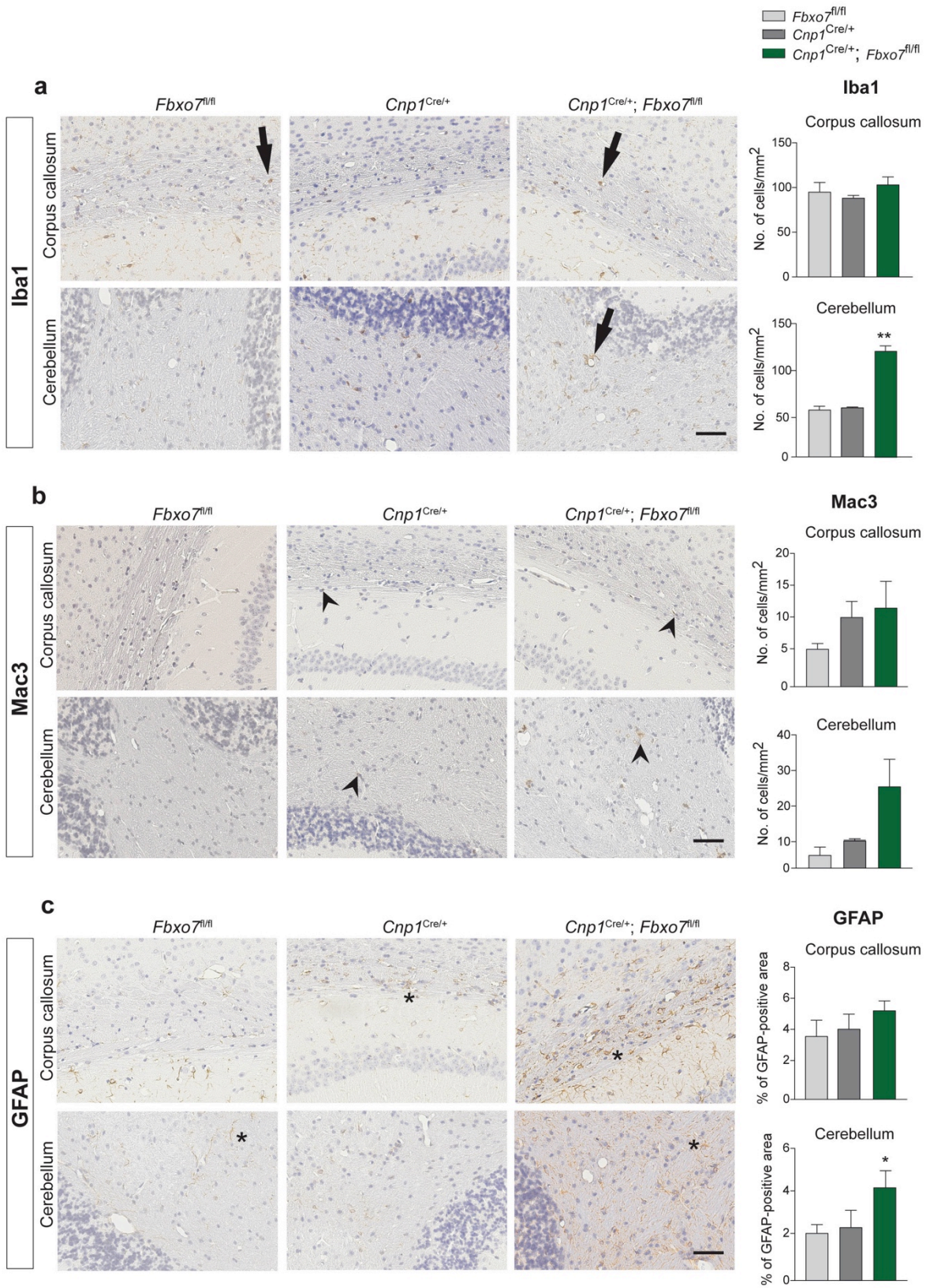
Figure 3.2.9 Severe axonal degeneration in the sciatic nerve of *Cnp1*^{Cre/+};*Fbxo7*^{fl/fl} mice.

(a)-(c) Electrophysiological recordings were measured from sciatic nerve of 2-month-old *Cnp1*^{Cre/+};*Fbxo7*^{fl/+} and *Cnp1*^{Cre/+};*Fbxo7*^{fl/fl} mice. (a) Compound muscle action potential (CMAP). (b) Nerve conduction velocity (NCV). (c) Distal motor latency (DML). Analyses were performed on 6 independent mice per condition (unpaired t-test, **P < 0.01, ***P < 0.001, mean ± s.e.m.). Electrophysiological recordings were performed by Dr. Robert Fledrich.

3.2.3 Knockdown of *Fbxo7* from myelinating cells leads to increased inflammation

The degeneration of cells and overall damage of tissue often evokes an immune response and as seen in many neurodegenerative diseases can induce neuroinflammation (Damier et al., 1993; Wyss-Coray and Mucke, 2002). Since *Cnp1^{Cre/+};Fbxo7^{fl/fl}* mice featured increased axonal loss in both CNS and PNS, I searched for inflammatory events that would accompany the degenerative event in corpus callosum and white matter of cerebellum. Hence, I subjected 3-month-old sagittal brain sections from *Fbxo7^{fl/fl}*, *Cnp1^{Cre/+}* and *Cnp1^{Cre/+};Fbxo7^{fl/fl}* mice to immunohistochemical analysis using an antibody against the ionized calcium-binding adapter molecule 1 (Iba1), which acts as an indicator for inflammation. The quantifications of Iba1-positive cells within the corpus callosum did not show a difference between groups. However, analysis of the white matter of cerebellum showed a significant increase in the occurrence of microglia in cKO mice as compared to control (**Figure 3.2.10a**). To further investigate inflammation, I stained the aforementioned brain sections with an antibody against macrophage antigen 3 (Mac3), marker for reactivated microglia. The number of activated microglia resulted in a slight increase in the corpus callosum and white matter of cerebellum of *Cnp1^{Cre/+};Fbxo7^{fl/fl}* mice (**Figure 3.2.10b**). In addition, I examined whether loss of *Fbxo7* leads to an increase in astrogliosis, since astrocytes extensively interact with microglia during an inflammatory response. Therefore, I immunostained brain sections with an antibody against glial fibrillary acidic protein (GFAP), a marker for astrocytes. The analysis showed a significant increase in GFAP signal in the white matter of cerebellum of *Cnp1^{Cre/+};Fbxo7^{fl/fl}* mice, but no difference in GFAP levels within the corpus callosum of all three groups (**Figure 3.2.10c**). To examine the inflammatory response upon *Fbxo7* deletion on long-traveling axons of the CNS, I further performed immunohistological staining on cross-sections of spinal cord from 3-months-old *Fbxo7^{fl/fl}*, *Cnp1^{Cre/+}* and *Cnp1^{Cre/+};Fbxo7^{fl/fl}* mice. The analysis of Iba1 stainings revealed a significant increase in microglia levels in *Cnp1^{Cre/+};Fbxo7^{fl/fl}* mice (**Figure 3.2.10d**). Moreover, GFAP stainings showed significantly more astrogliosis in cKO mice as compared to control (**Figure 3.2.10e**). Collectively, I found a significant increase in inflammation and astrogliosis predominantly in the white matter of the cerebellum of *Cnp1^{Cre/+};Fbxo7^{fl/fl}* mice. Further on *Cnp1^{Cre/+};Fbxo7^{fl/fl}* mice displayed significant inflammation and astrogliosis within the spinal cord.

3.2 Cellular characterization of *Cnp1^{Cre/+};Fbxo7^{fl/fl}* mice



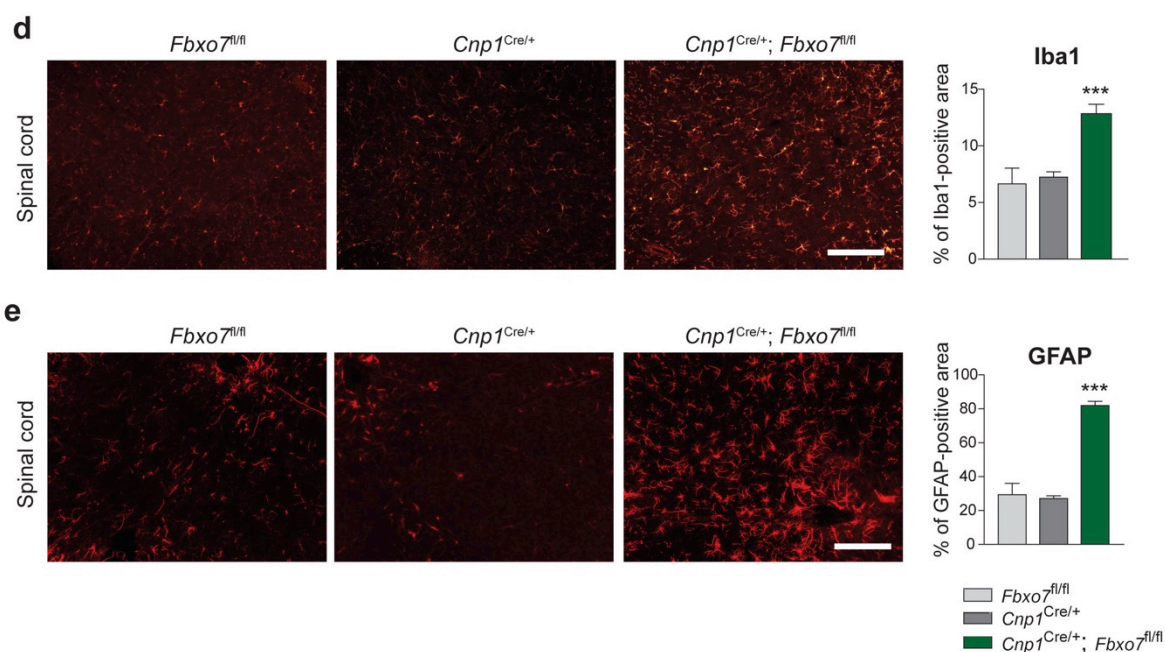
3.2 Cellular characterization of *Cnp1*^{Cre/+};*Fbxo7*^{fl/fl} mice

Figure 3.2.10 Increased inflammation in the white matter of cerebellum and spinal cord of *Cnp1*^{Cre/+};*Fbxo7*^{fl/fl} mice.

(a)-(c) Sagittal paraffin brain sections from 3-month-old *Fbxo7*^{fl/fl}, *Cnp1*^{Cre/+} and *Cnp1*^{Cre/+};*Fbxo7*^{fl/fl} mice were immunostained with (a) Iba1 (b) Mac3 and (c) GFAP antibodies. Three independent biological repeats per group and two technical repeats per animal were analyzed. Quantifications were performed within corpus callosum and white matter of cerebellum (one-way ANOVA, including Bonferroni post-test, *P < 0.05, **P < 0.01, mean ± s.e.m). Arrows indicate microglia, arrowheads show reactivated microglia and asterisk point at astrocytes. Scale bar = 50µm. (d) – (e) Representative images of spinal cord cross-sections from 3-month-old *Fbxo7*^{fl/fl}, *Cnp1*^{Cre/+} and *Cnp1*^{Cre/+};*Fbxo7*^{fl/fl} mice were immunostained with (d) Iba1 and (e) GFAP antibodies. Sections were taken from lumbar segment 1-3 of the spinal cord and three mice per condition, as well as three samples per mouse were analyzed (one-way ANOVA, including Bonferroni post-test, ***P < 0.001, mean ± s.e.m). The percentage of area stained by the respective antibody was analyzed, using a customized macro designed by Dr. Miso Mitkovski. Scale bar = 50µm.

3.2 Cellular characterization of *Cnp1*^{Cre/+};*Fbxo7*^{fl/fl} mice

Having determined that inflammation is significantly higher in cerebellar white matter of *Cnp1*^{Cre/+};*Fbxo7*^{fl/fl} mice, I further investigated inflammatory events by RT-PCR analysis. cDNA was synthesized from cerebellar tissue from 2-month-old *Fbxo7*^{fl/fl} and *Cnp1*^{Cre/+};*Fbxo7*^{fl/fl} mice and mRNA levels of different anti- and pro-inflammatory markers were tested. The analyses of anti-inflammatory markers including interleukin 10 (*IL-10*), interleukin 1 receptor antagonist (*IL-1ra*) and Interleukin 6 (*IL-6*), showed no significant but a trend of increased expression in *Cnp1*^{Cre/+};*Fbxo7*^{fl/fl} mice when compared to control mice (**Figure 3.2.11a**). Pro-inflammatory markers, such as tumor necrosis factor α (*Tnfa*), interleukin 1 β (*IL-1 β*), interferon γ -induced protein 10 (*Ip-10*) and monocyte chemoattractant protein 1 (*Mcp-1*) showed higher levels of expression in cKO mice, indicating an elevated inflammatory response in *Cnp1*^{Cre/+};*Fbxo7*^{fl/fl} mice. However of those pro-inflammatory markers only *Ip-10* was significantly increased (**Figure 3.2.11b**).

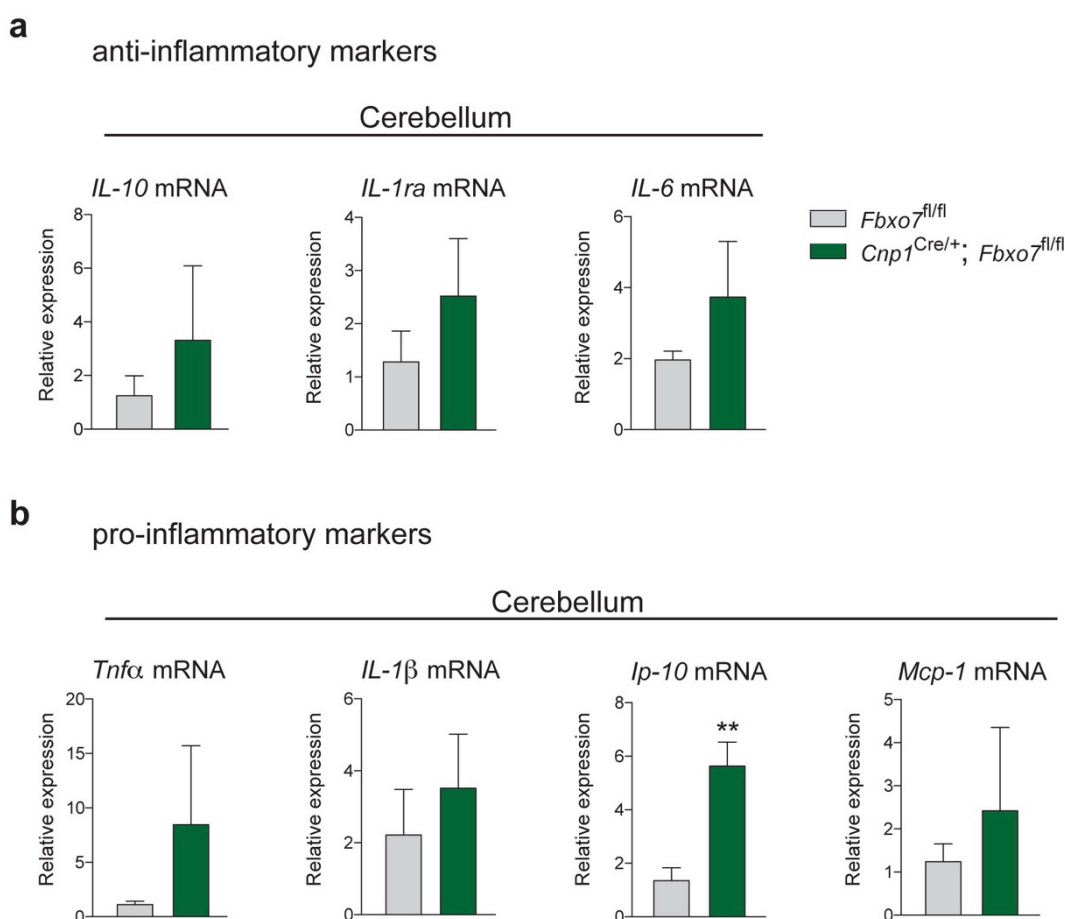


Figure 3.2.11 Levels of inflammatory markers show a trend of elevation in the cerebellum of *Cnp1*^{Cre/+};*Fbxo7*^{fl/fl} mice.

(a)-(b) RT-PCR analysis of RNA isolated from cerebella of 2-month-old *Fbxo7*^{fl/fl} and *Cnp1*^{Cre/+};*Fbxo7*^{fl/fl} mice. Primers were used for **(a)** anti-inflammatory markers including interleukin 10 (*IL-10*), interleukin 1 receptor antagonist (*IL-1ra*), Interleukin 6 (*IL-6*) and **(b)** pro-inflammatory markers including tumor necrosis factor α (*Tnfa*), interleukin 1 β (*IL-1 β*), interferon γ -induced protein 10 (*Ip-10*) and monocyte chemo attractant protein 1 (*Mcp-1*). Four independent animals per genotype were analyzed and three replicates per animal were included (unpaired t-test, **P < 0.01, mean \pm s.e.m).

3.2 Cellular characterization of *Cnp1*^{Cre/+};*Fbxo7*^{fl/fl} mice

To assess inflammation in the PNS of *Cnp1*^{Cre/+};*Fbxo7*^{fl/fl} mice, I subjected longitudinal sections of sciatic nerve from 3-month-old *Fbxo7*^{fl/fl}, *Cnp1*^{Cre/+} and *Cnp1*^{Cre/+};*Fbxo7*^{fl/fl} mice to immunohistochemical analysis using an antibody against Iba1 and GFAP. I found a significant increase in both Iba1-positive and GFAP-positive cells in cKO mice as compared to control (**Figure 3.2.12a,b**). Screening at a higher resolution for signs of inflammation, I analyzed electron microscopic images from sciatic nerve cross-sections of *Cnp1*^{Cre/+} and *Cnp1*^{Cre/+};*Fbxo7*^{fl/fl} mice. Interestingly, *Cnp1*^{Cre/+};*Fbxo7*^{fl/fl} mice harbored a striking number of macrophages engulfing and digesting dead myelinated axons, whereas macrophages were absent in control samples. Macrophages can be characterized by their thin, long processes, so-called pseudopodia, which they extend to engulf cellular debris, designated for phagocytosis and degradation. Additionally, large cytoplasmic granules are a feature of macrophages. These typical signs of macrophages I observed in great abundance in almost all of the 40 electron microscopic images of cKO mice, but not in the 40 images of section of control sciatic nerve (**Figure 3.2.12c**). The data illustrate the increased infiltration of the sciatic nerve by macrophages and underscores a strong inflammatory response in *Cnp1*^{Cre/+};*Fbxo7*^{fl/fl} mice upon *Fbxo7* deletion in the PNS.

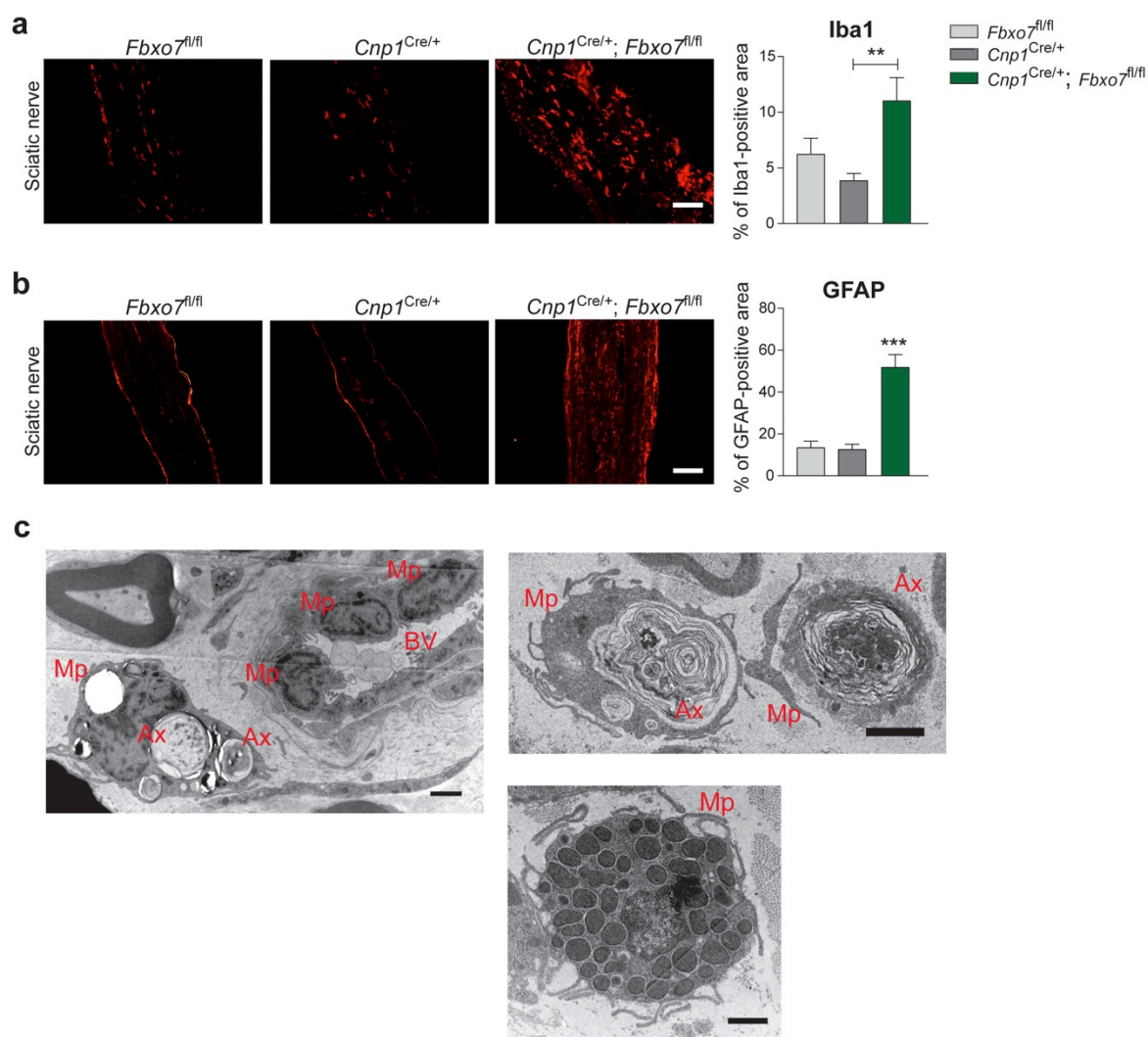
3.2 Cellular characterization of *Cnp1*^{Cre/+};*Fbxo7*^{fl/fl} mice

Figure 3.2.12 Increased inflammatory response in sciatic nerve of *Cnp1*^{Cre/+};*Fbxo7*^{fl/fl} mice.

(a)-(b) Longitudinal cryo-section from sciatic nerves of 3-month-old *Fbxo7*^{fl/fl}, *Cnp1*^{Cre/+} and *Cnp1*^{Cre/+};*Fbxo7*^{fl/fl} mice were subjected to immunohistochemistry using an antibody against (a) Iba1 or (b) GFAP. Three independent mice per genotype and three samples per mouse were analyzed (one-way ANOVA, including Bonferroni post-test, **P < 0.01, ***P < 0.001, mean ± s.e.m). The images were analyzed using a customized macro designed by Dr. Miso Mitkovski. Scale bar = 100µm. (c) Representative images of electron microscopic cross-sections from sciatic nerve of 3-month-old *Cnp1*^{Cre/+};*Fbxo7*^{fl/fl} mice. Images illustrate increased infiltration of sciatic nerve by macrophages engulfing dead, myelinated axons and migrating in from blood vessels. Mp = macrophage, Ax = axon, BV = blood vessel. Scale bar = 1µm.

3.3 Molecular characterization of *Cnp1*^{Cre/+};*Fbxo7*^{fl/fl} mice

Owing to its function as E3 ubiquitin ligase, FBXO7 interacts with different proteins and thus affects different molecular pathways. Previous studies have shown that FBXO7 interacts with p27, cyclin D/CDK6 complex and HURP, proteins which all are linked to cell cycle regulation (Hsu et al., 2004; Laman et al., 2005). Further on, FBXO7 was shown to interact with parkin and PINK, which both are essential for the mitochondrial quality control (Burchell et al., 2013). In our lab, Dr. David Brockelt identified FBXO7 to be a proteasome-associated protein, that binds to and ubiquitinates the proteasome subunit PSMA2 – a novel interaction partner. My colleagues demonstrated the vital role of FBXO7 in neurons and its regulatory function in proteasome assembly (Vingill et al., 2016). In the following experiments, I investigated the molecular changes in myelinating cells upon *Fbxo7* deletion and examined the proteasomal activity in *Fbxo7*-depleted Schwann cells.

3.3.1 *Fbxo7* deletion leads to an up-regulation of stress sensors and down-regulation of cytoskeletal proteins in CNS myelin

Myelinating cells not only insulate axons for fast and saltatory propagation of action potentials, they are also essential for the metabolic and trophic support of axons, ensuring their integrity and long term survival (Nave, 2010b). Hence, a balanced protein homeostasis within myelinating cells is crucial for the axon-glia interaction. To investigate how *Fbxo7* deletion affects the protein homeostasis in myelinating cells and support of axons, we subjected purified myelin isolated from brains of 3-month-old *Cnp1*^{Cre/+} and *Cnp1*^{Cre/+};*Fbxo7*^{fl/fl} mice to quantitative mass spectrometry analyses. Myelin purification from the CNS was performed by Ramona Jung and mass spectrometry analyses were done in collaboration with Dr. Olaf Jahn. The analysis identified 563 candidates, which were sorted according to a log₂ ratio of *Cnp1*^{Cre/+};*Fbxo7*^{fl/fl} values divided by *Cnp1*^{Cre/+} values. Among the proteins, those with 25% higher or lower expression levels as compared to control were grouped and selected candidates were analyzed. The up-regulated proteins of CNS myelin included a range of proteins that were associated with the cellular response to endogenous stimuli, such as detoxification processes, regulation of apoptosis, cellular signaling cascades and CNS development processes (**Figure 3.3.1a**). The majority of down-regulated proteins in CNS myelin were associated with cytoskeletal arrangement and mitochondrial function (**Figure 3.3.1b**). These results indicate that loss of *Fbxo7* from oligodendrocytes triggers a cellular stress response and

3.3 Molecular characterization of *Cnp1^{Cre/+};Fbxo7^{fl/fl}* mice

induces endogenous processes such as detoxification. Moreover, *Fbxo7* deletion affects the stability of the cytoskeleton and the mitochondrial function.

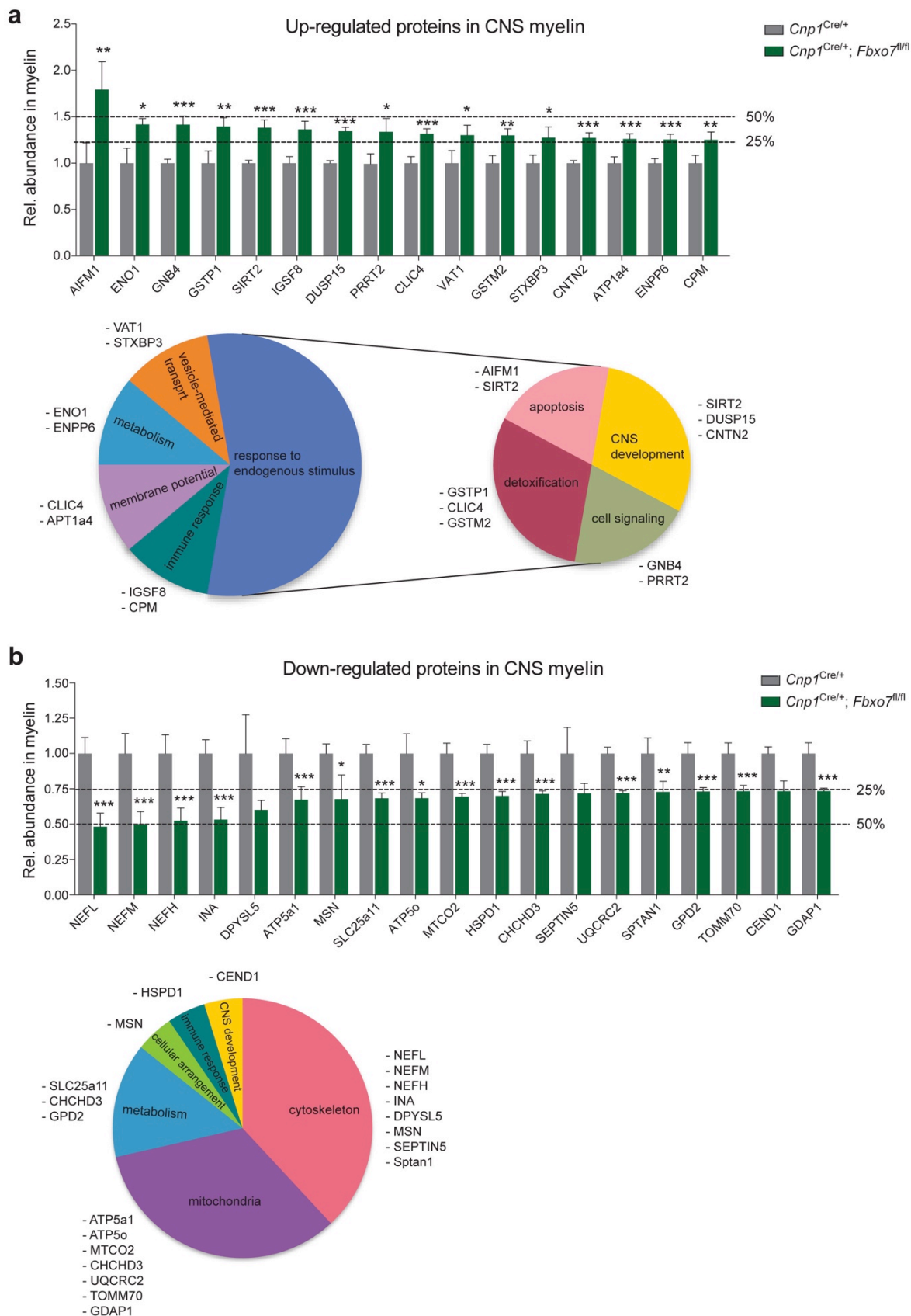


Figure 3.3.1 Up- and down-regulated proteins in CNS myelin upon deletion of *Fbxo7*.

3.3 Molecular characterization of *Cnp1*^{Cre/+};*Fbxo7*^{fl/fl} mice

(a)-(b) Purified myelin from 3-month-old *Cnp1*^{Cre/+} and *Cnp1*^{Cre/+};*Fbxo7*^{fl/fl} brains was analyzed by quantitative mass spectrometry. The mean of five mice per genotype and two repeats per animal was analyzed using the log₂ cKO/control ratio. *Cnp1*^{Cre/+};*Fbxo7*^{fl/fl} values were normalized to control (unpaired t-test, *P < 0.05, **P < 0.01, ***P < 0.001, mean ± s.e.m.). Shown are the 25% of **(a)** up-regulated proteins [AIFM1: Apoptosis-inducing factor 1; ENO1: Enolase 1; GNB4: Guanine nucleotide-binding protein subunit beta 4; GSTP1: Glutathione S-transferase pi 1; SIRT2: NAD-dependent protein deacetylase sirtuin-2; IGSF8: Immunoglobulin superfamily member 8; DUSP15: Dual specificity protein phosphatase 15; PRRT2: Proline-rich transmembrane protein 2; CLIC4: Chloride intracellular channel protein 4; VAT1: Synaptic vesicle membrane protein VAT-1 homolog; GSTM2: Glutathione S-transferase mu; STXBP3: Syntaxin-binding protein 3; CNTN2: Contactin 2; ATP1A4: Sodium/potassium-transporting ATPase subunit alpha 4; ENPP6: Ectonucleotide; pyrophosphatase 6; CPM: Carboxypeptidase M] and **(b)** down-regulated proteins [NEFL: Neurofilament light; NEFM: Neurofilament medium; NEFH: Neurofilament heavy; INA: Alpha-internexin; DPYSL5: Dihydropyrimidinase-related protein 5; ATP5A1: ATP synthase subunit alpha; MSN: Moesin; SLC25A11: Mitochondrial 2-oxoglutarate/malate carrier protein; ATP5O: ATP synthase subunit O; MTCO2: Cytochrome c oxidase subunit 2; HSPD1: 60 kDa heat shock protein; CHCHD3: MICOS complex subunit Mic19; SEPTIN5: Septin 5; UQCRC2: Cytochrome b-c1 complex subunit 2; SPTAN1: Spectrin alpha chain; GPD2: Glycerol-3-phosphate dehydrogenase; TOMM70: Mitochondrial import receptor subunit TOM70; CEND1: Cell cycle exit and neuronal differentiation protein 1; GDAP1: Ganglioside-induced differentiation-associated protein 1] of CNS myelin from *Cnp1*^{Cre/+};*Fbxo7*^{fl/fl} brains as compared to control. Pie chart displays the biological function of selected candidates, which was gathered using the Toppgene database. Quantitative mass spectrometry was conducted by Dr. Olaf Jahn

In order to validate the results from mass spectrometry, I performed immunohistochemical stainings on spinal cord sections of 3-month-old *Cnp1*^{Cre/+};*Fbxo7*^{fl/+} and *Cnp1*^{Cre/+};*Fbxo7*^{fl/fl} mice. The quantitative mass spectrometry analyses identified a range of proteins involved in the detoxification pathway. I decided to focus on glutathione S-transferase π 1 (GSTπ1), whose levels were increase. Importantly, GSTπ1 is specifically expressed in oligodendrocytes. I carried out immunohistochemical analyses on spinal cord sections of 3-month-old *Fbxo7*^{fl/fl}, *Cnp1*^{Cre/+} and *Cnp1*^{Cre/+};*Fbxo7*^{fl/fl} mice and found a significant increase in GSTπ1 signal in *Cnp1*^{Cre/+};*Fbxo7*^{fl/fl} mice as compared to control, verifying the up-regulated stress response in cKO mice (**Figure 3.3.2a**). Further on, I subjected brain lysates from *Cnp1*^{Cre/+};*Fbxo7*^{fl/+} and *Cnp1*^{Cre/+};*Fbxo7*^{fl/fl} mice to immunoblotting using the GSTπ1 antibody. The lysates of developing cKO mouse brains indicated a stronger signal for GSTπ1 at all ages examined (**Figure 3.3.2b**). With these results I showed that loss of *Fbxo7* from oligodendrocytes induces an up-regulation of the stress sensor GSTπ1.

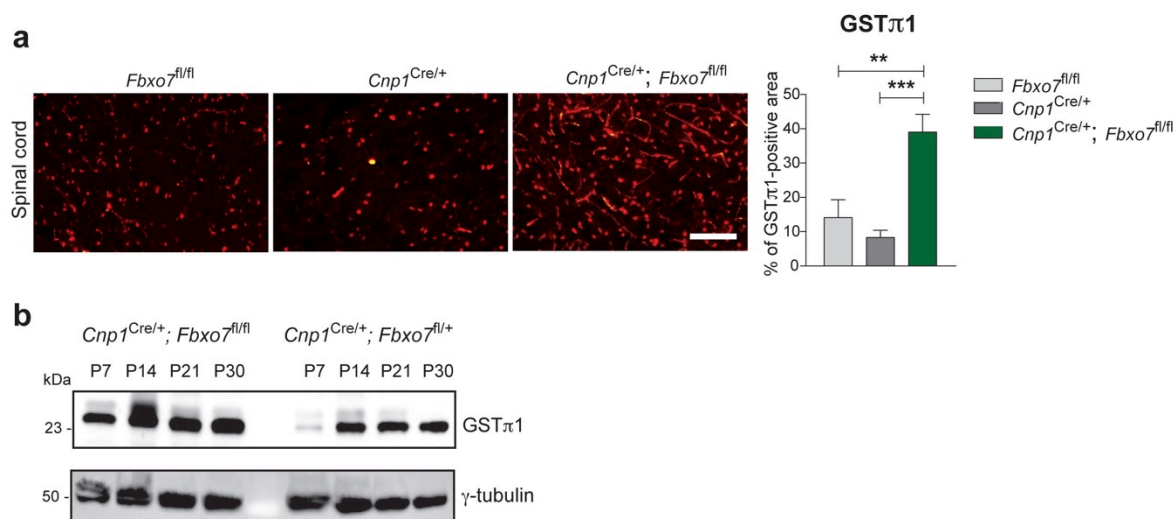
3.3 Molecular characterization of *Cnp1*^{Cre/+};*Fbxo7*^{fl/fl} mice

Figure 3.3.2 Increased GSTπ1 levels in the CNS due to *Fbxo7* deletion.

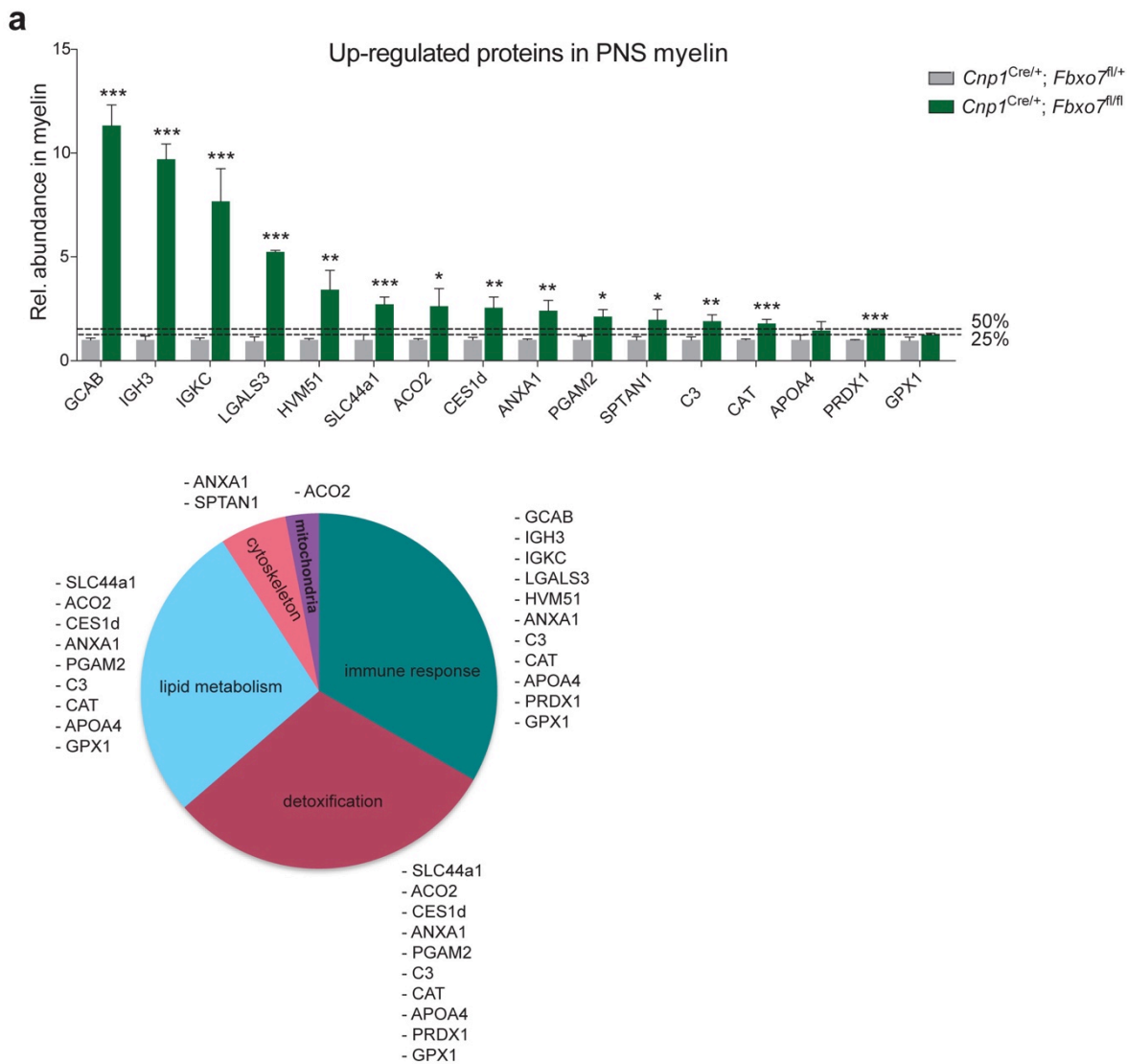
(a) cross-sections of spinal cord from 3-month-old *Fbxo7*^{fl/fl}, *Cnp1*^{Cre/+} and *Cnp1*^{Cre/+};*Fbxo7*^{fl/fl} mice were immunostained with a GSTπ1 antibody. Sections were taken from lumbar segment 1-3 of the spinal cord and three mice per condition, as well as three samples per mouse were analyzed (one-way ANOVA, **P < 0.01, ***P < 0.001, mean ± s.e.m). The percentage of area stained by GSTπ1 antibody was analyzed using a customized macro designed by Dr. Miso Mitkovski. Scale bar = 1μm. (b) Brain lysates from postnatal day (P) 7, P14, P21 and P30 of *Cnp1*^{Cre/+};*Fbxo7*^{fl/+} and *Cnp1*^{Cre/+};*Fbxo7*^{fl/fl} mice were immunoblotted with GSTπ1 and γ-tubulin antibodies, while γ-tubulin served as a loading control. (Sample was run on the same gradient gel as described in 3.3.4).

3.3.2 Loss of *Fbxo7* causes an immune response and down-regulation of cytoskeleton proteins in PNS myelin

To assess any changes in protein homeostasis in PNS myelin upon *Fbxo7* deletion, myelin was purified from sciatic nerves. Purification of myelin from sciatic nerve isolated from 3-month-old *Cnp1*^{Cre/+};*Fbxo7*^{fl/+} and *Cnp1*^{Cre/+};*Fbxo7*^{fl/fl} mice was performed with the help of Katja Lüders. Myelin was subjected to quantitative mass spectrometry analyses, performed by Dr. Olaf Jahn. 404 proteins were identified by quantitative mass spectrometry and further sorted by the log₂ ratio of *Cnp1*^{Cre/+};*Fbxo7*^{fl/fl} values divided by *Cnp1*^{Cre/+};*Fbxo7*^{fl/+} values. Among these candidates, the top 25% of up- and down-regulated proteins were grouped together and selected candidates were analyzed. The analysis of up-regulated proteins in PNS myelin indicated a big cluster of proteins that was part of the immune response. Further on, a large group of proteins were associated to detoxification processes and the lipid metabolism (**Figure 3.3.3a**). Among the down-regulated proteins, the majority of candidates were linked to the cytoskeleton. In addition, large clusters of mitochondrial proteins, proteins associated to ubiquitination and the

3.3 Molecular characterization of *Cnp1*^{Cre/+};*Fbxo7*^{fl/fl} mice

metabolism were also down regulated (**Figure 3.3.3b**). Taken together these results show that loss of *Fbxo7* from Schwann cells induces an inflammatory response and increases detoxification processes. Additionally, deletion of *Fbxo7* affects the stability of the cytoskeleton, mitochondrial integrity and the UPS.



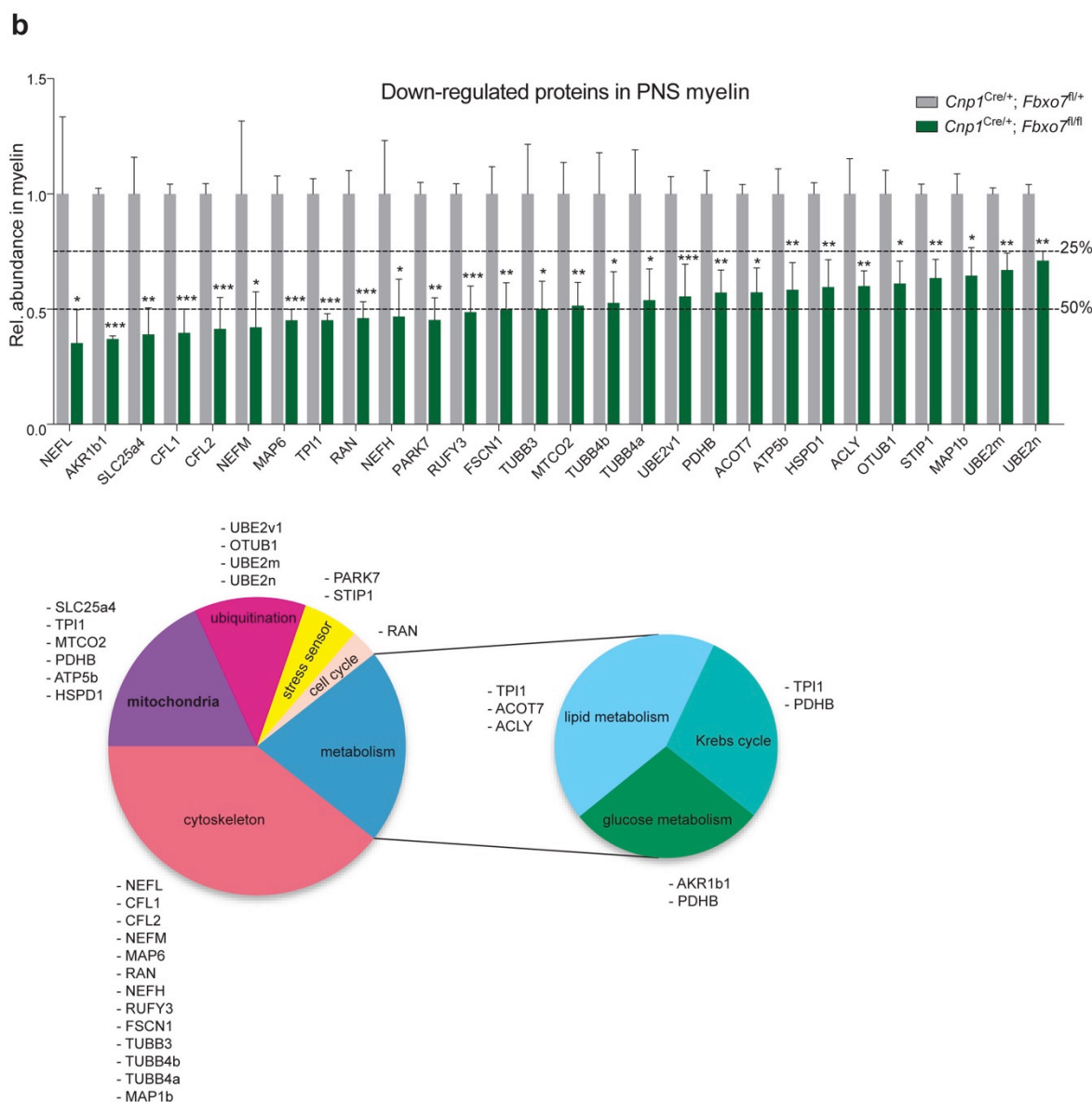
3.3 Molecular characterization of *Cnp1*^{Cre/+};*Fbxo7*^{fl/fl} mice

Figure 3.3.3 Up- and down-regulated proteins in PNS myelin upon *Fbxo7* deletion.

(a)-(b) Purified myelin from sciatic nerves of 3-month-old *Cnp1*^{Cre/+};*Fbxo7*^{fl/+} and *Cnp1*^{Cre/+};*Fbxo7*^{fl/fl} mice were analyzed by quantitative mass spectrometry. Nine pairs of sciatic nerve per genotype were pooled into 3 groups, each measured twice and the total mean analyzed using the log₂ cKO/control ratio. Values from *Cnp1*^{Cre/+};*Fbxo7*^{fl/fl} mice were normalized to control (unpaired t-test, *P < 0.05, **P < 0.01, ***P < 0.001, mean ± s.e.m.). From the identified proteins, the 25% of **(a)** up-regulated proteins [GCAB: Ig gamma 2A; IGH3: Ig gamma 2B; IGKC: Ig kappa; LGALS3: Galectin 3; HVM51: Ig heavy chain V; SLC44A1: Choline transporter-like protein 1; ACO2: Aconitate hydratase; CES1D: Carboxylesterase 1D; ANXA1: Annexin A1; PGAM2: Phosphoglycerate mutase 2; SPTAN1: Spectrin alpha chain; C3: Complement C3; CAT: Catalase; APOA4: Apolipoprotein A4; PRDX1: Peroxiredoxin 1; GPX1: Glutathione peroxidase 1] and **(b)** down-regulated proteins [NEFL: Neurofilament light; AKR1B1: Aldose reductase; SCL25A4: ADP/ATP translocase 1; CFL1: Cofilin 1; CFL2: Cofilin 2; NEFM: Neurofilament medium; MAP6: Microtubule-associated protein 6; TPI1: Triosephosphate isomerase; RAN: GTP-binding nuclear protein Ran; NEFH: Neurofilament heavy; PARK7: Protein deglycase DJ-1; RUFY3: Protein RUFY3; FSCN1: Fascin; TUBB3: Tubulin beta 3; MTCO2: Cytochrome c oxidase subunit; TUBB4B: Tubulin beta 4B; TUBB4A: Tubulin beta 4A; UBE2V1: Ubiquitin-

3.3 Molecular characterization of *Cnp1*^{Cre/+};*Fbxo7*^{fl/fl} mice

conjugating enzyme E2 variant 1; PDHB: Pyruvate dehydrogenase E1 component subunit beta; ACOT7: Cytosolic acyl coenzyme A thioester hydrolase; ATP5B: ATP synthase subunit beta; HSPD1: 60 kDa heat shock protein; ACLY: ATP-citrate synthase; OTUB1: Ubiquitin thioesterase OTUB1; STIP1: Stress-induced-phosphoprotein; MAP1B: Microtubule-associated protein 1B; UBE2M: NEDD8-conjugating enzyme Ubc12; UBE2N: Ubiquitin-conjugating enzyme E2 N] in *Cnp1*^{Cre/+};*Fbxo7*^{fl/fl} myelin as compared to control were selected. Pie chart displays the biological function of selected candidates, which was gathered while using the Toppgene database. Quantitative mass spectrometry was conducted by Dr. Olaf Jahn.

Although the list of up-regulated myelin proteins from the PNS of *Cnp1*^{Cre/+};*Fbxo7*^{fl/fl} mice did not include GST π 1, as seen in CNS myelin, detoxification processes were still highly up-regulated. Therefore, I investigated if the stress marker GST π 1 undergoes any changes and performed an immunohistochemical analysis on sciatic nerve sections of 3-month-old *Fbxo7*^{fl/fl}, *Cnp1*^{Cre/+} and *Cnp1*^{Cre/+};*Fbxo7*^{fl/fl} mice using a GST π 1 antibody. The result showed significant increase in GST π 1 signals in sections of *Cnp1*^{Cre/+};*Fbxo7*^{fl/fl} sciatic nerve as compared to control sciatic nerve (**Figure 3.3.4**).

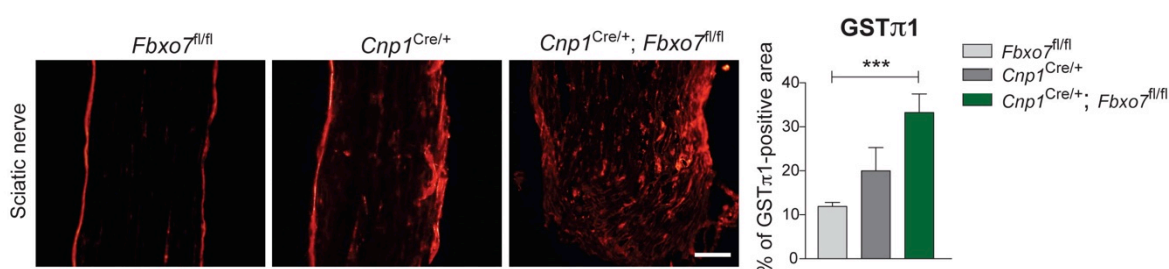


Figure 3.3.4 Increased GST π 1 signal in sciatic nerve isolated from *Cnp1*^{Cre/+};*Fbxo7*^{fl/fl} mice.

Immunohistochemical analyses were performed on longitudinal cryo-section of sciatic nerves from 3-month-old *Fbxo7*^{fl/fl}, *Cnp1*^{Cre/+} and *Cnp1*^{Cre/+};*Fbxo7*^{fl/fl} mice using a GST π 1 antibody. Three independent mice per genotype and three samples per mouse were analyzed (one-way ANOVA, Bonferroni post-test, ****P* < 0.001, mean \pm s.e.m). The images were analyzed using a customized macro designed by Dr. Miso Mitkovski. Scale bar = 100 μ m.

3.3.3 Increased myelin maintenance in the CNS and signs of peripheral neuropathy in *Cnp1*^{Cre/+};*Fbxo7*^{fl/fl} mice

The quantitative mass spectrometry data were further analyzed with regard to changes in structural myelin proteins and candidates that are closely associated with myelination. Within purified myelin from the CNS, I found that proteins linked to myelin maintenance and stabilization were up-regulated in *Cnp1*^{Cre/+};*Fbxo7*^{fl/fl} mice as compared to control. However, structural and myelin membrane specific proteins, including PLP, CNP, MBP

3.3 Molecular characterization of *Cnp1*^{Cre/+};*Fbxo7*^{fl/fl} mice

and MAG did not show any alterations upon *Fbxo7* deletion (**Figure 3.3.5a**). Similar to myelin proteins of the CNS, the analysis of PNS myelin did not show any change in myelin membrane-specific proteins (CNP, PLP, MAG, PMP2, MPZ and MBP). Interestingly, the trophic factor CNTF, which is important for axonal support, as well as proteins associated with peripheral neuropathy and cytoskeleton motility were significantly reduced in PNS myelin of *Cnp1*^{Cre/+};*Fbxo7*^{fl/fl} mice (**Figure 3.3.5b**). Concluding from these results, I showed that loss of *Fbxo7* from myelinating cells does not affect structural myelin proteins, which further supports my previous results. However, deletion of *Fbxo7* induces an increase in myelin maintenance in oligodendrocytes, whereas in Schwann cells loss of *Fbxo7* decreases the supportive function of myelin and affects proteins, which are associated with peripheral neuropathy.

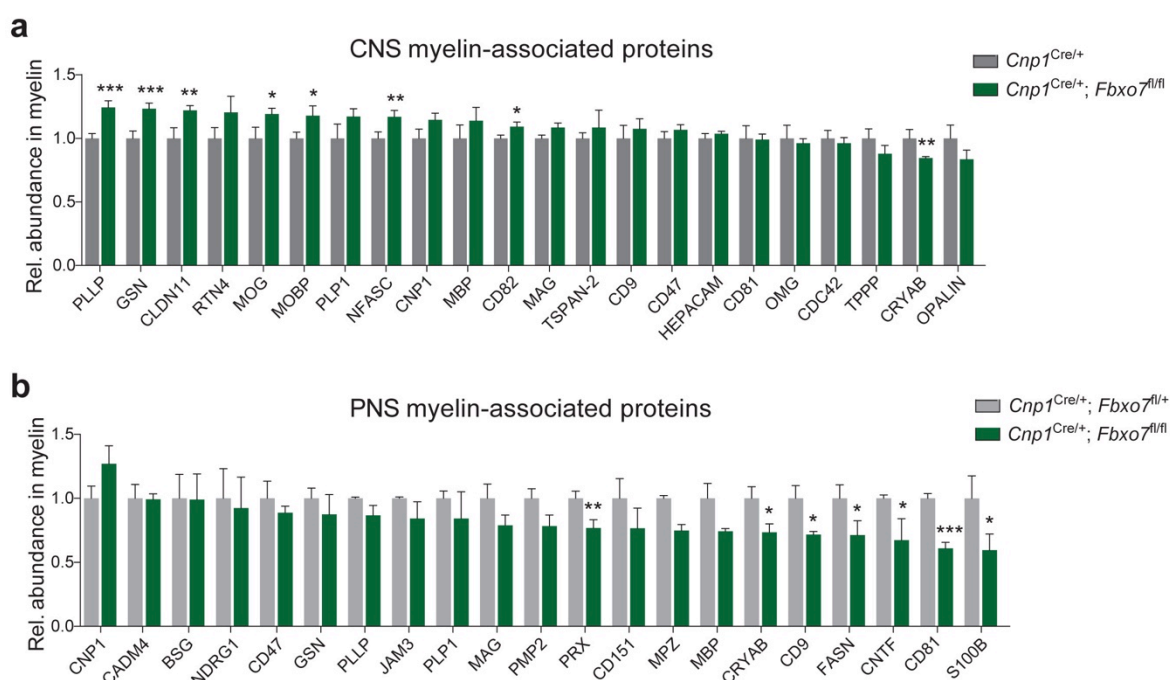


Figure 3.3.5 Loss of *Fbxo7* induces an increase in CNS myelin maintenance and affects proteins, which are associated with peripheral neuropathy in the PNS.

(a) Purified myelin from brains of 3-month-old *Cnp1*^{Cre/+} and *Cnp1*^{Cre/+};*Fbxo7*^{fl/fl} mice were subjected to quantitative mass spectrometry. The mean of five mice per genotype and two repeats per animal was analyzed using the log₂ cKO/control ratio. *Cnp1*^{Cre/+};*Fbxo7*^{fl/fl} values were normalized to control (unpaired t-test, *P < 0.05, **P < 0.01, ***P < 0.001, mean ± s.e.m.) [PLLP: Plasmolipin; GSN: Gelsolin; CLDN11: Claudin 11; RTN4: Reticulon 4; MOG: Myelin-oligodendrocyte glycoprotein; MOBP: Myelin-associated oligodendrocyte basic protein; PLP1: Proteolipid protein; NFASC: Neurofascin; CNP1: 2',3'-cyclic-nucleotide 3'-phosphodiesterase; MBP: Myelin basic protein; CD82: CD82 antigen; MAG: Myelin-associated glycoprotein; TSPAN2: Tetraspanin 2; CD9: CD9 antigen; CD47: Leukocyte surface antigen CD47; HEPACAM: Hepatocyte cell adhesion molecule; CD81: CD81 antigen; OMG: Oligodendrocyte-myelin glycoprotein; CDC42: Cell division control protein 42 homolog; TPPP: Tubulin polymerization-promoting protein; CRYAB: Alpha-crystallin B chain; OPALIN: Opalin]. **(b)** Purified myelin from sciatic nerves of 3-month-old

3.3 Molecular characterization of *Cnp1*^{Cre/+};*Fbxo7*^{fl/fl} mice

Cnp1^{Cre/+};*Fbxo7*^{fl/+} and *Cnp1*^{Cre/+};*Fbxo7*^{fl/fl} mice were analyzed by mass spectrometry. Nine pairs of sciatic nerve per genotype were pooled into 3 groups, each measured twice and the total mean analyzed using the log₂ cKO/control ratio (unpaired t-test, *P < 0.05, **P < 0.01, ***P < 0.001, mean ± s.e.m.) [CNP1: 2',3'-cyclic-nucleotide 3'-phosphodiesterase; CADM4: Cell adhesion molecule 4; BSG: Basigin; NDRG1: Protein NDRG1; CD47: Leukocyte surface antigen CD47; GSN: Gelsolin; PLLP: Plasmolipin; JAM3: Junctional adhesion molecule C; PLP1: Proteolipid protein; MAG: Myelin-associated glycoprotein; PMP2: Myelin P2 protein; PRX: Periaxin; CD151: CD151 antigen; MPZ: Myelin protein P0; MBP: Myelin basic protein; CRYAB: Alpha-crystallin B chain; CD9: CD9 antigen; FASN: Fatty acid synthase; CNTF: Ciliary neurotrophic factor; CD81: CD81 antigen; S100B: Protein S100 B]. Mass spectrometry was conducted by Dr. Olaf Jahn and analyses of data were supported by PD Dr. Hauke Werner.

3.3.4 *Cnp1*^{Cre/+};*Fbxo7*^{fl/fl} mice show unaltered development of oligodendrocytes regarding NG2 and CNP levels

Fbxo7 is highly expressed in oligodendrocyte precursor cells (OPC's) and newly forming oligodendrocytes (Zhang et al., 2014). Hence, we speculated that loss of *Fbxo7* might impact myelination at an early state of development. To test this hypothesis, I subjected brain lysates from *Cnp1*^{Cre/+};*Fbxo7*^{fl/+} and *Cnp1*^{Cre/+};*Fbxo7*^{fl/fl} mice of postnatal (P) day 7, 14, 21 and 30 to immunoblotting analysis using an antibody against the oligodendrocyte precursor marker (NG2). Here, I observed no difference between *Cnp1*^{Cre/+};*Fbxo7*^{fl/fl} mice and control. As expected, the levels of NG2 declined with age as OPCs differentiate into newly forming oligodendrocytes. Further on, I applied an antibody against 2',3'-cyclic-nucleotide 3'-phosphodiesterase (CNP), which is a marker for myelinating oligodendrocytes. As anticipated, both cKO and control samples showed that the levels increased with age. In addition the samples were analyzed with an antibody against FBXO7. FBXO7 levels showed an increase in control mice, but within the *Cnp1*^{Cre/+};*Fbxo7*^{fl/fl} samples the intensity of FBXO7 was only elevated until P21 and showed an obvious reduction at P30. This verifies the proper function of our transgene in the cKO mouse line: the activity of the *Cnp1* promoter is highly increased at P30, at the same time as the level of FBXO7 decreases. An immunoblot with γ -tubulin served as loading control (**Figure 3.3.6**).

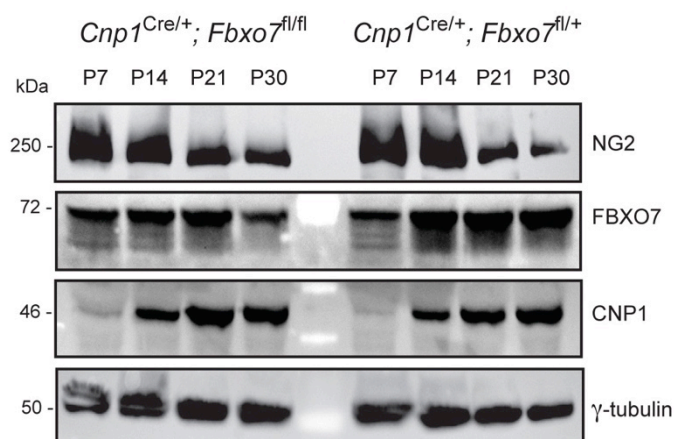
3.3 Molecular characterization of *Cnp1*^{Cre/+};*Fbxo7*^{fl/fl} mice

Figure 3.3.6 *Fbxo7* deletion does not influence the development of oligodendrocytes.

Brain lysates from P7, P14, P21 and P30 of *Cnp1*^{Cre/+};*Fbxo7*^{fl/fl} and *Cnp1*^{Cre/+};*Fbxo7*^{fl/+} mice were immunoblotted with NG2, FBXO7, CNP1 or γ -tubulin antibodies. The latter served as a loading control. Western-blot analyses were repeated three times.

3.3.5 Knockdown of the E3-ubiquitin ligase FBXO7 decreases proteasome activity

The E3-ubiquitin ligase FBXO7 belongs to the multi-subunit SKP1-cullin1-FBXO7 (SCF)-complex and as such is part of the ubiquitin-proteasome-system (UPS). Ubiquitination of target substrates by FBXO7 can either lead to functional modifications or proteasomal degradation (Nelson et al., 2013). In a co-immunoprecipitation (Co-IP) assay I verified, that the F-box domain of FBXO7 is crucial for binding of SKP1, which binds to cullin1 and altogether form the SCF-complex (Cardozo and Pagano, 2004). For this Co-IP, I transfected HEK cells with an empty vector p3xFLAG-CMV10, a plasmid encoding for Flag-tagged full-length *Fbxo7* (*Fbxo7*-wt) or a plasmid encoding for a deletion mutant of *Fbxo7* lacking the F-box domain (*Fbxo7*- Δ fbox) together with the myc-*Skp1* plasmid. The lysates were subjected to immunoprecipitation using a myc antibody, which pulled down SKP1 and the attached complex. Afterwards, the precipitates were immunoblotted with a Flag antibody, visualizing the FBXO7 protein. Furthermore, I carried out an immunoprecipitation using the Flag antibody, followed by immunoblotting with a cullin1 antibody. The results show that in absence of the F-box domain, FBXO7 does not interact with SKP1 or cullin1 and therefore will not form an SCF-complex (**Figure 3.3.7**).

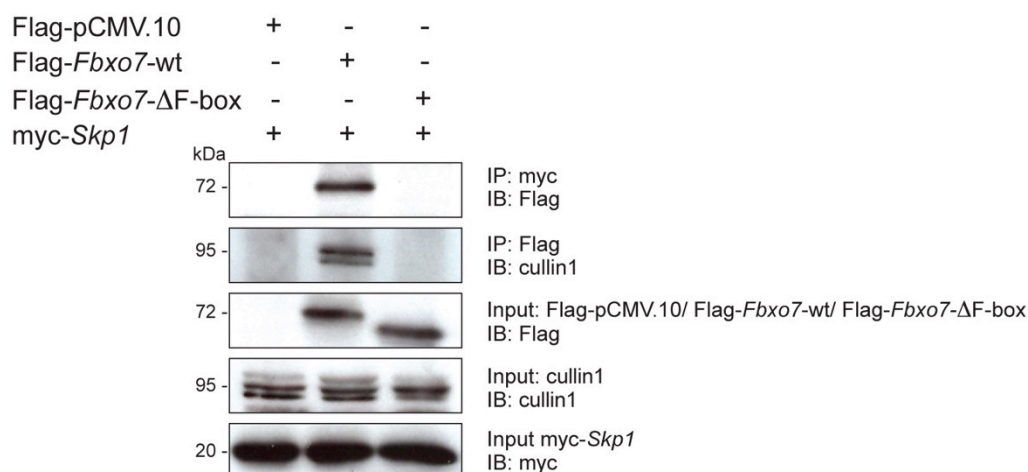
3.3 Molecular characterization of *Cnp1Cre/+;Fbxo7^{fl/fl}* mice

Figure 3.3.7 The FBXO7 F-box domain is crucial for the SCF-complex formation.

HEK293T cells were co-transfected with an empty vector, flag-tagged *Fbxo7*-wt or flag-tagged *Fbxo7*-ΔF-box and together with myc-tagged *Skp1*. The cell lysates were subjected to co-immunoprecipitation analysis using a myc antibody, followed by immunoblotting with a Flag antibody.

In our lab, Dr. David Brockelt identified the proteasomal subunit PSMA2 as direct and novel interaction partner of FBXO7 and showed that the ubiquitination via K-63-linkage of PSMA2 by FBXO7 induces a functional modification. This modification of PSMA2 by FBXO7 was shown to be essential for a proper proteasomal assembly and function (Brockelt, 2015). Brain lysates from FBXO7 knockout mice revealed a significant reduction in proteasome activity as compared to control littermates. Hence, I investigated the importance of FBXO7 for the proteasome function in myelinating cells and performed a proteasome activity assay in MSC80 Schwann cells. The aneuploid MSC80 Schwann cell line used in this study was established from primary mouse Schwann cell cultures (Boutry et al., 1992). I transfected MSC80 with the functional FBXO7 shRNA 1, the non-functional FBXO7 shRNA 4 and empty vector as control. In addition, I used as positive control a functional PSMA2 shRNA 7, which targets the proteasomal subunit PSMA2 and as negative control the non-functional PSMA2 shRNA 1. In addition, the cells were co-transfected with GFP to facilitate the sorting of the transfected cells by Fluorescence-Activated Cell Sorting (FACS). This step was necessary, since the transfection efficiency in MSC80 cells only yielded approximately 40%. Lysates of the transfected and sorted MSC80 cells were subjected to a proteasome activity assay, which measures the chymotrypsin-like activity of the proteasome using a fluorogenic substrate. The proteasome activity was measured, while quantifying the fluorescent signal. The specific readout of this assay was previously tested using the proteasome inhibitor lactacystin (Vingill et al., 2016). The result revealed a 31% reduction in proteasome activity in

FBXO7-depleted cells. Control PSMA2 shRNA cells revealed a 39% reduction in activity (**Figure 3.3.8a**). To validate the knockdown of FBXO7 and PSMA2, I performed a western-blot analysis of lysates from transfected and sorted MSC80 cells and immunoblotted against FBXO7, PSMA2 and γ -tubulin as loading control. Indeed, the functional shRNAs effectively knocked down FBXO7 and PSMA2, whereas non-functional shRNAs did not alter the protein levels of FBXO7 and PSMA2 (**Figure 3.3.8b**). Hence, I demonstrated that knockdown of FBXO7 in Schwann cells induces an impairment of proteasome activity.

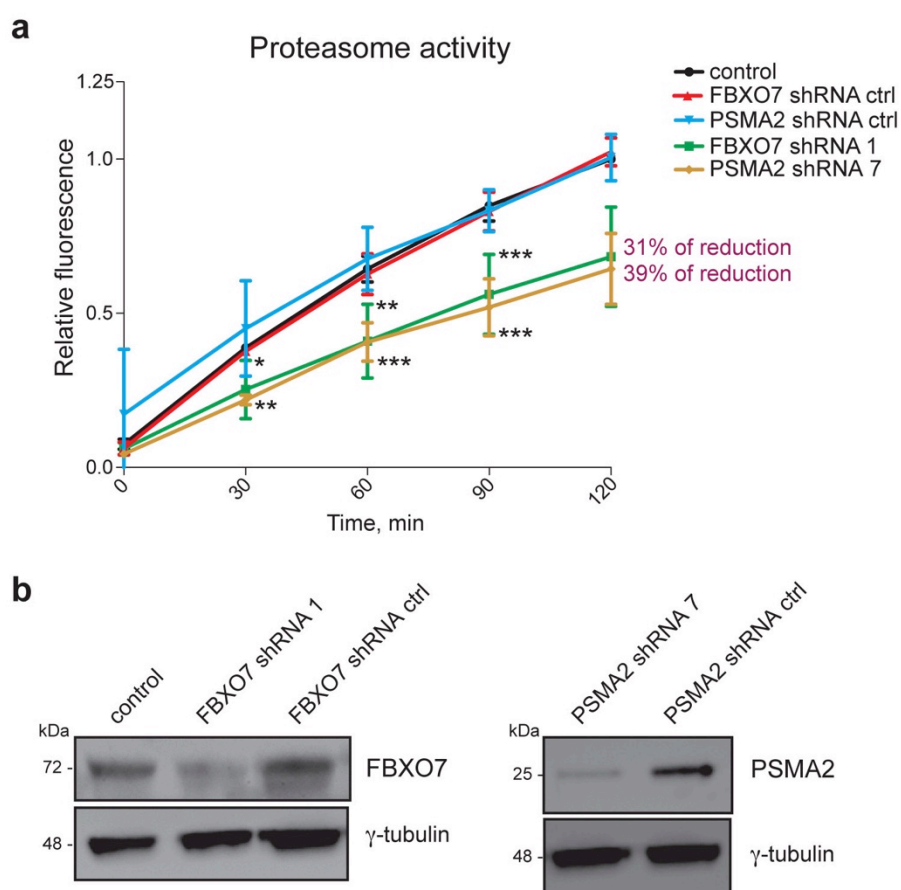


Figure 3.3.8 Knockdown of FBXO7 in Schwann cells leads to decreased proteasome activity

(a) MSC80 cells were transfected with a functional FBXO7 shRNA 1 and a functional PSMA2 shRNA 7. Transfections with a non-functional FBXO7 shRNA 4, non-functional PSMA2 shRNA 1 and empty vector served as control. Cell lysates were sorted and subjected to a proteasome activity assay (two-way ANOVA, * $P < 0.05$, ** $P < 0.01$, *** $P < 0.001$, mean \pm s.e.m). **(b)** Validation of shRNAs. Transfected MSC80 cell were lysed and a western-blot analysis was performed, while using antibodies against FBXO7, PSMA2 and γ -tubulin. The latter served as loading control.

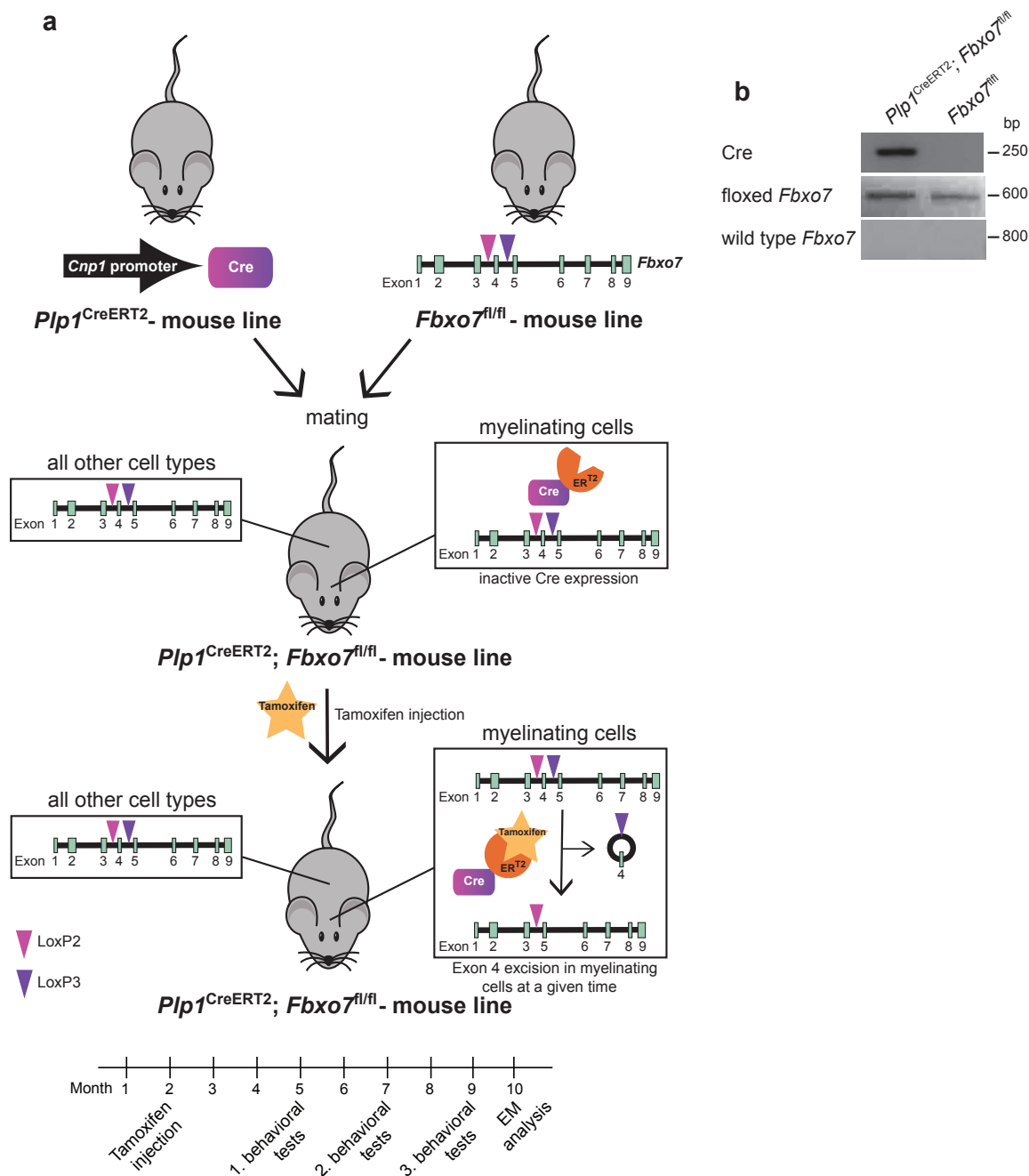
3.4 The post-developmental contribution of FBXO7 to the maintenance of the axon-glia interaction

With our *Cnp1^{Cre/+};Fbxo7^{fl/fl}* mouse line we showed that FBXO7 severely affects the axon-glia communication and that loss of *Fbxo7* in myelinating cells has a stronger impact on axon survival than on myelin stability. Since a previous publication has shown that *Fbxo7* is highly expressed during early stages of oligodendrocyte development, we were wondering if the impact of FBXO7 on the axon-glia interaction is only developmental based or whether FBXO7 also has a post-developmental contribution (Zhang et al., 2014). Hence, we generated a Tamoxifen-inducible *Pip1^{CreERT2/+}; Fbxo7^{fl/fl}* mouse line (cKO-Tam), in which *Fbxo7* was deleted from myelinating cells at a selected time point.

3.4.1 Generation of the *Pip1^{CreERT2/+};Fbxo7^{fl/fl}* mouse line

In collaboration with the department of Prof. Dr. Klaus-Armin Nave, we generated an inducible mouse line, in which *Fbxo7* was deleted from myelinating cells upon injection of Tamoxifen. Here, we bred the *Fbxo7^{fl/fl}* line (Vingill et al.) with the Tamoxifen-inducible *Pip1^{CreERT2/+}* mice (Leone et al., 2003). Tamoxifen, an agonist of the modified estrogen receptor (ER^{T2}), was injected at 2 month of age, when myelination was completed (**Figure 3.4.1a**). *Fbxo7^{fl/fl}* mice, injected with an equal amount of Tamoxifen, served as controls for *Pip1^{CreERT2/+}; Fbxo7^{fl/fl}* mice. Genotyping with primers for the Cre, floxed *Fbxo7* and wild type *Fbxo7* alleles ensured a correct breeding and were used to monitor the mouse line (**Figure 3.4.1b**).

3.4 The post-developmental contribution of FBOX7 to the maintenance of the axon-glia interaction



3.4.2 *Plp1*^{CreERT2/+}; *Fbxo7*^{fl/fl} mice show a moderate reduction of motor endurance and progressive muscle weakness

Plp1^{CreERT2/+}; *Fbxo7*^{fl/fl} mice did not display a strong phenotype and had a normal lifespan, comparable to those of control mice. To assess even mild changes in motor performance, I conducted an array of behavioral tests, in which I examined *Fbxo7*^{fl/fl} and *Plp1*^{CreERT2/+}; *Fbxo7*^{fl/fl} mice three, five and seven months after Tamoxifen injection. The analyses showed a stagnating bodyweight in *Plp1*^{CreERT2/+}; *Fbxo7*^{fl/fl} mice, which was significantly reduced at five and seven months post-Tamoxifen injected as compared to control (**Figure 3.4.2a**). Moreover, cKO-Tam mice scored significantly worse while performing a tail suspension test seven months post injection, indicating a progressive hind limb weakness (**Figure 3.4.2b**). In order to test the muscle strength of mice, an inverted grid test was performed and showed a decreased performance in *Plp1*^{CreERT2/+}; *Fbxo7*^{fl/fl} mice, when tested three months after injection. However the performance on an inverted grid did not progress at later time points (**Figure 3.4.2c**). Furthermore, muscle weakness was assessed with a wire hang test. Here, cKO-Tam mice showed decreased muscle strength as compared to control, when tested seven months after injection (**Figure 3.4.2d**). With the rotarod test, their motor endurance was analyzed and revealed a significant reduction in knockout mice as compared to control at all time points (**Figure 3.4.2e**). A pole test was carried out to determine motor coordination, showing no difference between both groups (**Figure 3.4.2f**). Motor coordination was further tested with a balance beam test. Here, cKO-Tam mice showed no difference in performance on the 6mm or 12mm beam compared to control mice at any time (**Figure 3.4.2g,h**). Aside from these motor tests, I further analyzed the sensory performance of mice and conducted a hotplate test. *Plp1*^{CreERT2/+}; *Fbxo7*^{fl/fl} mice showed signs of irritation a bit later than control mice, but did not differ significantly from control animals (**Figure 3.4.2i**). Anxiety and locomotion was monitored by performing an elevated plus maze and open field test. In both tests *Plp1*^{CreERT2/+}; *Fbxo7*^{fl/fl} mice did not show any difference to control mice (**Figure 3.4.2j,k**). To summarize, I found that post-developmental loss of *Fbxo7* from myelinating cells leads to a mild but progressive muscle weakness, as well as a moderate reduction of motor endurance. Nonetheless, *Plp1*^{CreERT2/+}; *Fbxo7*^{fl/fl} mice exhibit a predominantly normal motor and sensory behavior.

3.4 The post-developmental contribution of FBXO7 to the maintenance of the axon-glia interaction

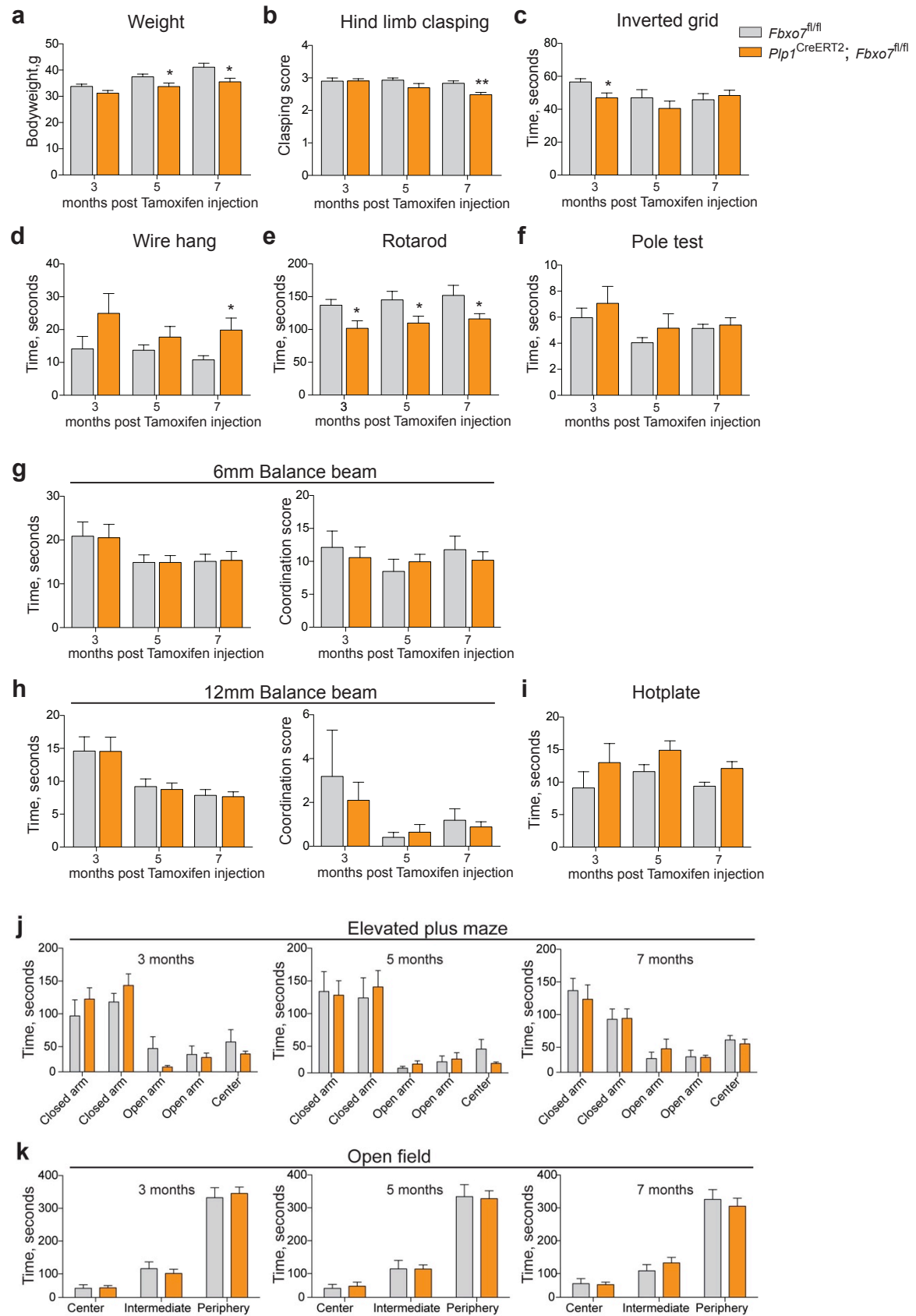


Figure 3.4.2 *Plp1^{CreERT2+}; Fbxo7^{fl/fl}* mice show mild but progressive muscle weakness and reduced motor endurance.

3.4 The post-developmental contribution of Fbxo7 to the maintenance of the axon-glia interaction

(a)-(k) Behavioral analyses of *Fbxo7^{fl/fl}* (n = 10) and *Plp1^{CreERT2/+}; Fbxo7^{fl/fl}* (n = 11) mice three, five and seven months after Tamoxifen injection. Measurements showing **(a)** body weight, **(b)** tail suspension test (3 = normal, 0 = strong hind limb clasping), **(c)** inverted grid, **(d)** wire hang, **(e)** pole test, **(f)** rotarod, **(g)-(h)** balance beam of 6mm and 12mm (0 = unable to cross beam, 7 = normal), **(i)** hotplate, **(j)** elevated plus maze and **(k)** open field test (unpaired t-test, *P < 0.05, **P < 0.01, mean ± s.e.m.).

3.4.3 Post-developmental loss of *Fbxo7* does not affect myelination, but induces a moderate axonal degeneration and immune response.

The deletion of *Fbxo7* from myelinating cells in *Cnp1^{Cre/+}; Fbxo7^{fl/fl}* mice induced a striking axonal degeneration and neuroinflammation in the sciatic nerve. To investigate whether post-developmental loss of *Fbxo7* also affects the integrity of axons or myelination, I decided to take electron microscopic images of sciatic nerve samples from *Plp1^{CreERT2/+}; Fbxo7^{fl/fl}* and *Fbxo7^{fl/fl}* mice 9 months after Tamoxifen injection. Electron microscopic images were taken in collaboration with Prof. Dr. Joachim Weis. Both, embedding of samples and acquisition of images were done with the support of Claudia Krude, Hannelore Mader and Dr. Istvan Katona. The cross-sections of sciatic nerves were analyzed by measuring of the g-ratio, as previously described. Together with my colleague Yuhao Huang, I analyzed the sciatic nerve and found an equal distribution of g-ratio values for cKO-Tam and control mice, indicating no change in myelination in the PNS of *Plp1^{CreERT2/+}; Fbxo7^{fl/fl}* mice (**Figure 3.4.3a**). Furthermore, I measured the average g-ratio of cKO-Tam and control axons and found that both indicated an equal average value of approximately 0.6 (**Figure 3.4.3b**). Additionally, I investigated the effect of post-developmental *Fbxo7* deletion in Schwann cells on axonal integrity and assessed the number of degenerated axons in the sciatic nerve. Here, *Plp1^{CreERT2/+}; Fbxo7^{fl/fl}* mice displayed a slight but not significant increase in degenerated axons (**Figure 3.4.3c**). Since *Cnp1^{Cre/+}; Fbxo7^{fl/fl}* mice revealed a prominent infiltration of macrophages in the sciatic nerve, I further observed the electron microscopic images for signs of inflammation. Interestingly, in the 15 images of cKO-Tam mice and 15 images of control mice, I found slightly more macrophages in the sciatic nerve of cKO-Tam mice than in control. However, this signs of inflammation in *Plp1^{CreERT2/+}; Fbxo7^{fl/fl}* sciatic nerve was certainly weaker than compared to *Cnp1^{Cre/+}; Fbxo7^{fl/fl}* mice. While *Cnp1^{Cre/+}; Fbxo7^{fl/fl}* mice displayed countless macrophages in cKO samples and non in control, *Plp1^{CreERT2/+}; Fbxo7^{fl/fl}* mice showed roughly 9 macrophages in cKO-Tam sciatic nerve sections and about 3 in control mice (**Figure 3.4.3d**). Concluding, from these results I showed that post-developmental deletion

3.4 The post-developmental contribution of FBXO7 to the maintenance of the axon-glia interaction

of *Fbxo7* from Schwann cells does not affect the integrity of myelination, however moderately impacts the integrity of axons in the sciatic nerve and further induces a mild increase in inflammatory response.

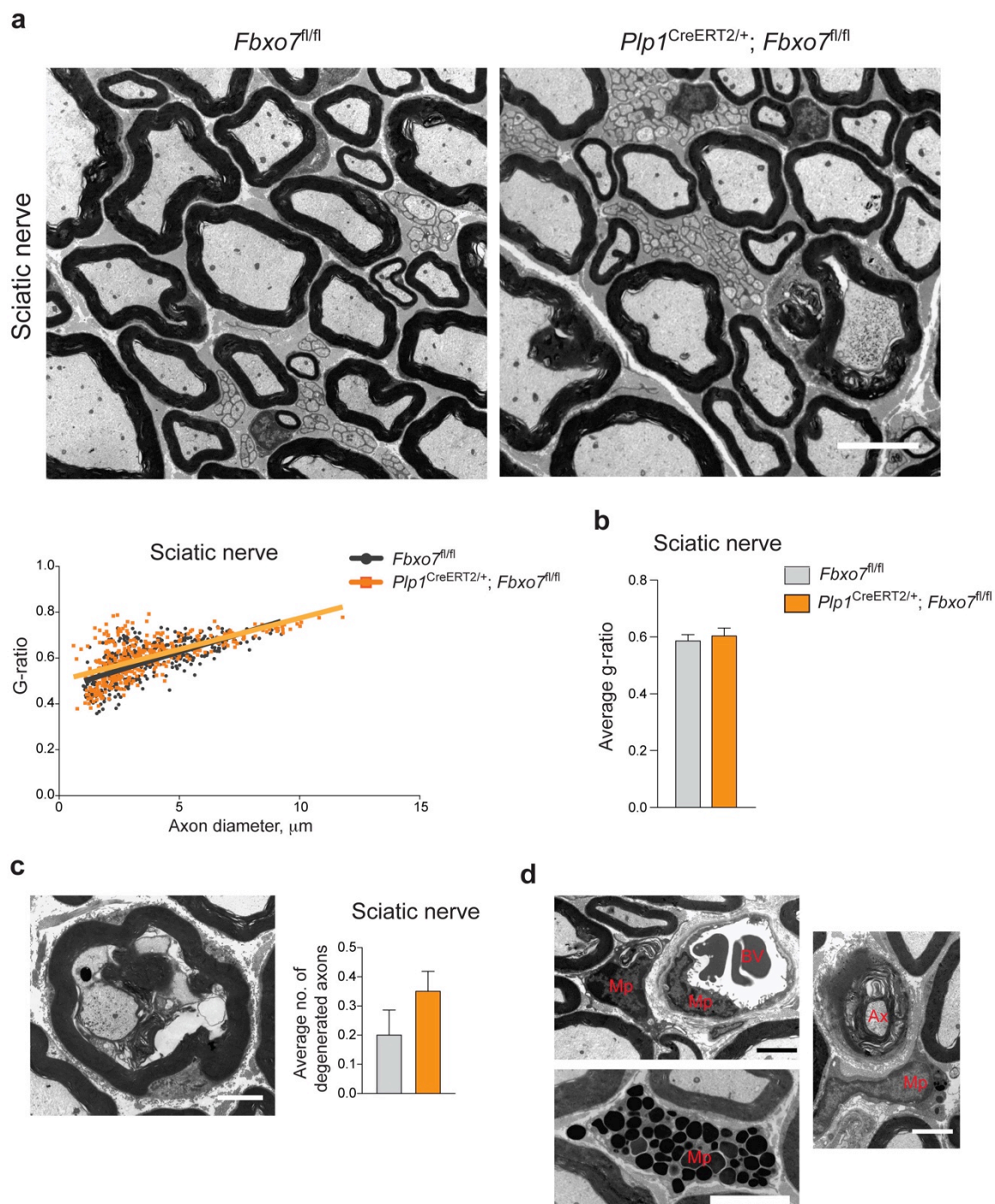


Figure 3.4.3 *Plp1^{CreERT2/+}; Fbxo7^{fl/fl}* mice display no alteration in PNS myelination and no significant but slight increase in axonal degeneration and inflammation.

(a)-(c) Representative electron microscopic images of sciatic nerve cross-sections from *Plp1^{CreERT2/+}; Fbxo7^{fl/fl}* and of *Fbxo7^{fl/fl}* mice 9 months after Tamoxifen injection. Four independent animals per condition and 15 images per mouse were included in the analyses. (a) G-ratio was measured and displayed as scatter plot,

3.4 The post-developmental contribution of FBXO7 to the maintenance of the axon-glia

presenting 400 axons per genotype. Scale bar = 5 μ m. G-ratio of sciatic nerve was measured with the help of Yuhao Hunag. **(b)** Average g-ratio of all measured axons from *Fbxo7^{fl/fl}* and *Plp1^{CreERT2/+}; Fbxo7^{fl/fl}* mice (unpaired t-test, mean \pm s.e.m.). **(c)** Further on, the average number of degenerated axons was counted. Electron microscopic image from sciatic nerve represents axonal degeneration. Scale bar = 2 μ m. **(d)** Images illustrate increased infiltration of sciatic nerve by macrophages engulfing dead, myelinated axons and migrating in from blood vessel. Mp = macrophage, Ax = axon, BV = blood vessel. Scale bar = 2 μ m.

4. Discussion

In this study, I investigated the functions of *Fbxo7* in myelinating cells and determined its impact on the integrity of myelination and the axon-myelin interaction using the newly generated *Cnp1^{Cre/+};Fbxo7^{fl/fl}* mouse line. Additionally, I investigated the post-developmental relevance of FBXO7 in myelinating cells with the Tamoxifen-inducible *Plp1^{CreERT2/+};Fbxo7^{fl/fl}* mouse line.

4.1 Deletion of *Fbxo7* in myelinating cells results in a strong motor phenotype in *Cnp^{Cre/+};Fbxo7^{fl/fl}* mice

The *Cnp^{Cre/+};Fbxo7^{fl/fl}* (cKO) mice are characterized by a severe denervation and atrophy of the musculoskeletal system. This severe muscle weakness manifested itself in decreased motor performance at 6 weeks of age and in paresis, of the hind limbs. Moreover, cKO mice displayed a loss of tail tip tone, which further underlines a strong impact of *Fbxo7* deletion on the PNS. The overall condition of *Cnp^{Cre/+};Fbxo7^{fl/fl}* mice rapidly declined within 4 months of age, which dictated the endpoint of the experimental analyses. The loss of *Fbxo7* in myelinating cells therefore induced a rapid progression of severe symptoms. Generally, mutations in genes encoding for myelin proteins, or even deletions of such genes are not accompanied by embryonic lethality, as myelination only peaks postnatally in mammals. However such alterations can affect the development of myelin and induce progressive disorders (Nave, 2010a).

The prominent expression of FBXO7 in myelinating cells was previously shown in brain sections of conventional *Fbxo7* knockout mice. My colleague Dr. Brockelt showed that FBXO7 is present in the white matter of cerebellum and corpus callosum, by performing a β -galactosidase staining of brain sections, in which the lacZ expression cassette was under the control of the endogenous *Fbxo7* promoter (Brockelt, 2015). Additionally, an RNA sequencing transcriptome database, generated by Zhang *et al.* in 2014, compared the expression of different RNA sequences of purified neurons, astrocytes, oligodendrocyte precursor cells (Melander *et al.*), newly formed oligodendrocytes, myelinating oligodendrocytes, microglia and endothelial cells from mouse cerebral cortex and showed that FBXO7 expression is the highest in OPC and newly formed oligodendrocytes (Zhang *et al.*, 2014). The comparison of FBXO7 expression further showed that FBXO7 is more abundant in glial cells than in neurons (Zhang *et al.*, 2014).

4.2 Loss of *Fbxo7* does not affect myelin integrity, but leads to degeneration of large-caliber axons in the PNS

The mouse line we generated, harbors a *Cnp1* promoter-driven deletion of *Fbxo7* in myelinating cells. *Cnp* is expressed in oligodendrocyte precursor cells (OPC) already in early stages of embryonic development at around E (embryonic day) 12.5 (Peyron et al., 1997; Yu et al., 1994). *Cnp*^{-/-} mice develop comparably normal without any obvious signs of impairments until four months of age. However, these mice reveal progressive motor deficits and hind limb impairment at around 6 months of age. Further on, *Cnp*^{-/-} mice display a similar phenotype as shown in *Cnp*^{Cre/+};*Fbxo7*^{fl/fl} mice, since *Cnp*^{-/-} mice also indicate muscle weakness, weight loss, gait abnormalities and a notable kyphosis. Nonetheless, *Cnp*^{-/-} mice live twice as long as cKO mice and die around 8-15 months of age (Lappe-Siefke et al., 2003). These similarities between *Cnp*-null and *Cnp*^{Cre/+};*Fbxo7*^{fl/fl} mice, might raise the question whether the phenotype of the cKO mouse line might be due to the haplo-insufficiency of the *Cnp* gene. However, investigations of *Cnp*^{+/-} mice revealed no abnormalities in behavior or phenotype until 24 months of age and showed a normal lifespan comparable to wild type mice, indicating that lower *Cnp* levels are either sufficient or can be fully compensated (Hagemeyer et al., 2012; Lappe-Siefke et al., 2003). *Cnp-Cre*^{+/-} mice were therefore a suitable driver line in our mouse model.

Interestingly, loss of *Fbxo7* induced a much stronger phenotype as seen in *Cnp1*^{-/-} mice, although CNP is a well established myelin protein that comprises approximately 4% of CNS and 0.5% of PNS myelin (de Monasterio-Schrader et al., 2012). Therefore, this early and strong phenotype of *Cnp1*^{Cre/+};*Fbxo7*^{fl/fl} mice demonstrates the vital role of FBXO7 and the crucial importance of a functional UPS in myelinating cells.

4.2 Loss of *Fbxo7* does not affect myelin integrity, but leads to degeneration of large-caliber axons in the PNS

Loss of *Fbxo7* revealed a strong impact on the axon-myelin interaction, with little or no impact on myelin integrity. While myelinated axons of cKO mice from the sciatic nerve showed mild, but not significant hypomyelination as compared to control mice, the number of axons in the sciatic nerve were significantly reduced, indicating axonal degeneration. Alterations upon loss of *Fbxo7* in the PNS occurred without influencing the number of Schwann cells present in the sciatic nerve, but induced a remarkable shift of axon diameter. Measurements demonstrated a significant loss of large-caliber axons and a potential compensatory increase in small-caliber axons in the sciatic nerve of *Cnp1*^{Cre/+};*Fbxo7*^{fl/fl} mice.

4.2 Loss of *Fbxo7* does not affect myelin integrity, but leads to degeneration of large-caliber axons in the PNS

Why large-caliber axons are more susceptible to degeneration is not fully understood. It is speculated that larger axons have higher metabolic and trophic demands, which render them more vulnerable to dysfunctions (Blight, 1991; Blight and Decrescito, 1986). Moreover, the intimate interaction of myelinating cells and their ensheathed axons is known to regulate axon diameter. Signaling of the axonal ligand neuregulin type III and its receptor ErbB3 on Schwann cells have been shown to be vital for myelination and the integrity of axons (Michailov et al., 2004; Riethmacher et al., 1997; Simon et al., 2010; Taveggia et al., 2005). While axon diameter is regulated by myelinating cells during development (Hsieh et al., 1994; Sanchez et al., 1996), dysmyelinating disease models with alterations in crucial myelin proteins, have been shown to reduce axon caliber (Brady et al., 1999; de Waegh et al., 1992). Charcot-Marie-Tooth (CMT) disease, also referred to as CMT1A, is the most common inherited neuropathy and can be caused by a duplication of the *Pmp22* gene. This alteration will lead to a slow-progressing demyelination, axonal degeneration and eventually distal pronounced muscle atrophy (Krajewski et al., 2000; Patel et al., 1992; Timmerman et al., 1992). The amount of secondary axonal death determines the disease severity (Berciano et al., 2000).

In my results, I showed that *Fbxo7* deletion induced a subtle change in myelination of peripheral axons and that myelin proteins of the PNS indicated a down-regulation of proteins associated with neuropathy and cytoskeleton mobility. Since structural proteins of myelin were not affected by deletion of *Fbxo7*, this further supports the assumption that FBXO7 acts as crucial UPS protein in the axon-myelin communication and helps to sustain the supportive function of myelinating cells for axonal integrity.

The investigation of our *Cnp1^{Cre/+};Fbxo7^{fl/fl}* mouse line indicated the important role of FBXO7 during development. Especially in the PNS, early deletion of *Fbxo7* induced a strong impact on the axon-glia interaction and integrity of axons. The essential communication between Schwann cells and axons during development was previously shown, as disruption of the ErbB3 receptor leads to secondary axonal loss and severe neuropathy (Riethmacher et al., 1997). Genetic mutations that induce changes in myelinating cells, often affect PNS fibers innervating the most distal muscle groups first and cause a length-dependent axonal loss (Nave, 2010a; Suter and Scherer, 2003). This can be observed in the *Plp1^{-/-}* mouse model, in which the break down of axonal transport leads to axonal swellings and subsequently to a degeneration of distal axons (Garbern and Hobson, 2002; Griffiths et al., 1998). Neurons with long axons present a logistic problem, as their diameter often only measures a few micrometers but their length can be hundreds of centimeters in large mammals (Griffin and Watson, 1988; Nave, 2010b). Moreover, dysfunctional myelinating cells and the resulting lack of support appears to be

4.3 Deletion of *Fbxo7* causes a shift in axon diameter without affecting myelination in the CNS

most vulnerable for long-traveling axons, since these axons have a higher demand in energy supply that is generally provided by myelinating cells (Funfschilling et al., 2012; Nave, 2010b; Simons and Nave, 2015).

The great influence of FBXO7 on the supportive function of myelinating cells towards axons and their integrity might lie in its remarkable function as being part of the ubiquitin proteasomal system (UPS). FBXO7 has multiple interaction partners and therefore many different sites of interaction within a myelinating cell that affects axonal survival. The vital role of the UPS for the stability of axons was demonstrated by other UPS-associated *PARK* genes - *PARK5*. *PARK5* encodes for the deubiquitinase UCH-L1 and similarly as seen in *Cnp1^{Cre/+};Fbxo7^{fl/fl}* mice, conventional *Uchl1* knockout mice display axonal death and denervation of muscles, progressive paralysis and premature death at around 7 months of age (Bishop et al., 2016; Chen et al., 2010). Moreover *Uchl1*-deficient mice present early-onset sensory and motor ataxia at 3 months of age (Mukoyama et al., 1989). These findings indicate an essential role of UCH-L1 for axonal health and stability and thus for neuronal survival (Bishop et al., 2016).

4.3 Deletion of *Fbxo7* causes a shift in axon diameter without affecting myelination in the CNS

In the CNS, loss of *Fbxo7* did not induce dramatic changes on the axon-myelin interaction as seen in the PNS. However, oligodendrocytes responded to the loss of *Fbxo7* with a significant shift in axon caliber. cKO mice displayed significantly larger axons in the CNS as compared to control mice, while the number of healthy myelinated axons in the optic nerve of *Cnp1^{Cre/+};Fbxo7^{fl/fl}* mice remained unchanged. The axons of cKO mice optic nerve presented no signs of axonal swelling, but indicated a mild trend of increased axonal death compared to control mice. Oligodendrocytes further showed a slight but not significant increase in nuclei abundance, without alteration in myelin thickness.

Similar effects were observed in a study, in which the CNS-specific myelin-associated oligodendrocyte basic protein (MOBP) was deleted. The analysis of *Mobp^{-/-}* mice revealed that axons of the optic nerve had larger diameter and more myelin lamellae as compared to controls (Sadahiro et al., 2000). Since axonal growth determines the rate of myelin formation, the number of myelin lamellae increase in proportion to the axon diameter (Fraher, 1976; Friede and Miyagishi, 1972; Hildebrand and Hahn, 1978). Hence, Sadahiro and authors concluded that MOBP regulates axon diameter, while the number of myelin lamellae is dependent on the size of the axon (Sadahiro et al., 2000). Another regulator of axon size is myelin basic protein (MBP). Mice expressing decreased levels of the *Mbp*

4.4 FBXO7 remains relevant for the post-developmental maintenance of the axon-myelin interaction

gene display larger myelinated axons than control mice (Shine et al., 1992). In the *Cnp^{Cre/+};Fbxo7^{fl/fl}* mice, loss of *Fbxo7* induced an increase in axon diameter in the optic nerve without significantly affecting myelination. Although I did not count the number of myelin lamellae of myelinated axons in the optic nerve, the g-ratio measurements indicated no significant change in myelin thickness. A potential secondary response of myelinating cells to an axonal shift, however might be the slight increase in oligodendrocyte abundance in *Cnp^{Cre/+};Fbxo7^{fl/fl}* optic nerve. Similar as MOBP and MBP, FBXO7 might have a regulatory function in axon diameter and act as a mediator of the interaction between myelinating cells and axons.

Interestingly, the function of FBXO7 appears to have a different impact on myelinating cells of the CNS as compared to the PNS. Why deletion of *Fbxo7* lead to an increase in axonal diameter in the optic nerve, but led to more small-caliber axons in the sciatic nerve is unclear. So far, nothing is known about the expression level of FBXO7 in oligodendrocytes compared to Schwann cells. As loss of *Fbxo7* affected the interaction of axons and Schwann cell more dramatically than the oligodendrocyte-axon communication, this might imply a higher expression or greater importance of FBXO7 in Schwann cells. Deletion of *Fbxo7* potentially induces an increase in axon caliber in both nervous systems, however its possible greater impact on Schwann cells might lead to a more dramatic disturbance of myelin support of PNS axons. Hence, early loss of *Fbxo7* in Schwann cells might contribute to a greater stress and vulnerability of long-traveling, peripheral axons, leading to increased axonal death in the PNS. To verify this hypothesis, further investigations are required that compare the expression levels of FBXO7 in both systems.

4.4 FBXO7 remains relevant for the post-developmental maintenance of the axon-myelin interaction

As FBXO7 was shown to be highly expressed in OPCs and newly forming oligodendrocytes, deletion of FBXO7 in the *Cnp^{Cre/+};Fbxo7^{fl/fl}* mouse line revealed the developmental importance of FBXO7 (Zhang et al., 2014). I showed that *Fbxo7* was deleted in *Cnp^{Cre/+};Fbxo7^{fl/fl}* mice around postnatal day 30. Having established the strong developmental influence of FBXO7 on myelinating cells, the question arose as to how FBXO7 might affect the post-developmental axon-glia interface. I therefore generated and analyzed the Tamoxifen-inducible *Plp1^{CreERT2/+}; Fbxo7^{fl/fl}* mouse line, in which *Fbxo7* was

4.5 Lack of *Fbxo7* elicits a strong inflammatory response and an increase in detoxification processes

deleted at 2 months of age when myelination was completed. The post-developmental effect of *Fbxo7* deletion on myelinating cells was less severe, as cKO-Tam mice revealed a milder phenotype. *Plp1^{CreERT2/+}; Fbxo7^{fl/fl}* mice displayed progressive muscle weakness of hind limbs, resulting in a moderate reduction of motor endurance. Further more, cKO-Tam mice indicated a stagnating body weight, but otherwise presented no distinct phenotype or signs of pain and had a normal lifespan. Similar to the *Cnp1^{Cre/+}; Fbxo7^{fl/fl}* mouse line, *Plp1^{CreERT2/+}; Fbxo7^{fl/fl}* mice showed no alterations in myelination of axons in the sciatic nerve. The number of degenerated axons in the sciatic nerve of cKO-Tam mice was slightly elevated as compared to control mice, but significantly lower as compared to *Cnp1^{Cre/+}; Fbxo7^{fl/fl}* mice. This demonstrates the vital importance of FBXO7 during development, but still shows that FBXO7 remains relevant for the post-developmental maintenance of the myelin-axon interplay and the supportive role of myelinating cells for axonal integrity.

4.5 Lack of *Fbxo7* elicits a strong inflammatory response and an increase in detoxification processes

The significant increase in neuroinflammation was one very prominent event, which was induced by loss of *Fbxo7* in both CNS and PNS as well as when post-developmentally deleted. *Cnp1^{Cre/+}; Fbxo7^{fl/fl}* mice presented strong astrogliosis and microgliosis in the myelin areas of the CNS and the PNS. Moreover, electron microscopic images of the sciatic nerve from *Plp1^{CreERT2/+}; Fbxo7^{fl/fl}* and *Cnp1^{Cre/+}; Fbxo7^{fl/fl}* mice showed a noticeable infiltration by macrophages.

Inflammation is a common phenotype seen in many neurodegenerative diseases and often precedes the onset of cellular degeneration and neurological disorders (Carson et al., 2006; Halliday and Stevens, 2011; Wyss-Coray and Mucke, 2002). Microglia sense even the smallest pathological changes, but only when the damage is severe enough activated microglia will initiate phagocytosis and secrete cytokines that activate astrocyte that lead to astrogliosis (Jansen et al., 2014). These activated astrocytes in turn influence the function of microglia, by releasing cytokines and thereby create a feedback loop in which both cells regulate each other (Amor et al., 2014; Zhang et al., 2010). Initial activation of astrocytes forms a protective border around damaged areas and is meant to be protective for neurons (Pekny and Pekna, 2014). However, persisting activation of astrocytes are unable to support neurons and therefore contribute to neuronal dysfunction (Pickering et al., 2005).

4.5 Lack of Fbxo7 elicits a strong inflammatory response and an increase in detoxification processes

Dysfunctional oligodendrocytes are known to trigger an inflammatory response, and contribute to axonal degeneration and to the severity of the disease, as inflammation poses an additional burden for axonal survival (Ip et al., 2006; Kassmann et al., 2007; Lappe-Siefke et al., 2003; Wieser et al., 2013). During the process of inflammation, activated microglia generate nitric oxide, which readily diffuses into axons and perturbs the mitochondrial ATP generation (Nave, 2010b; Smith and Lassmann, 2002; Trapp and Stys, 2009). Interestingly, I found in mass spectrometry analyses that loss of *Fbxo7* decreased mitochondrial proteins in purified myelin from CNS and PNS. This suggests that the strong inflammatory reaction induced by *Fbxo7* deletion in the CNS and PNS of *Cnp1^{Cre/+};Fbxo7^{fl/fl}* mice triggers the generation of NO species, which act as free radicals and induce oxidative stress in the cell. Indeed, I further demonstrated the increase of oxidative stress in myelinating cells, as levels of the endogenous stress sensor GST π 1 were elevated in both the CNS and PNS.

The mass spectrometry analyses further showed a dramatic increase in proteins linked to inflammation in PNS myelin. Hence, it suggests that axons of the PNS are potentially exposed to more stress and toxic substances, such as nitric oxide generated by activated microglia, which would induce a stronger degeneration of axons. To validate this hypothesis, the levels of NO in PNS axons have to be measured. This would provide more evidence on whether the increase in inflammation is accountable for the stronger axonal degeneration in the PNS as compared to CNS, which I reported for *Cnp1^{Cre/+};Fbxo7^{fl/fl}* mice. However, the question still remains as to why loss of *Fbxo7* induces a stronger immune response in the PNS than in the CNS.

The inflammatory response of glial cells further leads to an up-regulation of the NF- κ B or JKN pathway, which is controlled by UPS components (Dalal et al., 2012; Stefanova et al., 2012). The E3 ubiquitin ligase RING finger protein 11 (RNF11) is known to be one of the key negative regulators of the NF- κ B pathway (Dalal et al., 2012). Furthermore, FBXO7 indirectly decreases the NF- κ B signaling pathway, by ubiquitinating proteins of the NF- κ B cascade (Chang et al., 2006; Chen and Goeddel, 2002; Kuiken et al., 2012). Hence, the deletion of *Fbxo7* might lead to an uncontrolled increase of the NF- κ B signaling in *Cnp1^{Cre/+};Fbxo7^{fl/fl}* mice, which results in a strong neuroinflammatory event as seen in both mouse models.

The contribution of the UPS to the course of inflammation is further shown by the transformation of proteasomes in glia cells. During an inflammatory response, the secretion of cytokines such as interferon gamma induces the formation of immunoproteasomes in glia cells, which contributes to a more efficient clearance of disease-causing proteins and further activates the immune response (Basler et al., 2013;

4.5 Lack of Fbxo7 elicits a strong inflammatory response and an increase in detoxification

Sijts and Kloetzel, 2011). However, it is unknown whether the long-term induction of immunoproteasomes are beneficial or detrimental in neurodegenerative diseases, as chronic inflammation is known to contribute to the degeneration of neurons (Tansey et al., 2012).

While *Cnp1*^{-/-} mice show progressive inflammation in the CNS, *Cnp1*^{+/-} mice do not exhibit any signs of inflammation until 12 months of age (Hagemeyer et al., 2012; Lappe-Siefke et al., 2003; Wieser et al., 2013). The prominent inflammatory events due to loss of *Fbxo7* in the *Cnp1*^{Cre/+};*Fbxo7*^{fl/fl} mice, therefore must originate from a dysfunctional UPS in myelinating cells.

As mentioned before, deletion of *Fbxo7* caused an up-regulation of proteins involved in the detoxification process. In both CNS and PNS, the levels of GST π 1 were increased in *Cnp1*^{Cre/+};*Fbxo7*^{fl/fl} mice. While the mass spectrometry of purified CNS myelin showed significant increase in GST π 1 levels, GST π 1 was not among the list of highly up-regulated proteins in PNS myelin. Nonetheless, GST π 1 stainings of the sciatic nerve demonstrated increased levels of the enzyme. Furthermore, PNS myelin contained many other proteins linked to detoxification processes, which were up-regulated upon *Fbxo7* deletion.

Glutathione S-transferase π 1 is a phase II detoxification enzyme that catalyzes the conjugation of xenobiotic and electrophilic components with reduced glutathione (GSH) (Sheehan et al., 2001; Udomsinprasert et al., 2005). There are three isoforms expressed in the nervous system (GST α , GST μ and GST π), out of which GST π is predominately expressed in myelinating cells (Castro-Caldas et al., 2009; Tamura et al., 2007). Upon low cellular stress, GST π 1 prevents apoptosis while inhibiting C-jun phosphorylation by JNK (Adler et al., 1999; Laborde, 2010; Wang et al., 2001). However, increased cellular oxidative stress induces the oligomerization of GST π 1, inhibiting its function and resulting in apoptosis (Townsend and Tew, 2003).

A similar increase of proteins of the detoxification pathway was seen in glia cells of parkin knockout mice. Just like FBXO7, parkin functions as an E3-ubiquitin ligase is encoded by a *PARK* gene. Glia cells of *parkin* knockout mice showed increased levels of glutathione and glutathione S-transferase activity (Solano et al., 2008). An increased redox status is known to modulate the process of protein ubiquitination via reversible S-thiolation of E1 and E2 enzymes, presumably by glutathione (Jahngen-Hodge et al., 1997).

Oligodendrocytes seem to be particularly susceptible to oxidative stress and often appear as vulnerable as neurons to insults caused by oxidation or ischemia (Juurlink et al., 1998; Osterhout et al., 2002; Sypecka, 2003). This might be due to their high content of iron,

4.6 Mutation in the *FBXO7* gene cause Parkinsonian-Pyramidal syndrome

which is predominantly present in oligodendrocytes and myelin sheaths (Connor and Menzies, 1996; Todorich et al., 2009). Additionally, oligodendrocytes are low in glutathione and glutathione peroxidase, rendering them more sensitive to oxidative stress (Juurlink et al., 1998). The observed increase in GST π 1 levels might thus reflect an attempt of myelinating cells to overcome their deficiency in scavenging reactive oxygen species.

Another endogenous redox sensor that responds to oxidative stress is DJ-1 (Shadrach et al., 2013). DJ-1 is also known as *PARK7* and further belongs to the 20 identified *PARK* genes. Interestingly, its level was significantly down-regulated in purified myelin from the PNS of *Cnp1^{Cre/+};Fbxo7^{fl/fl}* mice. DJ-1 shows increased susceptibility to oxidative stress and regulates factors regarding stress-induced cell death (Chan and Chan, 2015; Shadrach et al., 2013). It has been suggested that DJ-1 functionally interacts with *FBXO7* and parkin, since all three *PARK* genes have been linked to mediate mitochondrial function, but the direct interaction has so far not been validated. Since my data show a down-regulation of DJ-1 upon *Fbxo7* deletion, it indicates that both proteins influence each other in their expression levels. Whether this influence is achieved via a direct or indirect interaction, remains to be elucidated.

These examples show that a dysfunctional UPS often lead to an up-regulation of detoxification processes, as the result of oxidative stress in the cells. Moreover, as mutations in *FBXO7*, *Parkin* and *DJ-1* are known to induce different forms of parkinsonism, it demonstrates the importance of a functional UPS for cellular vitality and further shows that disruption of the UPS leads to severe changes in the cell, contributing to the onset of neurological diseases.

4.6 Mutation in the *FBXO7* gene cause Parkinsonian-Pyramidal syndrome

Mutations in the *Fbxo7* (*PARK15*) gene cause a genetic form of parkinsonism, known as Parkinsonian-Pyramidal Syndrome (PPS) (Di Fonzo et al., 2009; Shojaee et al., 2008). Symptoms seen in these *PARK15* patients are very heterogenic, with signs of parkinsonism and pyramidal tract features, but also additional atypical symptoms (Di Fonzo et al., 2009; Lohmann et al., 2015; Shojaee et al., 2008). So far, research groups that had the opportunity to diagnose and examine these rare cases of PPS, neither reported on peripheral neuropathies, nor on potential defects in myelin, mostly since there is no *PARK15* patient material available.

However, as previously mentioned, *Fbxo7* was found to be stronger expressed in glia cells than in neurons (Zhang et al., 2014). Therefore, glia cells that are affected by FBXO7 dysfunction have to be considered as equally important in their contribution to the disease onset as affected neurons. Interestingly, a brain scan of one PPS patient revealed white matter lesions, indicating a potential influence of *Fbxo7* mutations on myelin integrity (Lohmann et al., 2015). Nonetheless, this finding was only reported in one patient and has to be verified in more *PARK15* patients, since not all reported cases were subjected to MRI scanning. Owing to the immense impact of glia cells on the nervous system, further investigation are relevant and help to elucidate the general role of the E3-ubiquitin ligase FBXO7 in the axon-glia interaction. Deleting *Fbxo7* from myelinating cells in *Cnp1^{Cre/+};Fbxo7^{fl/fl}* mice triggered loss of motor control and a severe impairment of gait, which is reminiscent of pyramidal symptoms seen in PPS patients (Conedera et al., 2016; Paisan-Ruiz et al., 2010; Yalcin-Cakmakli et al., 2014). One of the atypical symptoms that some patients carry is dysarthria, a motor speech disorder resulting from neurological injuries (Lohmann et al., 2015). Here, muscles that are involved in the creation of speech are affected and include those of respiration, resonance or phonation. Although I did not investigated how loss of *Fbxo7* in myelinating cells affected the diaphragm or intercostal muscles of respiration, I did found a pronounced muscle atrophy of the same type of skeletal muscle throughout the body of the cKO mice. Furthermore, I showed a severe atrophy of cKO lungs, indicating substantial problems of the respiratory system due to potential denervation.

4.7 Molecular changes induced by loss of *Fbxo7*

Loss of *Fbxo7* led to significant down-regulation of proteins associated with the cytoskeleton and mitochondrial functions in both CNS and PNS. While screening for new interaction partners of FBXO7, our lab identified the light chain 1 of the microtubule-associated protein 1B (MAP1B-LC1), MAP1A-LC2 and MAP1S as novel substrates of FBXO7 (Brockelt, 2015). My colleague demonstrated the ubiquitination of MAP1B-LC1 and MAP1A-LC2 by FBXO7 and hypothesized a potential K63 linkage of ubiquitination (Brockelt, 2015). As K63-linked ubiquitination is often thought to induce a functional modification of the target protein, loss of *Fbxo7* and the resulting dysfunction of the UPS might affect the stability of these novel interactors. Indeed, purified myelin from the PNS indicated a significant down-regulation of MAP1B in *Cnp1^{Cre/+};Fbxo7^{fl/fl}* mice as compared to control. Hence, supporting the speculated interaction of FBXO7 and MAP1B *in vivo* and suggesting a possible stabilization of MAP1B by FBXO7 ubiquitination. In order to further

elucidate the interaction of both proteins and to understand the impact of FBXO7 on the cytoskeleton system, additional experiments are required.

Interestingly, DJ-1 (*PARK7*) is known to bind MAP1B and inhibits MAP1B aggregates (Wang et al., 2011). Since DJ-1 as well was decreased upon *Fbxo7* deletion, it potentially influences the cytoskeleton stability as well and illustrates the multi-layered interaction and complex influence that FBXO7 has within many different pathways of the cell.

Changes in the cytoskeletal arrangement can influence the integrity of mitochondria. MAP1B is not only important for microtubule stabilization, it is also required of a proper anterograde transport of mitochondria. In addition, deregulation of MAP1B-LC1 has been shown to induce mitochondrial aggregation (Jimenez-Mateos et al., 2006; Yonashiro et al., 2012). Furthermore, FBXO7 was reported to participate in the mitochondrial quality control mechanism, while acting as scaffold protein for parkin and PINK1, which are recruited to the depolarized mitochondrial membrane (Burchell et al., 2013). The lack of FBXO7 therefore compromises mitochondrial integrity and as seen in the mass spectrometry of purified CNS and PNS myelin induces a significant decrease in mitochondrial proteins in *Cnp1^{Cre/+};Fbxo7^{fl/fl}* mice.

In our previous publication our lab identified the proteasome subunit $\alpha 2$ (PSMA2) as direct interactor and ubiquitination substrate of FBXO7 (Vingill et al., 2016). While my colleagues showed that lack of *Fbxo7* reduced proteasome activity in neurons, I investigated the activity of proteasomes in Schwann cells and performed a proteasome activity assay by measuring the chymotrypsin-like activity of the proteasome, using a fluorogenic peptide substrate. The results showed a reduced proteasome activity in cultured Schwann cells upon FBXO7 knockdown.

Changes in the function of the proteasome have been shown to cause similar pathological symptoms as seen in *Cnp1^{Cre/+};Fbxo7^{fl/fl}* mice. Rats treated with the proteasome inhibitor bortezomib have demonstrated Schwann cell and myelin disturbances associated with mild axonal degenerations (Cavaletti et al., 2007). Moreover, patients treated with bortezomib were reported to develop a dose-dependent neuropathy, including sensory ataxia and axonal changes that slightly improved after the treatment was stopped for six months (Filosto et al., 2007). As high doses of bortezomib-related neuropathy induced myelin damage in the PNS, the authors hypothesized that inhibition of proteasomes in myelinating cells may be a target for the drug-induced injury (Filosto et al., 2007). Additionally, it was reported that cultured primary oligodendrocytes were highly susceptible to proteasome inhibition when treated with MG-132, which caused oxidative stress, mitochondrial dysfunction and apoptosis (Goldbaum et al., 2006).

The mass spectrometry of CNS and PNS myelin did not identify a prominent alteration of proteasome-associated proteins. This was not surprising, since ubiquitination of PSMA2 by FBXO7 facilitates the assembly of the proteasome complex, however does not influence the stability of PSMA2. Consistent with my results, brain lysates of conventional *Fbxo7*^{-/-} mice did also not show any difference in PSMA2 protein levels as compared to control (Vingill et al., 2016). While FBXO7 clearly is important for proteasome assembly and activity, lack of *Fbxo7* does not affect levels of proteins that are part of the core or regulatory particles of the proteasome.

5. Conclusion and perspectives

In this study, I showed that FBXO7 plays a crucial role in myelinating cells and their support of axonal integrity. Particularly in Schwann cells, FBXO7 promotes the proper axon-myelin interaction while providing a balanced protein homeostasis and the prerequisite for Schwann cells to ensure axonal stability. While loss of *Fbxo7* induced severe axonal degeneration, myelination of axons in the optic and sciatic nerve was not affected by *Fbxo7* deletion, indicating that FBXO7 has little or no effect on the process of myelination. On comparing the phenotype of *Cnp1^{Cre/+};Fbxo7^{fl/fl}* mice with those observed in *Pip1^{CreERT2/+};Fbxo7^{fl/fl}* mice, I concluded that FBXO7 has a predominant importance for the axon-myelin axis during development and remains relevant for the post-developmental maintenance of the axon-glia interaction, although to a far lesser extent. As part of the UPS, the E3 ubiquitin-ligase FBXO7 plays an essential role in protein homeostasis in the cell. Dysfunction of the UPS is often linked to neurodegenerative disease, but the precise disease-causing mechanisms have only started to be elucidated. In my project, I gathered the first results on FBXO7's impact on myelinating cells and their immediate environment. Further investigations are required to enhance our understanding of the functions of FBXO7 on the axon-myelin interaction. As loss of *Fbxo7* induced different effects in the CNS and PNS, the comparison of FBXO7's expression levels in both systems will add to a better understanding of these differences. While the abundance of FBXO7 in each part of the nervous system might reflect its relevance, FBXO7 may also have different functions in Schwann cells as compared to oligodendrocytes. In order to dissect FBXO7's impact on Schwann cells apart from its affect on oligodendrocytes, additional genetic approaches are required that use cell type-specific driver lines for the PNS or CNS. Moreover, while taking advantage of a different driver-line, the basic results should be reproducible and further underscore the role of FBXO7, independent of any potential ectopic activity of the driver line. FBXO7 is known to directly or indirectly affect and interact with several different pathways and compartments in the cell. The molecular changes in myelin upon *Fbxo7* deletion support the notion that FBXO7 plays a complex role in the cell and provide further foundation for detailed investigations of different pathways affected in myelinating cells. Our lab previously established that proteasomal integrity and thus its activity depends on proper FBXO7 function. Hence, additional investigations are required of how FBXO7 regulates proteasome assembly and the impact that decreased proteasome activity has on e.g. mitochondrial function in myelinating cells. This will help to unravel the complexity of FBXO7's function and the impact that the UPS has on myelinating cells and their axonal interaction, guiding us to a better understanding of the disease-causing mechanism of neurodegenerative disorders.

List of abbreviations

(n)S	Sedimentation region
Aa	Amino acids
ACLY	ATP-citrate synthase
ACO2	Aconitate hydratase
ACOT7	Cytosolic acyl coenzyme A thioester hydrolase
AD	Alzheimer's disease
AIFM1	Apoptosis-inducing factor 1
AKR1B1	Aldose reductase
ALS	Amyotrophic lateral sclerosis
ANOVA	Analysis of variance
ANXA1	Annexin A1
AP	Action potential
APOA4	Apolipoprotein A-IV
APP	Amyloid precursor protein
APS	Ammonium persulfate
AR	Autosomal recessive
ATP	Adenosine triphosphate
ATP1A4	Sodium/potassium-transporting ATPase subunit alpha-4
ATP5A1	ATP synthase subunit alpha
ATP5B	ATP synthase subunit beta
ATP5O	ATP synthase subunit O
Bcl^{XL}	B-cell lymphoma-extra large
BDNF	Brain-derived neurotrophic factor
BME	Basal medium eagle
BSA	Bovine serum albumin
BSG	Basigin
C-Terminus	Carboxyl-terminus (-COOH)
C3	Complement C3
CADM4	Cell adhesion molecule 4
CAMP	Compound muscle action potential
CAT	Catalase
CB	Cerebellum
CD151	CD151 antigen
CD47	Leukocyte surface antigen CD47
CD81	CD81 antigen

CD82	CD82 antigen
CD9	Tetraspanin-29
CDC42	Cell division control protein 42 homolog
CDK6	Cyclin-dependend kinase 6
cDNA	complementary DNA
CEND1	Cell cycle exit and neuronal differentiation protein 1
CES1D	Carboxylesterase 1D
CFL1	Cofilin-1
CFL2	Cofilin-2
CHCHD3	MICOS complex subunit Mic19
ciAP1	Cellular inhibitor of apoptosis 1
cKO	Conditional knockout (<i>Cnp1^{Cre/+};Fbxo7^{fl/fl}</i>)
cKO-Tam	Tamoxifen-induced conditional knockout (<i>Pip1^{CreERT2/+};Fbxo7^{fl/fl}</i> mice)
CLDN11	Claudin 11
CLIC4	Chloride intracellular channel protein 4
CMT	Charcot-Marie-Tooth
CNP	2',3'-cyclic nucleotide 3'-phosphodiesterase
CNS	Central nervous system
CNTF	Ciliary neurotrophic factor
CNTN2	Contactin-2
Co-IP	Co-Immunoprecipitation
CP	Core particle
CPM	Carboxypeptidase M
CR	Corona radiata
Cre	Cyclization recombinase
CRYAB	Alpha-crystallin B chain
CS	Calf serum
C_T	Cycle threshold
CTX	Cortex
CUL1	Cullin 1
Cy2/3	Cyanine 2/3
DAB	3-3'-diaminobenzidine
DAPI	4'6-diamidino-2-phenylindole
ddH₂O	Double distilled water
DJ-1	Protein deglycase 1
DMEM	Dulbecco's modified eagle's medium
DML	Distal motor latency

DNA	Deoxyribonucleic acid
dNTP	Deoxyribonucleotide triphosphate
DPYSL5	Dihydropyrimidinase-related protein 5
DTT	Dithiothreitol
DUB	Deubiquitinating enzymes
DUSP15	Dual specificity protein phosphatase 15
E1	Ubiquitin-activating enzyme
E2	Ubiquitin-conjugating enzyme
E3	Ubiquitin ligase enzyme
ECL	Enhanced chemiluminescence
EDTA	Ethylenediaminetetraacetic acid
ENO1	Enolase 1
ENPP6	Ectonucleotide pyrophosphatase6
ER	Endoplasmic reticulum
ERAD	ER-associated degradation
FACS	Fluorescence-Activated Cell Sorting
FASN	Fatty acid synthase
FBP	F-box protein
FBS	Fetal bovine serum
FBXL	F-box protein with leucine-rich repeats
FBXO	F-box protein with only / other domain motifs
FBXW	F-box protein with WD40 domains
FP	FBOX7-PI31 interaction domain
FSCN1	Fascin
Fwd	Forward
G₁-Phase	Gap-phase
GCAB	Ig gamma-2A chain C regio
GDAP1	Ganglioside-induced differentiation-associated protein 1
GDNF	Glial cell-derived neurotrophic factor
GFAP	Glial fibrillary acidic protein
GFP	Green fluorescent protein
GLUT1	Glucose transporter 1
GNB4	Guanine nucleotide-binding protein subunit beta-4
GPD2	Glycerol-3-phosphate dehydrogenase
GPX1	Glutathione peroxidase 1
GS	Goat serum
GSN	Gelsolin

GSTM2	Glutathione S-transferase Mu
GSTπ1	Glutathione S-transferase π 1
HBSS	Hank's balanced salt solution
HECT	Homologous to E6-associated protein carboxy terminal
HEK293T	Human Embryonic Kidney 293T cells
HEPACAM	Hepatocyte cell adhesion molecule
HEPES	4-(2-hydroxyethyl)-1-piperazineethanesulfonic acid
HRP	Horseradish peroxidase
HS	Horse serum
HSPD1	60 kDa heat shock protein
HURP	Hepatoma up-regulated protein
HVM51	Ig heavy chain V region AC38 205.12
IB	Immunoblot
Iba1	Ionized calcium-binding adapter molecule 1
IGF1	Insulin-like growth factor 1
IgG	Immunoglobulin G
IGH3	Ig gamma-2B chain C region
IGKC	Ig kappa chain C region
IGSF8	Immunoglobulin superfamily member 8
IHC	Immunohistochemistry
IL	Interleukin
IL-1RA	Interleukin 1 receptor antagonist
INA	Alpha-internexin
IP	Immunoprecipitation
IP-10	Interferon γ -induced protein 10
JAM3	Junctional adhesion molecule C
JKN	c-Jun N-terminale Kinase
LacZ	Lactose operon Z
LC-MS	Liquid chromatography–mass spectrometry
LGALS3	Galectin-3
LIF	Leukemia inhibitory factor
M-phase	Mitosis
Mac3	Macrophage antigen 3
MAG	Myelin-associated glycoprotein
MAP (nx)	Microtubule-associated protein (nx)
MAP1B	Microtubule-associated protein 1B
MAP1B LC1	Microtubule-associated protein 1B light chain 1

MAP6	Microtubule-associated protein 6
MBP	Myelin basic protein
MCP-1	Monocyte chemoattractant protein 1
MCT (n)	Monocarboxylate transporter (n)
MHC	Major histocompatibility complex
MIB1	Mind bomb-1
Mm	Mus musculus
MOBP	Myelin-associated oligodendrocytic basic protein
MOG	Myelin-oligodendrocyte glycoprotein
MPZ	Myelin protein P0
MRI	Magnet resonance imaging
mRNA	Messenger RNA
MSC80	Mouse Schwann cells 80
MSN	Moesin
MTCO2	Cytochrome c oxidase subunit 2
mTOR	The mechanistic target of rapamycin
N-Terminus	Amino-terminus (-NH ₂)
NCV	Nerve conductance velocity
NDRG1	Protein NDRG1
NEDD4	Neural precursor cell expressed developmentally down-regulated protein 4
NEFH	Neurofilament heavy
NEFL	Neurofilament light
NEFM	Neurofilament medium
NF- κB	Nuclear factor 'kappa-light-chain-enhancer' of activated B-cells
NFASC	Neurofascin
NO	Nitric oxide
No.	Number
NRG1	Neuregulin1 type III
NT3	Neurotrophin 3
OCT	Optimal cutting temperature
OMG	Oligodendrocyte-myelin glycoprotein
OPALIN	Opalin
OPC	Oligodendrocyte precursor cells
OTUB1	Ubiquitin thioesterase OTUB1
P (n)	Postnatal Day (n)
PARK	PD-associated gene locus

PARK7	Protein deglycase DJ-1
PBS	Phosphate-buffered saline
PBST	Phosphate-buffered saline with Triton-X
PCR	Polymerase chain reaction
PD	Parkinson's disease
PDGF	Platelet derived growth factor
PDHB	Pyruvate dehydrogenase E1 component subunit beta
PFA	Paraformaldehyde
PGAM2	Phosphoglycerate mutase 2
PI31	Proteasomal inhibitor 31
PINK1	PTEN Induced Putative Kinase 1
PLL	Poly-L-Lysin
PLLP	Plasmolipin
PLP	Proteolipid protein
PMP2	Myelin P2 protein
PMP22	Peripheral myelin protein 22
PNS	Peripheral nervous system
PPS	Parkinsonian-Pyramidal Syndrome
PRDX1	Peroxiredoxin-1
PRR	Proline-rich region
PRRT2	Proline-rich transmembrane protein 2
PRX	Periaxin
PSG	Penicillin/Streptomycin/GlutaMax
PSMA2	Proteasomal subunit alpha 2
PTEN	Phosphatase and tensin homolog
RAN	GTP-binding nuclear protein Ran
RBX1	RING-box protein 1
Rev	Reverse
RING	Really Interesting New Gene
RIPA	Radio-immunoprecipitation assay buffer
RNA	Ribonucleic acid
RP	Regulatory particle
RT	Room temperature
RT-PCR	Real time polymerase chain reaction
RTN4	Reticulon 4
RUFY3	Protein RUFY3
s.e.m.	Standard error of the mean

S100B	Protein S100 B
SCF	SKP, Cullin, F-box-containing complex
SCL25A4	ADP/ATP translocase 1
SDS	Sodium dodecyl sulfate
SDS-PAGE	SDS-Polyacrylamide gel electrophoresis
SEPTIN5	Septin-5
shRNA	Short hairpin RNA
SIMPLE	Small integral membrane protein of lysosome/late endosome
SIRT2	NAD-dependent protein deacetylase sirtuin-2
SKP1	S-phase kinase-associated protein 1
SLC25A11	Mitochondrial 2-oxoglutarate/malate carrier protein
SLC44A1	Choline transporter-like protein 1
SNCA	Synuclein, alpha
SNP	Single nucleotide polymorphism
SPTAN1	Spectrin alpha chain
STIP1	Stress-induced-phosphoprotein
STXBP3	Syntaxin-binding protein 3
Suc-LLVY-AMC	<i>N</i> -Succinyl-Leu-Leu-Val-Tyr-AMC (7-amino-4-methylcoumarin)
TAE	Tris base, acetic acid and EDTA
TBS	Tris-buffered saline
TE	Trypsin/EDTA
TEMED	Tetramethylethylenediamine
TNF	Tumor necrosis factor
TOMM70	Mitochondrial import receptor subunit TOM70
TPI1	Triosephosphate isomerase
TPPP	Tubulin polymerization-promoting protein
TRAF2	TNF receptor-associated factor 2
TSPAN-2	Tetraspanin 2
TUBB3	Tubulin beta-3 chain
TUBB4A	Tubulin beta-4A chain
TUBB4B	Tubulin beta-4B chain
TUNEL	TdT-mediated dUTP nick-end labeling
Ub	Ubiquitin
UBE2M	NEDD8-conjugating enzyme Ubc12
UBE2N	Ubiquitin-conjugating enzyme E2 N
UBE2V1	Ubiquitin-conjugating enzyme E2 variant 1
UbR	Ubiquitin-related domain

UCH-L1	Ubiquitin carboxyl-terminal esterase L1
UPLC	Ultra Performance Liquid Chromatography
UPS	Ubiquitin-proteasome system
UQCRC2	Cytochrome b-c1 complex subunit 2
UV	Ultra violet
VAT1	Synaptic vesicle membrane protein VAT-1 homolog
WB	Western blot
WT	Wild type
ZNRF1	Zinc and ring finger 1
α	Anti
β-Gal	β-Galactosidase

<u>Nucleotide</u>	<u>Single-letter code</u>
-------------------	---------------------------

Adenine	A
Cytosine	C
Guanine	G
Thymine	T

<u>Amino acids</u>	<u>3-letter code</u>	<u>Single-letter code</u>
--------------------	----------------------	---------------------------

Arginine	Arg	R
Cysteine	Cys	C
Glycine	Gly	G
Isoleucine	Ile	I
Leucine	Leu	L
Lysine	Lys	K
Methionine	Met	M
Proline	Pro	P
Termination	/	X
Threonine	Thr	T
Tyrosine	Tyr	Y
Valine	Val	V

Units

cm	Centimeter
Mm	Millimeter
μm	Micrometer
nm	Nanometer
L	Liter
ml	Milliliter
μl	Microliter
Kg	Kilogram
g	Gram
mg	Milligram
μg	Microgram
ng	Nanogram
M	Molar
mM	Milimolar
μM	Micromolar
h	Hour
min	Minute
s/sec	Second
ms	Milliseconds
m/s	Meter per seconds
mA	Milliampere
V	Volt
mV	Millivolt
°C	Degrees Celsius
%	Percentage
rpm	Revolutions per minute
g	Gravity
kDa	Kilodalton
bp	Base pairs
kb	Kilobase

Nomenclature

According to the guidelines of the HUGO Gene Nomenclature Committee (HGNC) and the Mouse Genome Informatics (MGI), human as well as mouse gene and protein names were referred to in this study as following:

Example: **F-box only protein 7**

Species	Gene symbol	Protein symbol
Human	<i>FBXO7</i>	FBXO7
Mouse	<i>Fbxo7</i>	FBXO7

References

- Aartsma-Rus, A., and van Putten, M. (2014). Assessing functional performance in the mdx mouse model. *J Vis Exp*.
- Adler, V., Yin, Z., Fuchs, S.Y., Benezra, M., Rosario, L., Tew, K.D., Pincus, M.R., Sardana, M., Henderson, C.J., Wolf, C.R., *et al.* (1999). Regulation of JNK signaling by GSTp. *EMBO J* 18, 1321-1334.
- Allen, N.J., and Barres, B.A. (2009). Neuroscience: Glia - more than just brain glue. *Nature* 457, 675-677.
- Amor, S., Peferoen, L.A., Vogel, D.Y., Breur, M., van der Valk, P., Baker, D., and van Noort, J.M. (2014). Inflammation in neurodegenerative diseases--an update. *Immunology* 142, 151-166.
- An, S.F., Giometto, B., Groves, M., Miller, R.F., Beckett, A.A., Gray, F., Tavolato, B., and Scaravilli, F. (1997). Axonal damage revealed by accumulation of beta-APP in HIV-positive individuals without AIDS. *J Neuropathol Exp Neurol* 56, 1262-1268.
- Araki, T., Nagarajan, R., and Milbrandt, J. (2001). Identification of genes induced in peripheral nerve after injury. Expression profiling and novel gene discovery. *J Biol Chem* 276, 34131-34141.
- Asi, Y.T., Simpson, J.E., Heath, P.R., Wharton, S.B., Lees, A.J., Revesz, T., Houlden, H., and Holton, J.L. (2014). Alpha-synuclein mRNA expression in oligodendrocytes in MSA. *Glia* 62, 964-970.
- Azevedo, F.A., Carvalho, L.R., Grinberg, L.T., Farfel, J.M., Ferretti, R.E., Leite, R.E., Jacob Filho, W., Lent, R., and Herculano-Houzel, S. (2009). Equal numbers of neuronal and nonneuronal cells make the human brain an isometrically scaled-up primate brain. *J Comp Neurol* 513, 532-541.
- Basler, M., Kirk, C.J., and Groettrup, M. (2013). The immunoproteasome in antigen processing and other immunological functions. *Curr Opin Immunol* 25, 74-80.
- Bence, N.F., Sampat, R.M., and Kopito, R.R. (2001). Impairment of the ubiquitin-proteasome system by protein aggregation. *Science* 292, 1552-1555.
- Bennett, V., and Lambert, S. (1999). Physiological roles of axonal ankyrins in survival of premyelinated axons and localization of voltage-gated sodium channels. *J Neurocytol* 28, 303-318.
- Berciano, J., Garcia, A., Figols, J., Munoz, R., Berciano, M.T., and Lafarga, M. (2000). Perineurium contributes to axonal damage in acute inflammatory demyelinating polyneuropathy. *Neurology* 55, 552-559.

- Bheda, A., Gullapalli, A., Caplow, M., Pagano, J.S., and Shackelford, J. (2010). Ubiquitin editing enzyme UCH L1 and microtubule dynamics: implication in mitosis. *Cell Cycle* 9, 980-994.
- Bishop, P., Rocca, D., and Henley, J.M. (2016). Ubiquitin C-terminal hydrolase L1 (UCH-L1): structure, distribution and roles in brain function and dysfunction. *Biochem J* 473, 2453-2462.
- Blight, A.R. (1991). Morphometric analysis of a model of spinal cord injury in guinea pigs, with behavioral evidence of delayed secondary pathology. *J Neurol Sci* 103, 156-171.
- Blight, A.R., and Decrescito, V. (1986). Morphometric analysis of experimental spinal cord injury in the cat: the relation of injury intensity to survival of myelinated axons. *Neuroscience* 19, 321-341.
- Bochtler, M., Ditzel, L., Groll, M., Hartmann, C., and Huber, R. (1999). The proteasome. *Annu Rev Biophys Biomol Struct* 28, 295-317.
- Boutry, J.M., Hauw, J.J., Gansmuller, A., Di-Bert, N., Pouchelet, M., and Baron-Van Evercooren, A. (1992). Establishment and characterization of a mouse Schwann cell line which produces myelin in vivo. *J Neurosci Res* 32, 15-26.
- Bradford, M.M. (1976). A rapid and sensitive method for the quantitation of microgram quantities of protein utilizing the principle of protein-dye binding. *Anal Biochem* 72, 248-254.
- Brady, S.T., Witt, A.S., Kirkpatrick, L.L., de Waegh, S.M., Readhead, C., Tu, P.H., and Lee, V.M. (1999). Formation of compact myelin is required for maturation of the axonal cytoskeleton. *J Neurosci* 19, 7278-7288.
- Brockelt, D. (2015). The role of the E3 ubiquitin ligase FBXO7-SCF in early-onset Parkinson's disease (Göttingen, Georg-August university, doctoral thesis).
- Burchell, V.S., Nelson, D.E., Sanchez-Martinez, A., Delgado-Camprubi, M., Ivatt, R.M., Pogson, J.H., Randle, S.J., Wray, S., Lewis, P.A., Houlden, H., *et al.* (2013). The Parkinson's disease-linked proteins Fbxo7 and Parkin interact to mediate mitophagy. *Nat Neurosci* 16, 1257-1265.
- Cardozo, T., and Pagano, M. (2004). The SCF ubiquitin ligase: insights into a molecular machine. *Nat Rev Mol Cell Biol* 5, 739-751.
- Carson, M.J., Thrash, J.C., and Walter, B. (2006). The cellular response in neuroinflammation: The role of leukocytes, microglia and astrocytes in neuronal death and survival. *Clin Neurosci Res* 6, 237-245.
- Castro-Caldas, M., Neves Carvalho, A., Peixeiro, I., Rodrigues, E., Lechner, M.C., and Gama, M.J. (2009). GSTpi expression in MPTP-induced dopaminergic

- neurodegeneration of C57BL/6 mouse midbrain and striatum. *J Mol Neurosci* 38, 114-127.
- Cavaletti, G., Gilardini, A., Canta, A., Rigamonti, L., Rodriguez-Menendez, V., Ceresa, C., Marmiroli, P., Bossi, M., Oggioni, N., D'Incalci, M., *et al.* (2007). Bortezomib-induced peripheral neurotoxicity: a neurophysiological and pathological study in the rat. *Exp Neurol* 204, 317-325.
- Cenciarelli, C., Chiaur, D.S., Guardavaccaro, D., Parks, W., Vidal, M., and Pagano, M. (1999). Identification of a family of human F-box proteins. *Curr Biol* 9, 1177-1179.
- Chan, J.Y., and Chan, S.H. (2015). Activation of endogenous antioxidants as a common therapeutic strategy against cancer, neurodegeneration and cardiovascular diseases: A lesson learnt from DJ-1. *Pharmacol Ther* 156, 69-74.
- Chang, Y.F., Cheng, C.M., Chang, L.K., Jong, Y.J., and Yuo, C.Y. (2006). The F-box protein Fbxo7 interacts with human inhibitor of apoptosis protein cIAP1 and promotes cIAP1 ubiquitination. *Biochem Biophys Res Commun* 342, 1022-1026.
- Chen, C.M., Chen, I.C., Huang, Y.C., Juan, H.F., Chen, Y.L., Chen, Y.C., Lin, C.H., Lee, L.C., Lee, C.M., Lee-Chen, G.J., *et al.* (2014a). FBXO7 Y52C polymorphism as a potential protective factor in Parkinson's disease. *PLoS One* 9, e101392.
- Chen, F., Sugiura, Y., Myers, K.G., Liu, Y., and Lin, W. (2010). Ubiquitin carboxyl-terminal hydrolase L1 is required for maintaining the structure and function of the neuromuscular junction. *Proc Natl Acad Sci U S A* 107, 1636-1641.
- Chen, G., and Goeddel, D.V. (2002). TNF-R1 signaling: a beautiful pathway. *Science* 296, 1634-1635.
- Chen, J., Liu, Q.J., Wang, D., Zhou, X.Y., Xiong, D., Li, H.J., and Li, C.L. (2014b). Hepatoma upregulated protein expression is involved in the pathogenesis of human breast carcinogenesis. *Oncol Lett* 8, 2543-2548.
- Chen, L., Thiruchelvam, M.J., Madura, K., and Richfield, E.K. (2006). Proteasome dysfunction in aged human alpha-synuclein transgenic mice. *Neurobiol Dis* 23, 120-126.
- Chomiak, T., and Hu, B. (2009). What is the optimal value of the g-ratio for myelinated fibers in the rat CNS? A theoretical approach. *PLoS One* 4, e7754.
- Ciechanover, A., and Schwartz, A.L. (2002). Ubiquitin-mediated degradation of cellular proteins in health and disease. *Hepatology* 35, 3-6.
- Clark, K., Sakowski, L., Sperle, K., Banser, L., Landel, C.P., Bessert, D.A., Skoff, R.P., and Hobson, G.M. (2013). Gait abnormalities and progressive myelin degeneration in a new murine model of Pelizaeus-Merzbacher disease with tandem genomic duplication. *J Neurosci* 33, 11788-11799.

- Conedera, S., Apaydin, H., Li, Y., Yoshino, H., Ikeda, A., Matsushima, T., Funayama, M., Nishioka, K., and Hattori, N. (2016). *FBXO7* mutations in Parkinson's disease and multiple system atrophy. *Neurobiol Aging* 40, 192 e191-195.
- Connor, J.R., and Menzies, S.L. (1996). Relationship of iron to oligodendrocytes and myelination. *Glia* 17, 83-93.
- Corfas, G., Velardez, M.O., Ko, C.P., Ratner, N., and Peles, E. (2004). Mechanisms and roles of axon-Schwann cell interactions. *J Neurosci* 24, 9250-9260.
- D'Urso, D., Brophy, P.J., Staugaitis, S.M., Gillespie, C.S., Frey, A.B., Stempak, J.G., and Colman, D.R. (1990). Protein zero of peripheral nerve myelin: biosynthesis, membrane insertion, and evidence for homotypic interaction. *Neuron* 4, 449-460.
- Dai, X., Lercher, L.D., Clinton, P.M., Du, Y., Livingston, D.L., Vieira, C., Yang, L., Shen, M.M., and Dreyfus, C.F. (2003). The trophic role of oligodendrocytes in the basal forebrain. *J Neurosci* 23, 5846-5853.
- Dalal, N.V., Pranski, E.L., Tansey, M.G., Lah, J.J., Levey, A.I., and Betarbet, R.S. (2012). *RNF11* modulates microglia activation through NF-kappaB signalling cascade. *Neurosci Lett* 528, 174-179.
- Damier, P., Hirsch, E.C., Zhang, P., Agid, Y., and Javoy-Agid, F. (1993). Glutathione peroxidase, glial cells and Parkinson's disease. *Neuroscience* 52, 1-6.
- Dantuma, N.P., and Bott, L.C. (2014). The ubiquitin-proteasome system in neurodegenerative diseases: precipitating factor, yet part of the solution. *Front Mol Neurosci* 7, 70.
- Dantuma, N.P., and Salomons, F.A. (2016). Ubiquitin versus misfolding: The minimal requirements for inclusion body formation. *J Cell Biol* 213, 147-149.
- De Jonghe, P., Timmerman, V., Ceuterick, C., Nelis, E., De Vriendt, E., Lofgren, A., Vercruyssen, A., Verellen, C., Van Maldergem, L., Martin, J.J., *et al.* (1999). The Thr124Met mutation in the peripheral myelin protein zero (MPZ) gene is associated with a clinically distinct Charcot-Marie-Tooth phenotype. *Brain* 122 (Pt 2), 281-290.
- de Lau, L.M., and Breteler, M.M. (2006). Epidemiology of Parkinson's disease. *Lancet Neurol* 5, 525-535.
- de Monasterio-Schrader, P., Jahn, O., Tenzer, S., Wichert, S.P., Patzig, J., and Werner, H.B. (2012). Systematic approaches to central nervous system myelin. *Cell Mol Life Sci* 69, 2879-2894.
- de Waegh, S.M., Lee, V.M., and Brady, S.T. (1992). Local modulation of neurofilament phosphorylation, axonal caliber, and slow axonal transport by myelinating Schwann cells. *Cell* 68, 451-463.

- Delgado-Camprubi, M., Esteras, N., Soutar, M.P., Plun-Favreau, H., and Abramov, A.Y. (2017). Deficiency of Parkinson's disease-related gene *Fbxo7* is associated with impaired mitochondrial metabolism by PARP activation. *Cell Death Differ* 24, 120-131.
- Deshaiies, R.J., and Joazeiro, C.A. (2009). RING domain E3 ubiquitin ligases. *Annu Rev Biochem* 78, 399-434.
- Di Fonzo, A., Dekker, M.C., Montagna, P., Baruzzi, A., Yonova, E.H., Correia Guedes, L., Szczerbinska, A., Zhao, T., Dubbel-Hulsman, L.O., Wouters, C.H., *et al.* (2009). *FBXO7* mutations cause autosomal recessive, early-onset parkinsonian-pyramidal syndrome. *Neurology* 72, 240-245.
- Diaz-Hernandez, M., Valera, A.G., Moran, M.A., Gomez-Ramos, P., Alvarez-Castelao, B., Castano, J.G., Hernandez, F., and Lucas, J.J. (2006). Inhibition of 26S proteasome activity by huntingtin filaments but not inclusion bodies isolated from mouse and human brain. *J Neurochem* 98, 1585-1596.
- Dickson, D.W. (2012). Parkinson's disease and parkinsonism: neuropathology. *Cold Spring Harb Perspect Med* 2.
- Dikic, I. (2017). Proteasomal and Autophagy Degradation Systems. *Annu Rev Biochem*.
- Distler, U., Kuharev, J., Navarro, P., Levin, Y., Schild, H., and Tenzer, S. (2014). Drift time-specific collision energies enable deep-coverage data-independent acquisition proteomics. *Nat Methods* 11, 167-170.
- Distler, U., Kuharev, J., Navarro, P., and Tenzer, S. (2016). Label-free quantification in ion mobility-enhanced data-independent acquisition proteomics. *Nat Protoc* 11, 795-812.
- Du, Y., and Dreyfus, C.F. (2002). Oligodendrocytes as providers of growth factors. *J Neurosci Res* 68, 647-654.
- Dupouey, P., Jacque, C., Bourre, J.M., Cesselin, F., Privat, A., and Baumann, N. (1979). Immunochemical studies of myelin basic protein in shiverer mouse devoid of major dense line of myelin. *Neurosci Lett* 12, 113-118.
- Eddy, N.B., and Leimbach, D. (1953). Synthetic analgesics. II. Dithienylbutenyl- and dithienylbutylamines. *J Pharmacol Exp Ther* 107, 385-393.
- Edgar, J.M., McLaughlin, M., Werner, H.B., McCulloch, M.C., Barrie, J.A., Brown, A., Faichney, A.B., Snaidero, N., Nave, K.A., and Griffiths, I.R. (2009). Early ultrastructural defects of axons and axon-glia junctions in mice lacking expression of *Cnp1*. *Glia* 57, 1815-1824.
- Ehlers, M.D. (2003). Activity level controls postsynaptic composition and signaling via the ubiquitin-proteasome system. *Nat Neurosci* 6, 231-242.

- Erdmann, G., Berger, S., and Schutz, G. (2008). Genetic dissection of glucocorticoid receptor function in the mouse brain. *J Neuroendocrinol* 20, 655-659.
- Eric R. Kandel, J.H.S., Thomas M. Jessell (2000). Principles of neuronal scienc, fourth edition edn (McGraw-Hill).
- Feltri, M.L., Poitelon, Y., and Previtali, S.C. (2016). How Schwann Cells Sort Axons: New Concepts. *Neuroscientist* 22, 252-265.
- Filosto, M., Rossi, G., Pelizzari, A.M., Buzio, S., Tentorio, M., Broglio, L., Mancuso, M., Rinaldi, M., Scarpelli, M., and Padovani, A. (2007). A high-dose bortezomib neuropathy with sensory ataxia and myelin involvement. *J Neurol Sci* 263, 40-43.
- Finley, D. (2009). Recognition and processing of ubiquitin-protein conjugates by the proteasome. *Annu Rev Biochem* 78, 477-513.
- Fraher, J.P. (1976). The growth and myelination of central and peripheral segments of ventral motoneurone axons. A quantitative ultrastructural study. *Brain Res* 105, 193-211.
- Friede, R.L., and Miyagishi, T. (1972). Adjustment of the myelin sheath to changes in axon caliber. *Anat Rec* 172, 1-14.
- Funfschilling, U., Supplie, L.M., Mahad, D., Boretius, S., Saab, A.S., Edgar, J., Brinkmann, B.G., Kassmann, C.M., Tzvetanova, I.D., Mobius, W., *et al.* (2012). Glycolytic oligodendrocytes maintain myelin and long-term axonal integrity. *Nature* 485, 517-521.
- Gallyas, F. (1979). Silver staining of myelin by means of physical development. *Neurol Res* 1, 203-209.
- Garbern, J., and Hobson, G. (2002). Prenatal diagnosis of Pelizaeus-Merzbacher disease. *Prenat Diagn* 22, 1033-1035.
- Garbern, J.Y. (2007). Pelizaeus-Merzbacher disease: Genetic and cellular pathogenesis. *Cell Mol Life Sci* 64, 50-65.
- Garbern, J.Y., Yool, D.A., Moore, G.J., Wilds, I.B., Faulk, M.W., Klugmann, M., Nave, K.A., Sistermans, E.A., van der Knaap, M.S., Bird, T.D., *et al.* (2002). Patients lacking the major CNS myelin protein, proteolipid protein 1, develop length-dependent axonal degeneration in the absence of demyelination and inflammation. *Brain* 125, 551-561.
- Glickman, M.H., and Ciechanover, A. (2002). The ubiquitin-proteasome proteolytic pathway: destruction for the sake of construction. *Physiol Rev* 82, 373-428.

- Goldbaum, O., Vollmer, G., and Richter-Landsberg, C. (2006). Proteasome inhibition by MG-132 induces apoptotic cell death and mitochondrial dysfunction in cultured rat brain oligodendrocytes but not in astrocytes. *Glia* 53, 891-901.
- Gregori, L., Fuchs, C., Figueiredo-Pereira, M.E., Van Nostrand, W.E., and Goldgaber, D. (1995). Amyloid beta-protein inhibits ubiquitin-dependent protein degradation in vitro. *J Biol Chem* 270, 19702-19708.
- Griffin, J.W., and Watson, D.F. (1988). Axonal transport in neurological disease. *Ann Neurol* 23, 3-13.
- Griffiths, I., Klugmann, M., Anderson, T., Yool, D., Thomson, C., Schwab, M.H., Schneider, A., Zimmermann, F., McCulloch, M., Nadon, N., *et al.* (1998). Axonal swellings and degeneration in mice lacking the major proteolipid of myelin. *Science* 280, 1610-1613.
- Guardiola-Diaz, H.M., Ishii, A., and Bansal, R. (2012). Erk1/2 MAPK and mTOR signaling sequentially regulates progression through distinct stages of oligodendrocyte differentiation. *Glia* 60, 476-486.
- Guyenet, S.J., Furrer, S.A., Damian, V.M., Baughan, T.D., La Spada, A.R., and Garden, G.A. (2010). A simple composite phenotype scoring system for evaluating mouse models of cerebellar ataxia. *J Vis Exp*.
- Hagemeyer, N., Goebbels, S., Papiol, S., Kastner, A., Hofer, S., Begemann, M., Gerwig, U.C., Boretius, S., Wieser, G.L., Ronnenberg, A., *et al.* (2012). A myelin gene causative of a catatonia-depression syndrome upon aging. *EMBO Mol Med* 4, 528-539.
- Hall, C.S. (1932). A study of the rat's behavior in a field: a contribution to method in comparative psychology. *University of California Publications in Psychology* 6, 1-12.
- Halliday, G.M., and Stevens, C.H. (2011). Glia: initiators and progressors of pathology in Parkinson's disease. *Mov Disord* 26, 6-17.
- Hara, T., Hashimoto, Y., Akuzawa, T., Hirai, R., Kobayashi, H., and Sato, K. (2014). Rer1 and calnexin regulate endoplasmic reticulum retention of a peripheral myelin protein 22 mutant that causes type 1A Charcot-Marie-Tooth disease. *Sci Rep* 4, 6992.
- Hartmann-Petersen, R., and Gordon, C. (2004). Integral UBL domain proteins: a family of proteasome interacting proteins. *Semin Cell Dev Biol* 15, 247-259.
- Helmut Kettenmann, B.R.R. (2013). *Neuroglia*, Third edition edn (Oxford).
- Hershko, A., and Ciechanover, A. (1998). The ubiquitin system. *Annu Rev Biochem* 67, 425-479.

- Hildebrand, C., and Hahn, R. (1978). Relation between myelin sheath thickness and axon size in spinal cord white matter of some vertebrate species. *J Neurol Sci* 38, 421-434.
- Hsieh, S.T., Kidd, G.J., Crawford, T.O., Xu, Z., Lin, W.M., Trapp, B.D., Cleveland, D.W., and Griffin, J.W. (1994). Regional modulation of neurofilament organization by myelination in normal axons. *J Neurosci* 14, 6392-6401.
- Hsu, J.M., Lee, Y.C., Yu, C.T., and Huang, C.Y. (2004). Fbx7 functions in the SCF complex regulating Cdk1-cyclin B-phosphorylated hepatoma up-regulated protein (HURP) proteolysis by a proline-rich region. *J Biol Chem* 279, 32592-32602.
- Huang, Y.L., Chiu, A.W., Huan, S.K., Wang, Y.C., Ju, J.P., and Lu, C.L. (2003). Prognostic significance of hepatoma-up-regulated protein expression in patients with urinary bladder transitional cell carcinoma. *Anticancer Res* 23, 2729-2733.
- Ilyin, G.P., Rialland, M., Pigeon, C., and Guguen-Guillouzo, C. (2000). cDNA cloning and expression analysis of new members of the mammalian F-box protein family. *Genomics* 67, 40-47.
- Ip, C.W., Kroner, A., Bendszus, M., Leder, C., Kobsar, I., Fischer, S., Wiendl, H., Nave, K.A., and Martini, R. (2006). Immune cells contribute to myelin degeneration and axonopathic changes in mice overexpressing proteolipid protein in oligodendrocytes. *J Neurosci* 26, 8206-8216.
- Jahn, O., Tenzer, S., and Werner, H.B. (2009). Myelin proteomics: molecular anatomy of an insulating sheath. *Mol Neurobiol* 40, 55-72.
- Jahngen-Hodge, J., Obin, M.S., Gong, X., Shang, F., Nowell, T.R., Jr., Gong, J., Abasi, H., Blumberg, J., and Taylor, A. (1997). Regulation of ubiquitin-conjugating enzymes by glutathione following oxidative stress. *J Biol Chem* 272, 28218-28226.
- Jansen, A.H., Reits, E.A., and Hol, E.M. (2014). The ubiquitin proteasome system in glia and its role in neurodegenerative diseases. *Front Mol Neurosci* 7, 73.
- Jessen, K.R., and Mirsky, R. (2005). The origin and development of glial cells in peripheral nerves. *Nat Rev Neurosci* 6, 671-682.
- Jimenez-Mateos, E.M., Gonzalez-Billault, C., Dawson, H.N., Vitek, M.P., and Avila, J. (2006). Role of MAP1B in axonal retrograde transport of mitochondria. *Biochem J* 397, 53-59.
- Jin, J., Cardozo, T., Lovering, R.C., Elledge, S.J., Pagano, M., and Harper, J.W. (2004). Systematic analysis and nomenclature of mammalian F-box proteins. *Genes Dev* 18, 2573-2580.
- Juurlink, B.H., Thorburne, S.K., and Hertz, L. (1998). Peroxide-scavenging deficit underlies oligodendrocyte susceptibility to oxidative stress. *Glia* 22, 371-378.

- Kabuta, T., Furuta, A., Aoki, S., Furuta, K., and Wada, K. (2008). Aberrant interaction between Parkinson disease-associated mutant UCH-L1 and the lysosomal receptor for chaperone-mediated autophagy. *J Biol Chem* 283, 23731-23738.
- Kamholz, J., Sessa, M., Scherer, S., Vogelbacker, H., Mokuno, K., Baron, P., Wrabetz, L., Shy, M., and Pleasure, D. (1992). Structure and expression of proteolipid protein in the peripheral nervous system. *J Neurosci Res* 31, 231-244.
- Kang, K., Lee, D., Hong, S., Park, S.G., and Song, M.R. (2013). The E3 ligase Mind bomb-1 (Mib1) modulates Delta-Notch signaling to control neurogenesis and gliogenesis in the developing spinal cord. *J Biol Chem* 288, 2580-2592.
- Kassmann, C.M., Lappe-Siefke, C., Baes, M., Brugger, B., Mildner, A., Werner, H.B., Natt, O., Michaelis, T., Prinz, M., Frahm, J., *et al.* (2007). Axonal loss and neuroinflammation caused by peroxisome-deficient oligodendrocytes. *Nat Genet* 39, 969-976.
- Kawabe, H., and Brose, N. (2011). The role of ubiquitylation in nerve cell development. *Nat Rev Neurosci* 12, 251-268.
- Kazunori Sango, J.Y. (2014). Schwann cell development and pathology (Japan, Springer).
- Kearns, C.A., Ravanelli, A.M., Cooper, K., and Appel, B. (2015). Fbxw7 Limits Myelination by Inhibiting mTOR Signaling. *J Neurosci* 35, 14861-14871.
- Keeney, P.M., Xie, J., Capaldi, R.A., and Bennett, J.P., Jr. (2006). Parkinson's disease brain mitochondrial complex I has oxidatively damaged subunits and is functionally impaired and misassembled. *J Neurosci* 26, 5256-5264.
- Keswani, S.C., Buldanlioglu, U., Fischer, A., Reed, N., Polley, M., Liang, H., Zhou, C., Jack, C., Leitz, G.J., and Hoke, A. (2004). A novel endogenous erythropoietin mediated pathway prevents axonal degeneration. *Ann Neurol* 56, 815-826.
- Kirk, R., Laman, H., Knowles, P.P., Murray-Rust, J., Lomonosov, M., Meziane el, K., and McDonald, N.Q. (2008). Structure of a conserved dimerization domain within the F-box protein Fbxo7 and the PI31 proteasome inhibitor. *J Biol Chem* 283, 22325-22335.
- Kisselev, A.F., and Goldberg, A.L. (2005). Monitoring activity and inhibition of 26S proteasomes with fluorogenic peptide substrates. *Methods Enzymol* 398, 364-378.
- Klugmann, M., Schwab, M.H., Puhlhofer, A., Schneider, A., Zimmermann, F., Griffiths, I.R., and Nave, K.A. (1997). Assembly of CNS myelin in the absence of proteolipid protein. *Neuron* 18, 59-70.
- Komander, D., and Rape, M. (2012). The ubiquitin code. *Annu Rev Biochem* 81, 203-229.

- Kondziela, W. (1964). Eine neue methode zur messung der muskularen relaxtion bei weissen mausen. *Arch Int Pharmacodyn* 152, 277-284.
- Konishi, Y., Stegmuller, J., Matsuda, T., Bonni, S., and Bonni, A. (2004). Cdh1-APC controls axonal growth and patterning in the mammalian brain. *Science* 303, 1026-1030.
- Krajewski, K.M., Lewis, R.A., Fuerst, D.R., Turansky, C., Hinderer, S.R., Garbern, J., Kamholz, J., and Shy, M.E. (2000). Neurological dysfunction and axonal degeneration in Charcot-Marie-Tooth disease type 1A. *Brain* 123 (Pt 7), 1516-1527.
- Kuharev, J., Navarro, P., Distler, U., Jahn, O., and Tenzer, S. (2015). In-depth evaluation of software tools for data-independent acquisition based label-free quantification. *Proteomics* 15, 3140-3151.
- Kuiken, H.J., Egan, D.A., Laman, H., Bernardts, R., Beijersbergen, R.L., and Dirac, A.M. (2012). Identification of F-box only protein 7 as a negative regulator of NF-kappaB signalling. *J Cell Mol Med* 16, 2140-2149.
- Laborde, E. (2010). Glutathione transferases as mediators of signaling pathways involved in cell proliferation and cell death. *Cell Death Differ* 17, 1373-1380.
- Laman, H. (2006). Fbxo7 gets proactive with cyclin D/cdk6. *Cell Cycle* 5, 279-282.
- Laman, H., Funes, J.M., Ye, H., Henderson, S., Galinanes-Garcia, L., Hara, E., Knowles, P., McDonald, N., and Boshoff, C. (2005). Transforming activity of Fbxo7 is mediated specifically through regulation of cyclin D/cdk6. *EMBO J* 24, 3104-3116.
- Laman, H., Funes, J.M., Ye, H., Henderson, S., Galinanes-Garcia, L., Hara, E., Knowles, P., McDonald, N., and Boshoff, C. (2005). Transforming activity of Fbxo7 is mediated specifically through regulation of cyclin D/cdk6. *EMBO J* 24, 3104-3116.
- Lappe-Siefke, C., Goebels, S., Gravel, M., Nicksch, E., Lee, J., Braun, P.E., Griffiths, I.R., and Nave, K.A. (2003). Disruption of Cnp1 uncouples oligodendroglial functions in axonal support and myelination. *Nat Genet* 33, 366-374.
- Larocca, J.N., and Norton, W.T. (2007). Isolation of myelin. *Curr Protoc Cell Biol Chapter* 3, Unit3 25.
- Lee, H.K., Shin, Y.K., Jung, J., Seo, S.Y., Baek, S.Y., and Park, H.T. (2009). Proteasome inhibition suppresses Schwann cell dedifferentiation in vitro and in vivo. *Glia* 57, 1825-1834.
- Lee, S.M., Chin, L.S., and Li, L. (2012a). Protein misfolding and clearance in demyelinating peripheral neuropathies: Therapeutic implications. *Commun Integr Biol* 5, 107-110.

- Lee, Y., Morrison, B.M., Li, Y., Lengacher, S., Farah, M.H., Hoffman, P.N., Liu, Y., Tsingalia, A., Jin, L., Zhang, P.W., *et al.* (2012b). Oligodendroglia metabolically support axons and contribute to neurodegeneration. *Nature* 487, 443-448.
- Leone, D.P., Genoud, S., Atanasoski, S., Grausenburger, R., Berger, P., Metzger, D., Macklin, W.B., Chambon, P., and Suter, U. (2003). Tamoxifen-inducible glia-specific Cre mice for somatic mutagenesis in oligodendrocytes and Schwann cells. *Mol Cell Neurosci* 22, 430-440.
- Li, G.Z., Vissers, J.P., Silva, J.C., Golick, D., Gorenstein, M.V., and Geromanos, S.J. (2009). Database searching and accounting of multiplexed precursor and product ion spectra from the data independent analysis of simple and complex peptide mixtures. *Proteomics* 9, 1696-1719.
- Lilienbaum, A. (2013). Relationship between the proteasomal system and autophagy. *Int J Biochem Mol Biol* 4, 1-26.
- Lindsten, K., de Vrij, F.M., Verhoef, L.G., Fischer, D.F., van Leeuwen, F.W., Hol, E.M., Masucci, M.G., and Dantuma, N.P. (2002). Mutant ubiquitin found in neurodegenerative disorders is a ubiquitin fusion degradation substrate that blocks proteasomal degradation. *J Cell Biol* 157, 417-427.
- Lohmann, E., Coquel, A.S., Honore, A., Gurvit, H., Hanagasi, H., Emre, M., Leutenegger, A.L., Drouet, V., Sahbatou, M., Guven, G., *et al.* (2015). A new F-box protein 7 gene mutation causing typical Parkinson's disease. *Mov Disord* 30, 1130-1133.
- Lowry, O.H., Rosebrough, N.J., Farr, A.L., and Randall, R.J. (1951). Protein measurement with the Folin phenol reagent. *J Biol Chem* 193, 265-275.
- Luft, J.H. (1961). Improvements in epoxy resin embedding methods. *J Biophys Biochem Cytol* 9, 409-414.
- Luong, T.N., Carlisle, H.J., Southwell, A., and Patterson, P.H. (2011). Assessment of motor balance and coordination in mice using the balance beam. *J Vis Exp*.
- Mandelkow, E., and Mandelkow, E.M. (1995). Microtubules and microtubule-associated proteins. *Curr Opin Cell Biol* 7, 72-81.
- Mandrekar, S., Jiang, Q., Lee, C.Y., Koenigsnecht-Talboo, J., Holtzman, D.M., and Landreth, G.E. (2009). Microglia mediate the clearance of soluble Abeta through fluid phase macropinocytosis. *J Neurosci* 29, 4252-4262.
- Martini, R., Zielasek, J., Toyka, K.V., Giese, K.P., and Schachner, M. (1995). Protein zero (P0)-deficient mice show myelin degeneration in peripheral nerves characteristic of inherited human neuropathies. *Nat Genet* 11, 281-286.

- Matsuura, K., Kabuto, H., Makino, H., and Ogawa, N. (1997). Pole test is a useful method for evaluating the mouse movement disorder caused by striatal dopamine depletion. *J Neurosci Methods* 73, 45-48.
- McCutchen-Maloney, S.L., Matsuda, K., Shimbara, N., Binns, D.D., Tanaka, K., Slaughter, C.A., and DeMartino, G.N. (2000). cDNA cloning, expression, and functional characterization of PI31, a proline-rich inhibitor of the proteasome. *J Biol Chem* 275, 18557-18565.
- McNaught, K.S., Mytilineou, C., Jnobaptiste, R., Yabut, J., Shashidharan, P., Jennert, P., and Olanow, C.W. (2002). Impairment of the ubiquitin-proteasome system causes dopaminergic cell death and inclusion body formation in ventral mesencephalic cultures. *J Neurochem* 81, 301-306.
- Melander, A., Olsson, J., Lindberg, G., Salzman, A., Howard, T., Stang, P., Lydick, E., Emslie-Smith, A., Boyle, D.I., Evans, J.M., *et al.* (1999). 35th Annual Meeting of the European Association for the Study of Diabetes : Brussels, Belgium, 28 September-2 October 1999. *Diabetologia* 42, A1-A330.
- Meziane el, K., Randle, S.J., Nelson, D.E., Lomonosov, M., and Laman, H. (2011). Knockdown of Fbxo7 reveals its regulatory role in proliferation and differentiation of haematopoietic precursor cells. *J Cell Sci* 124, 2175-2186.
- Michailov, G.V., Sereda, M.W., Brinkmann, B.G., Fischer, T.M., Haug, B., Birchmeier, C., Role, L., Lai, C., Schwab, M.H., and Nave, K.A. (2004). Axonal neuregulin-1 regulates myelin sheath thickness. *Science* 304, 700-703.
- Morgan, D.O. (1995). Principles of CDK regulation. *Nature* 374, 131-134.
- Morland, C., Henjum, S., Iversen, E.G., Skrede, K.K., and Hassel, B. (2007). Evidence for a higher glycolytic than oxidative metabolic activity in white matter of rat brain. *Neurochem Int* 50, 703-709.
- Mukoyama, M., Yamazaki, K., Kikuchi, T., and Tomita, T. (1989). Neuropathology of gracile axonal dystrophy (GAD) mouse. An animal model of central distal axonopathy in primary sensory neurons. *Acta Neuropathol* 79, 294-299.
- Mulder, S.D., Nielsen, H.M., Blankenstein, M.A., Eikelenboom, P., and Veerhuis, R. (2014). Apolipoproteins E and J interfere with amyloid-beta uptake by primary human astrocytes and microglia in vitro. *Glia* 62, 493-503.
- Naef, R., Adlkofer, K., Lescher, B., and Suter, U. (1997). Aberrant protein trafficking in Trembler suggests a disease mechanism for hereditary human peripheral neuropathies. *Mol Cell Neurosci* 9, 13-25.
- Nave, K.A. (2010a). Myelination and support of axonal integrity by glia. *Nature* 468, 244-252.

- Nave, K.A. (2010b). Myelination and the trophic support of long axons. *Nat Rev Neurosci* 11, 275-283.
- Nave, K.A., and Salzer, J.L. (2006). Axonal regulation of myelination by neuregulin 1. *Curr Opin Neurobiol* 16, 492-500.
- Nelson, D.E., Randle, S.J., and Laman, H. (2013). Beyond ubiquitination: the atypical functions of Fbxo7 and other F-box proteins. *Open Biol* 3, 130131.
- Nguyen, M.D., Lariviere, R.C., and Julien, J.P. (2000). Reduction of axonal caliber does not alleviate motor neuron disease caused by mutant superoxide dismutase 1. *Proc Natl Acad Sci U S A* 97, 12306-12311.
- Noiges, R., Eichinger, R., Kutschera, W., Fischer, I., Nemeth, Z., Wiche, G., and Propst, F. (2002). Microtubule-associated protein 1A (MAP1A) and MAP1B: light chains determine distinct functional properties. *J Neurosci* 22, 2106-2114.
- Norton, W.T., and Autilio, L.A. (1965). The Chemical Composition of Bovine Cns Myelin. *Ann N Y Acad Sci* 122, 77-85.
- Norton, W.T., and Poduslo, S.E. (1973a). Myelination in rat brain: changes in myelin composition during brain maturation. *J Neurochem* 21, 759-773.
- Norton, W.T., and Poduslo, S.E. (1973b). Myelination in rat brain: method of myelin isolation. *J Neurochem* 21, 749-757.
- Ogawa, N., Hirose, Y., Ohara, S., Ono, T., and Watanabe, Y. (1985). A simple quantitative bradykinesia test in MPTP-treated mice. *Res Commun Chem Pathol Pharmacol* 50, 435-441.
- Orban-Nemeth, Z., Simader, H., Badurek, S., Trancikova, A., and Propst, F. (2005). Microtubule-associated protein 1S, a short and ubiquitously expressed member of the microtubule-associated protein 1 family. *J Biol Chem* 280, 2257-2265.
- Osaka, H., Wang, Y.L., Takada, K., Takizawa, S., Setsuie, R., Li, H., Sato, Y., Nishikawa, K., Sun, Y.J., Sakurai, M., *et al.* (2003). Ubiquitin carboxy-terminal hydrolase L1 binds to and stabilizes monoubiquitin in neuron. *Hum Mol Genet* 12, 1945-1958.
- Osterhout, D.J., Marin-Husstege, M., Abano, P., and Casaccia-Bonnel, P. (2002). Molecular mechanisms of enhanced susceptibility to apoptosis in differentiating oligodendrocytes. *J Neurosci Res* 69, 24-29.
- Paisan-Ruiz, C., Guevara, R., Federoff, M., Hanagasi, H., Sina, F., Elahi, E., Schneider, S.A., Schwingenschuh, P., Bajaj, N., Emre, M., *et al.* (2010). Early-onset L-dopa-responsive parkinsonism with pyramidal signs due to ATP13A2, PLA2G6, FBXO7 and spatacsin mutations. *Mov Disord* 25, 1791-1800.

- Parker, W.D., Jr., Boyson, S.J., and Parks, J.K. (1989). Abnormalities of the electron transport chain in idiopathic Parkinson's disease. *Ann Neurol* 26, 719-723.
- Patel, P.I., Roa, B.B., Welcher, A.A., Schoener-Scott, R., Trask, B.J., Pentao, L., Snipes, G.J., Garcia, C.A., Francke, U., Shooter, E.M., *et al.* (1992). The gene for the peripheral myelin protein PMP-22 is a candidate for Charcot-Marie-Tooth disease type 1A. *Nat Genet* 1, 159-165.
- Patzig, J., Jahn, O., Tenzer, S., Wichert, S.P., de Monasterio-Schrader, P., Rosfa, S., Kuharev, J., Yan, K., Bormuth, I., Bremer, J., *et al.* (2011). Quantitative and integrative proteome analysis of peripheral nerve myelin identifies novel myelin proteins and candidate neuropathy loci. *J Neurosci* 31, 16369-16386.
- Pekny, M., and Pekna, M. (2014). Astrocyte reactivity and reactive astrogliosis: costs and benefits. *Physiol Rev* 94, 1077-1098.
- Pellow, S., Chopin, P., File, S.E., and Briley, M. (1985). Validation of open:closed arm entries in an elevated plus-maze as a measure of anxiety in the rat. *J Neurosci Methods* 14, 149-167.
- Perry, G., Friedman, R., Shaw, G., and Chau, V. (1987). Ubiquitin is detected in neurofibrillary tangles and senile plaque neurites of Alzheimer disease brains. *Proc Natl Acad Sci U S A* 84, 3033-3036.
- Peyron, F., Timsit, S., Thomas, J.L., Kagawa, T., Ikenaka, K., and Zalc, B. (1997). In situ expression of PLP/DM-20, MBP, and CNP during embryonic and postnatal development of the jimpy mutant and of transgenic mice overexpressing PLP. *J Neurosci Res* 50, 190-201.
- Pfeiffer, S.E., Warrington, A.E., and Bansal, R. (1993). The oligodendrocyte and its many cellular processes. *Trends Cell Biol* 3, 191-197.
- Pickart, C.M. (2000). Ubiquitin biology: an old dog learns an old trick. *Nat Cell Biol* 2, E139-141.
- Pickart, C.M., and Eddins, M.J. (2004). Ubiquitin: structures, functions, mechanisms. *Biochim Biophys Acta* 1695, 55-72.
- Pickart, C.M., and Fushman, D. (2004). Polyubiquitin chains: polymeric protein signals. *Curr Opin Chem Biol* 8, 610-616.
- Pickering, M., Cumiskey, D., and O'Connor, J.J. (2005). Actions of TNF-alpha on glutamatergic synaptic transmission in the central nervous system. *Exp Physiol* 90, 663-670.
- Pickrell, A.M., and Youle, R.J. (2015). The roles of PINK1, parkin, and mitochondrial fidelity in Parkinson's disease. *Neuron* 85, 257-273.

- Poliak, S., and Peles, E. (2003). The local differentiation of myelinated axons at nodes of Ranvier. *Nat Rev Neurosci* 4, 968-980.
- Polymeropoulos, M.H., Hurko, O., Hsu, F., Rubenstein, J., Basnet, S., Lane, K., Dietz, H., Spetzler, R.F., and Rigamonti, D. (1997). Linkage of the locus for cerebral cavernous hemangiomas to human chromosome 7q in four families of Mexican-American descent. *Neurology* 48, 752-757.
- Preibisch, S., Saalfeld, S., and Tomancak, P. (2009). Globally optimal stitching of tiled 3D microscopic image acquisitions. *Bioinformatics* 25, 1463-1465.
- Randle, S.J., Nelson, D.E., Patel, S.P., and Laman, H. (2015). Defective erythropoiesis in a mouse model of reduced Fbxo7 expression due to decreased p27 expression. *J Pathol* 237, 263-272.
- Reynolds, E.S. (1963). The use of lead citrate at high pH as an electron-opaque stain in electron microscopy. *J Cell Biol* 17, 208-212.
- Richardson, K.C., Jarett, L., and Finke, E.H. (1960). Embedding in epoxy resins for ultrathin sectioning in electron microscopy. *Stain Technol* 35, 313-323.
- Riethmacher, D., Sonnenberg-Riethmacher, E., Brinkmann, V., Yamaai, T., Lewin, G.R., and Birchmeier, C. (1997). Severe neuropathies in mice with targeted mutations in the ErbB3 receptor. *Nature* 389, 725-730.
- Rosenbluth, J., Nave, K.A., Mierzwa, A., and Schiff, R. (2006). Subtle myelin defects in PLP-null mice. *Glia* 54, 172-182.
- Rushton, W.A. (1951). A theory of the effects of fibre size in medullated nerve. *J Physiol* 115, 101-122.
- Saab, A.S., Tzvetanova, I.D., and Nave, K.A. (2013). The role of myelin and oligodendrocytes in axonal energy metabolism. *Curr Opin Neurobiol* 23, 1065-1072.
- Sadahiro, S., Yoshikawa, H., Yagi, N., Yamamoto, Y., Yanagihara, T., Kimura, M., and Sakoda, S. (2000). Morphometric analysis of the myelin-associated oligodendrocytic basic protein-deficient mouse reveals a possible role for myelin-associated oligodendrocytic basic protein in regulating axonal diameter. *Neuroscience* 98, 361-367.
- Saiki, R.K., Scharf, S., Faloona, F., Mullis, K.B., Horn, G.T., Erlich, H.A., and Arnheim, N. (1985). Enzymatic amplification of beta-globin genomic sequences and restriction site analysis for diagnosis of sickle cell anemia. *Science* 230, 1350-1354.
- Sanchez, I., Hassinger, L., Paskevich, P.A., Shine, H.D., and Nixon, R.A. (1996). Oligodendroglia regulate the regional expansion of axon caliber and local accumulation of neurofilaments during development independently of myelin formation. *J Neurosci* 16, 5095-5105.

- Scarffe, L.A., Stevens, D.A., Dawson, V.L., and Dawson, T.M. (2014). Parkin and PINK1: much more than mitophagy. *Trends Neurosci* 37, 315-324.
- Schapira, A.H., Cooper, J.M., Dexter, D., Jenner, P., Clark, J.B., and Marsden, C.D. (1989). Mitochondrial complex I deficiency in Parkinson's disease. *Lancet* 1, 1269.
- Scheffner, M., Nuber, U., and Huibregtse, J.M. (1995). Protein ubiquitination involving an E1-E2-E3 enzyme ubiquitin thioester cascade. *Nature* 373, 81-83.
- Schlesinger, D.H., and Goldstein, G. (1975). Molecular conservation of 74 amino acid sequence of ubiquitin between cattle and man. *Nature* 255, 423-424.
- Shadrach, K.G., Rayborn, M.E., Hollyfield, J.G., and Bonilha, V.L. (2013). DJ-1-dependent regulation of oxidative stress in the retinal pigment epithelium (RPE). *PLoS One* 8, e67983.
- Sheehan, D., Meade, G., Foley, V.M., and Dowd, C.A. (2001). Structure, function and evolution of glutathione transferases: implications for classification of non-mammalian members of an ancient enzyme superfamily. *Biochem J* 360, 1-16.
- Sherr, C.J. (1996). Cancer cell cycles. *Science* 274, 1672-1677.
- Shine, H.D., Readhead, C., Popko, B., Hood, L., and Sidman, R.L. (1992). Morphometric analysis of normal, mutant, and transgenic CNS: correlation of myelin basic protein expression to myelinogenesis. *J Neurochem* 58, 342-349.
- Shirk, A.J., Anderson, S.K., Hashemi, S.H., Chance, P.F., and Bennett, C.L. (2005). SIMPLE interacts with NEDD4 and TSG101: evidence for a role in lysosomal sorting and implications for Charcot-Marie-Tooth disease. *J Neurosci Res* 82, 43-50.
- Shojaee, S., Sina, F., Banihosseini, S.S., Kazemi, M.H., Kalhor, R., Shahidi, G.A., Fakhrai-Rad, H., Ronaghi, M., and Elahi, E. (2008). Genome-wide linkage analysis of a Parkinsonian-pyramidal syndrome pedigree by 500 K SNP arrays. *Am J Hum Genet* 82, 1375-1384.
- Sijts, E.J., and Kloetzel, P.M. (2011). The role of the proteasome in the generation of MHC class I ligands and immune responses. *Cell Mol Life Sci* 68, 1491-1502.
- Simon, C.M., Jablonka, S., Ruiz, R., Tabares, L., and Sendtner, M. (2010). Ciliary neurotrophic factor-induced sprouting preserves motor function in a mouse model of mild spinal muscular atrophy. *Hum Mol Genet* 19, 973-986.
- Simons, M., and Nave, K.A. (2015). Oligodendrocytes: Myelination and Axonal Support. *Cold Spring Harb Perspect Biol* 8, a020479.
- Smith, K.J., and Lassmann, H. (2002). The role of nitric oxide in multiple sclerosis. *Lancet Neurol* 1, 232-241.

- Snyder, H., Mensah, K., Theisler, C., Lee, J., Matouschek, A., and Wolozin, B. (2003). Aggregated and monomeric alpha-synuclein bind to the S6' proteasomal protein and inhibit proteasomal function. *J Biol Chem* 278, 11753-11759.
- Snyder, J.L., Kearns, C.A., and Appel, B. (2012). Fbxw7 regulates Notch to control specification of neural precursors for oligodendrocyte fate. *Neural Dev* 7, 15.
- Solano, R.M., Casarejos, M.J., Menendez-Cuervo, J., Rodriguez-Navarro, J.A., Garcia de Yébenes, J., and Mena, M.A. (2008). Glial dysfunction in parkin null mice: effects of aging. *J Neurosci* 28, 598-611.
- Somlai, J.a.K., Tibor (2016). *Neuro-Ophthalmology* (Springer).
- Spillantini, M.G., Schmidt, M.L., Lee, V.M., Trojanowski, J.Q., Jakes, R., and Goedert, M. (1997). Alpha-synuclein in Lewy bodies. *Nature* 388, 839-840.
- Sprinkle, T.J., McMorris, F.A., Yoshino, J., and DeVries, G.H. (1985). Differential expression of 2':3'-cyclic nucleotide 3'-phosphodiesterase in cultured central, peripheral, and extraneural cells. *Neurochem Res* 10, 919-931.
- Stefanis, L., Larsen, K.E., Rideout, H.J., Sulzer, D., and Greene, L.A. (2001). Expression of A53T mutant but not wild-type alpha-synuclein in PC12 cells induces alterations of the ubiquitin-dependent degradation system, loss of dopamine release, and autophagic cell death. *J Neurosci* 21, 9549-9560.
- Stefanova, N., Bucke, P., Duerr, S., and Wenning, G.K. (2009). Multiple system atrophy: an update. *Lancet Neurol* 8, 1172-1178.
- Stefanova, N., Kaufmann, W.A., Humpel, C., Poewe, W., and Wenning, G.K. (2012). Systemic proteasome inhibition triggers neurodegeneration in a transgenic mouse model expressing human alpha-synuclein under oligodendrocyte promoter: implications for multiple system atrophy. *Acta Neuropathol* 124, 51-65.
- Steru, L., Chermat, R., Thierry, B., and Simon, P. (1985). The tail suspension test: a new method for screening antidepressants in mice. *Psychopharmacology (Berl)* 85, 367-370.
- Suter, U., and Scherer, S.S. (2003). Disease mechanisms in inherited neuropathies. *Nat Rev Neurosci* 4, 714-726.
- Sypecka, J. (2003). Different vulnerability to cytotoxicity and susceptibility to protection of progenitors versus mature oligodendrocytes. *Pol J Pharmacol* 55, 881-885.
- Tait, S., Gunn-Moore, F., Collinson, J.M., Huang, J., Lubetzki, C., Pedraza, L., Sherman, D.L., Colman, D.R., and Brophy, P.J. (2000). An oligodendrocyte cell adhesion molecule at the site of assembly of the paranodal axo-glial junction. *J Cell Biol* 150, 657-666.

- Tamura, Y., Kataoka, Y., Cui, Y., Takamori, Y., Watanabe, Y., and Yamada, H. (2007). Intracellular translocation of glutathione S-transferase pi during oligodendrocyte differentiation in adult rat cerebral cortex in vivo. *Neuroscience* 148, 535-540.
- Tansey, K.E., McKay, W.B., and Kakulas, B.A. (2012). Restorative neurology: consideration of the new anatomy and physiology of the injured nervous system. *Clin Neurol Neurosurg* 114, 436-440.
- Taveggia, C., Zanazzi, G., Petrylak, A., Yano, H., Rosenbluth, J., Einheber, S., Xu, X., Esper, R.M., Loeb, J.A., Shrager, P., *et al.* (2005). Neuregulin-1 type III determines the ensheathment fate of axons. *Neuron* 47, 681-694.
- Timmerman, V., Nelis, E., Van Hul, W., Nieuwenhuijsen, B.W., Chen, K.L., Wang, S., Ben Othman, K., Cullen, B., Leach, R.J., Hanemann, C.O., *et al.* (1992). The peripheral myelin protein gene PMP-22 is contained within the Charcot-Marie-Tooth disease type 1A duplication. *Nat Genet* 1, 171-175.
- Todorich, B., Pasquini, J.M., Garcia, C.I., Paez, P.M., and Connor, J.R. (2009). Oligodendrocytes and myelination: the role of iron. *Glia* 57, 467-478.
- Townsend, D.M., and Tew, K.D. (2003). The role of glutathione-S-transferase in anti-cancer drug resistance. *Oncogene* 22, 7369-7375.
- Trapp, B.D., and Stys, P.K. (2009). Virtual hypoxia and chronic necrosis of demyelinated axons in multiple sclerosis. *Lancet Neurol* 8, 280-291.
- Tsou, A.P., Yang, C.W., Huang, C.Y., Yu, R.C., Lee, Y.C., Chang, C.W., Chen, B.R., Chung, Y.F., Fann, M.J., Chi, C.W., *et al.* (2003). Identification of a novel cell cycle regulated gene, HURP, overexpressed in human hepatocellular carcinoma. *Oncogene* 22, 298-307.
- Tyler, W.A., Gangoli, N., Gokina, P., Kim, H.A., Covey, M., Levison, S.W., and Wood, T.L. (2009). Activation of the mammalian target of rapamycin (mTOR) is essential for oligodendrocyte differentiation. *J Neurosci* 29, 6367-6378.
- Udomsinprasert, R., Pongjaroenkit, S., Wongsantichon, J., Oakley, A.J., Prapanthadara, L.A., Wilce, M.C., and Ketterman, A.J. (2005). Identification, characterization and structure of a new Delta class glutathione transferase isoenzyme. *Biochem J* 388, 763-771.
- van Tijn, P., Hol, E.M., van Leeuwen, F.W., and Fischer, D.F. (2008). The neuronal ubiquitin-proteasome system: murine models and their neurological phenotype. *Prog Neurobiol* 85, 176-193.
- Veitenhansl, M., Stegner, K., Hierl, F.X., Dieterle, C., Feldmeier, H., Gutt, B., Landgraf, R., Garrow, A.P., Vileikyte, L., Findlow, A., *et al.* (2004). 40th EASD Annual Meeting of

- the European Association for the Study of Diabetes : Munich, Germany, 5-9 September 2004. *Diabetologia* 47, A1-A464.
- Verma, P., Chierzi, S., Codd, A.M., Campbell, D.S., Meyer, R.L., Holt, C.E., and Fawcett, J.W. (2005). Axonal protein synthesis and degradation are necessary for efficient growth cone regeneration. *J Neurosci* 25, 331-342.
- Vingill, S. (2016). Characterization of FBXO7 (*PARK15*) knockout mice modeling Parkinsonian-Pyramidal Syndrome (Göttingen, Georg-August university, doctoral thesis).
- Vingill, S., Brockelt, D., Lancelin, C., Tatenhorst, L., Dontcheva, G., Preisinger, C., Schwedhelm-Domeyer, N., Joseph, S., Mitkovski, M., Goebbels, S., *et al.* (2016). Loss of FBXO7 (*PARK15*) results in reduced proteasome activity and models a parkinsonism-like phenotype in mice. *EMBO J* 35, 2008-2025.
- Wahl, S.E., McLane, L.E., Bercury, K.K., Macklin, W.B., and Wood, T.L. (2014). Mammalian target of rapamycin promotes oligodendrocyte differentiation, initiation and extent of CNS myelination. *J Neurosci* 34, 4453-4465.
- Wang, T., Arifoglu, P., Ronai, Z., and Tew, K.D. (2001). Glutathione S-transferase P1-1 (*GSTP1-1*) inhibits c-Jun N-terminal kinase (*JNK1*) signaling through interaction with the C terminus. *J Biol Chem* 276, 20999-21003.
- Wang, X. (2017). Destructive Cellular Paths Underlying Familial and Sporadic Parkinson Disease Converge on Mitophagy. *Autophagy*, 0.
- Wang, Z., Zhang, Y., Zhang, S., Guo, Q., Tan, Y., Wang, X., Xiong, R., Ding, J., and Chen, S. (2011). DJ-1 can inhibit microtubule associated protein 1 B formed aggregates. *Mol Neurodegener* 6, 38.
- Weber, K., and Osborn, M. (1969). The reliability of molecular weight determinations by dodecyl sulfate-polyacrylamide gel electrophoresis. *J Biol Chem* 244, 4406-4412.
- Wieser, G.L., Gerwig, U.C., Adamcio, B., Barrette, B., Nave, K.A., Ehrenreich, H., and Goebbels, S. (2013). Neuroinflammation in white matter tracts of *Cnp1* mutant mice amplified by a minor brain injury. *Glia* 61, 869-880.
- Wilkins, A., Majed, H., Layfield, R., Compston, A., and Chandran, S. (2003). Oligodendrocytes promote neuronal survival and axonal length by distinct intracellular mechanisms: a novel role for oligodendrocyte-derived glial cell line-derived neurotrophic factor. *J Neurosci* 23, 4967-4974.
- Winston, J.T., Koeppe, D.M., Zhu, C., Elledge, S.J., and Harper, J.W. (1999). A family of mammalian F-box proteins. *Curr Biol* 9, 1180-1182.
- Wisniewski, J.R., Zougman, A., Nagaraj, N., and Mann, M. (2009). Universal sample preparation method for proteome analysis. *Nat Methods* 6, 359-362.

- Woodward, K.J. (2008). The molecular and cellular defects underlying Pelizaeus-Merzbacher disease. *Expert Rev Mol Med* 10, e14.
- Wyss-Coray, T., Loike, J.D., Brionne, T.C., Lu, E., Anankov, R., Yan, F., Silverstein, S.C., and Husemann, J. (2003). Adult mouse astrocytes degrade amyloid-beta in vitro and in situ. *Nat Med* 9, 453-457.
- Wyss-Coray, T., and Mucke, L. (2002). Inflammation in neurodegenerative disease--a double-edged sword. *Neuron* 35, 419-432.
- Yalcin-Cakmakli, G., Olgiati, S., Quadri, M., Breedveld, G.J., Cortelli, P., Bonifati, V., and Elibol, B. (2014). A new Turkish family with homozygous FBXO7 truncating mutation and juvenile atypical parkinsonism. *Parkinsonism Relat Disord* 20, 1248-1252.
- Yamamoto, A., Lucas, J.J., and Hen, R. (2000). Reversal of neuropathology and motor dysfunction in a conditional model of Huntington's disease. *Cell* 101, 57-66.
- Yin, X., Crawford, T.O., Griffin, J.W., Tu, P., Lee, V.M., Li, C., Roder, J., and Trapp, B.D. (1998). Myelin-associated glycoprotein is a myelin signal that modulates the caliber of myelinated axons. *J Neurosci* 18, 1953-1962.
- Yonashiro, R., Kimijima, Y., Shimura, T., Kawaguchi, K., Fukuda, T., Inatome, R., and Yanagi, S. (2012). Mitochondrial ubiquitin ligase MITOL blocks S-nitrosylated MAP1B-light chain 1-mediated mitochondrial dysfunction and neuronal cell death. *Proc Natl Acad Sci U S A* 109, 2382-2387.
- Yu, W.P., Collarini, E.J., Pringle, N.P., and Richardson, W.D. (1994). Embryonic expression of myelin genes: evidence for a focal source of oligodendrocyte precursors in the ventricular zone of the neural tube. *Neuron* 12, 1353-1362.
- Zaiss, D.M., Standera, S., Kloetzel, P.M., and Sijts, A.J. (2002). PI31 is a modulator of proteasome formation and antigen processing. *Proc Natl Acad Sci U S A* 99, 14344-14349.
- Zhang, D., Hu, X., Qian, L., O'Callaghan, J.P., and Hong, J.S. (2010). Astrogliosis in CNS pathologies: is there a role for microglia? *Mol Neurobiol* 41, 232-241.
- Zhang, Y., Chen, K., Sloan, S.A., Bennett, M.L., Scholze, A.R., O'Keeffe, S., Phatnani, H.P., Guarnieri, P., Caneda, C., Ruderisch, N., *et al.* (2014). An RNA-sequencing transcriptome and splicing database of glia, neurons, and vascular cells of the cerebral cortex. *J Neurosci* 34, 11929-11947.
- Zheng, N., Schulman, B.A., Song, L., Miller, J.J., Jeffrey, P.D., Wang, P., Chu, C., Koepp, D.M., Elledge, S.J., Pagano, M., *et al.* (2002). Structure of the Cul1-Rbx1-Skp1-F boxSkp2 SCF ubiquitin ligase complex. *Nature* 416, 703-709.

- Zhou, Z.D., Xie, S.P., Sathiyamoorthy, S., Saw, W.T., Sing, T.Y., Ng, S.H., Chua, H.P., Tang, A.M., Shaffra, F., Li, Z., *et al.* (2015). F-box protein 7 mutations promote protein aggregation in mitochondria and inhibit mitophagy. *Hum Mol Genet* 24, 6314-6330.
- Zuchero, J.B., and Barres, B.A. (2011). Between the sheets: a molecular sieve makes myelin membranes. *Dev Cell* 21, 385-386.

